

Multi-Wavelength Study of Feedback Driven Region: Star Formation Rate and Efficiency

Thesis

Master of Science

in

Astronomy and Astrophysics

by

Divyansh Chourey

(SC18M018)

Supervised by

Dr. Jessy Jose

Assistant Professor, IISER Tirupati

Dr. Anandmayee Tej

Professor, IIEST Thiruvananthapuram



**Department of Earth and Space Science
Indian Institute of Space Science and Technology
Thiruvananthapuram, India**

May 2020

Certificate

This is to certify that the Thesis titled ***Multi-Wavelength Study of Feedback Driven Region: Star Formation Rate and Efficiency*** submitted by **Divyansh Chourey**, to the Indian Institute of Space Science and Technology, Thiruvananthapuram, in partial fulfillment for the award of the degree of **Master of Science in Astronomy and Astrophysics** is a bona fide record of the original work carried out by him under my supervision. The contents of this Thesis, in full or in parts, have not been submitted to any other Institute or University for the award of any degree or diploma.

Dr. Anandmayee Tej
Professor
Dept. of Earth and Space Science
IIST, Trivandrum

Dr. Samir Mandal
Associate Professor and HoD
Dept. of Earth and Space Science
IIST, Trivandrum

Dr. Jessy Jose
Assistant Professor
Dept. of Physics
IISER, Tirupati

Place: Thiruvananthapuram
Date: May 2020

Declaration

I declare that this Thesis titled ***Multi-Wavelength Study of Feedback Driven Region: Star Formation Rate and Efficiency*** submitted in partial fulfillment for the award of the degree of **Master of Science in Astronomy and Astrophysics** is a record of the original work carried out by me under the supervision of **Dr. Jessy Jose**, Assistant Professor, IISER, Tirupati and **Dr. Anandmayee Tej**, Professor, IIIST, Trivandrum, and has not formed the basis for the award of any degree, diploma, associateship, fellowship, or other titles in this or any other Institution or University of higher learning. In keeping with the ethical practice in reporting scientific information, due acknowledgments have been made wherever the findings of others have been cited.

Place: Thiruvananthapuram

Divyansh Chourey

Date: May 2020

(SC18M018)

Acknowledgements

I would first like to express my deep gratitude to my supervisor Dr. Jessy Jose for her continuous guidance and support. she has always been extremely motivating throughout the course of my work, and urged me to explore and find the answers right from the fundamentals.

I am grateful to Dr. Anandmayee Tej, Professor for her constant guidance and help which made it convenient and easy to work on my project. All of their valuable suggestions and insightful discussions have helped me a lot. Her care, patience and guidance are invaluable.

I am sincerely thankful to Dr. Jagadheep D., Dr. Anand Narayanan, Dr. Samir Mandal, Dr. Sarita Vig, Dr. Resmi Lekshmi alongwith Dr. Anandmayee Tej, who were my very first professors and mentors in Astronomy and Astrophysics at IIST. They introduced me to this fascinating discipline in the most beautiful way possible, and rooted my interests firmly into Astronomy. They were always available for discussions and advices, which helped me a lot. I am grateful to Sai ‘chetta’ Krishnan, our Lab Assistant, who was ever ready to provide with all the technical help.

Finally, I must express my profound gratitude to my loving parents, especially my *papa*, who is responsible for planting the seed of ‘crave for Physics’ in me. Its hard to even think about finding words to thank my *maa*, it’s a undeniable fact that *Kuputro Jayet, Kwachidapy Kumata Na Bhawati*. Finally to my dear brother for providing me with unfailing support and continuous encouragement throughout my years of study. Today whatever I have done, whatever I will do tomorrow, whatever I will become, its all because of my Guru, my God and my life time Guardians.

Divyansh Chourey

Abstract

Bright-rimmed clouds (BRCs) are small molecular clouds found near the edges of evolved H II regions, with the bright rims facing the ionizing stars. The morphology and physical conditions of BRCs match well with the theoretical models of Radiation driven implosion (RDI), so they are generally believed to be the sites of RDI.

This project involves study of such BRCs in different H II complexes like W3, W4 and W5. we have started with studying W5E H II region which includes two BRCs, BRC 13 and BRC 14. The data analysis on two BRCs involves multi-wavelength photometric study followed by identification of young stellar objects (YSOs) and analysis of spectral energy distribution (SEDs).

For multi-wavelength study, we are considering Near Infrared data from NEWFIRM and 2 Micron all sky survey (2MASS), for Mid-Infrared study, Spitzer data is analyzed. For optical window, Pan-Starrs data is used. Later using all these, the project involves the study of star formation rate, star formation efficiency in all possible BRCs in giant molecular complexes in W3, W4 and W5.

Contents

List of Figures	xiii
List of Tables	xxi
1 Introduction	1
1.1 Star Formation Scenario	1
1.2 Effects of Massive star on interstellar medium	2
1.2.1 H II Regions	3
1.2.2 H II region expansion: phase I	5
1.2.3 H II region expansion: phase II	6
1.3 Feedback Driven Regions	7
1.4 Triggered Star Formation	12
1.4.1 Collect and Collapse	13
1.4.2 Radiation Driven Implosion	16
1.5 Bright Rimmed Clouds	22
1.5.1 Classification of Bright-Rimmed Clouds	23
1.5.2 Observations of BRCs and SFO catalogs	24
1.5.3 Star Formation in Bright Rimmed Cloud	25
1.5.4 Mass and Age estimation at BRCs	27
1.5.5 Some other properties of BRCs	31
1.6 Young Stellar System	33
1.6.1 NIR Color-Color Diagram	33
1.6.2 Spectral Energy Distribution and Classification of YSOs	35
1.7 Motivation and Region of Study	40
2 Methodology and Data Analysis	43
2.1 Instruments	43

2.1.1	NEWFIRM	43
2.1.2	Spitzer IRAC	44
2.1.3	Panoramic Survey Telescope and rapid Response System I (Pan-STARR I)	44
2.2	Photometry	46
2.2.1	Aperture Photometry	46
2.2.2	Point spread function (PSF) Photometry	48
2.3	Near Infrared Data Reduction	51
2.3.1	NIR Source Detection	51
2.3.2	NIR Aperture Photometry	53
2.3.3	NIR PSF Photometry	53
2.3.4	NIR Source Matching	55
2.3.5	Calibration and Catalog merger	55
2.4	Mid-Infrared Data Reduction	57
2.4.1	MIR Source Detection	57
2.4.2	MIR Aperture Photometry	58
2.4.3	MIR PSF Photometry	59
2.4.4	MIR Source Matching	59
2.4.5	Calibration and Catalog merger	59
2.5	Extinction Estimation Methods	63
2.5.1	Column Density Map	63
2.5.2	PNICER	64
2.5.3	Using JHKs[CH1][CH2] photometry	68
2.6	YSO Identification	70
2.6.1	YSO identification:Phase I	71
2.6.2	YSO identification: Phase II	73
2.6.3	YSO identification: Phase III	73
2.7	Spectral Energy Distribution (SEDs) Modelling	74
2.7.1	Theoretical SED Model	74
2.7.2	VOSA SED Analyzer	77
3	Results	85
3.1	Selection of Sources for Analysis	85
3.2	Magnitude Distributions and Color-Color-Diagrams	86
3.3	Extinction Estimation	91

3.3.1	Using Column Density Map	91
3.3.2	Using JHKs[3.6][4.5] photometry	93
3.3.3	Using Field Stars	94
3.3.4	Using PNICER	96
3.4	YSO identification	100
3.5	SED Modelling and HR diagram	101
4	Conclusions and Future Work	105
	Bibliography	106

List of Figures

1.1	Schematic of H II region. This shows a central ionizing star within a spherically symmetric cloud. The ionization front is trailing to shock front, where the number density within the H II region is n_H^1 and number density for ambient ISM is n_H^0 Stahler & Palla (2008). This shows the collected neutral material and cold dust at the outskirts of H II region. It shows the hot ionized gas and hot dust within the Strömgren radius (Zavagno et al. 2006).	4
1.2	Spherical H II region showing first and second phase of expansion. Ionized material surrounding central star has relatively low density n_H^1 , surrounded by thin neutral shell of matter. This shell expands supersonically to ambient cloud with density n_H^0 (Stahler & Palla 2008).	6
1.3	Protostellar outflow activity at NGC 1333. (a) [S II] image of HH 740A and 740B. The image is centered southwest of NGC 1333; (b) $H\alpha + [S$ II] image showing HH 741, image is centered southwest of NGC 1333; (c) Smoothed $H\alpha + [S$ II] image showing HH 756, 752A, 752B, and 752C, centered north of NGC 1333; (d) Smoothed [S II] image centered south of NGC 1333, showing HH 352 and 762 (Walawender et al. 2005).	9
1.4	Effect of Radiation pressure feedback. (a) Density profile for the simulated cloud core. Cluster formation is shown at 0, 50, 100, 150, 500 Myr (black, green, turquoise, blue, red respectively). (b) Radial velocity of compressed shell, the radiatively compressed shell estimated to move outward at around $2-6 \text{ kms}^{-1}$. Horizontal axis shows radial coverage in parsec. (Scoville et al. 2001)	10

1.5 Schematic view of a H II region showing its second phase of expansion along with different mechanism of triggered star formation: (1) Small-scale gravitational instabilities; (2) Large-scale gravitational instabilities resulting in the formation of high-mass protostellar cores; (3) Ionizing radiation imploding on a turbulent ambient medium; (4) Radiation-driven implosion of pre-existing dense clumps (Deharveng et al. 2010).	13
1.6 Column density maps (viewed along the z-axis) from three epochs of the smooth (left-hand column) and noisy (right-hand column) 1.3×10^6 particle simulation (Dale et al. 2007).	15
1.7 Time sequence of column-density images showing the evolution of the simulated cloud when it is exposed to a relatively high ionizing flux. t/Myr is given in the top right-hand corner of figure. The color bar shows the values of column density in log scale and axes are in parsec Lefloch & Lazareff (1994).	18
1.8 Time evolution of bright rimmed cloud. Three-dimensional projection of bright rimmed cloud is shown in left side. Right side column shows the evolution, color-coded with column density, contour shows the ionization fraction. Ionized gas is shown in blue, neutral gas in red (Kessel-Deynet & Burkert 2003).	20
1.9 Dense cloud along the symmetry axis is shown (Only the top half portion). An ionization-shock front propagates into this initially spherical cloud. The ionizing photon flux at (r_0, θ_0) depends on the absorption along the dashed line toward the ionizing star (Bertoldi 1989).	21
1.10 Classification of the rim shape (Sugitani et al. 1991). Relation between W and L for all three types of BRCs shown above are given in table 1.3.	24
1.11 (J-H)/(H-K) NIR colour-colour diagrams. Open triangles represent NIR excess stars and blue asterisk represent the H α emission sources. The continuous and dashed curves represent the intrinsic MS and giant locus respectively (Bessell & Brett 1988). The dotted line represents the intrinsic colours of CTTSs (Meyer et al. 1997), and the parallel dashed lines are the reddening vectors with crosses separated by $AV = 5$ mag. The error bars in the top middle show average errors in the colours. (Panwar et al. 2014).	26

1.12 Colour-Colour diagrams for BRC 5, BRC 7 and BRC 39. Red squares and green circles are Class I sources and Class II sources respectively. The continuous lines and dashed lines are the criteria used by Gutermuth et al. (2009). The error bars show the errors in the respective colours of Class I and Class II sources. (Panwar et al. 2014)	27
1.13 colour-colour diagrams for BRC 5, BRC 7 and BRC 39. Red squares and green circles are Class I sources are Class II sources respectively. The continuous lines and dashed lines are the criteria used by Koenig et al. (2011). The error bars show the errors in the respective colours of Class I and Class II sources. (Panwar et al. 2014)	28
1.14 Near-infrared color-color diagram (J-H)/(H-K). The Continuous curves shows the intrinsic locus of Main sequence (below) and Giants(above). The dashed lines are reddening vectors. The dotted lines are showing color of from ideal blackbody distributions (Chauhan et al. 2011)	28
1.15 V/(V-I) color-magnitude diagram for BRC 13 and BRC 14. It shows 0.1, 1.0 and 5.0 Myr from Siess et al. (2000). Isochrones are corrected for distance and mean reddening. (Chauhan et al. 2011)	29
1.16 Cummulative mass function (CMF) for BRC 13 (c) and BRC 14 (d). The error bars represents poission error (Chauhan et al. 2011)	29
1.17 (a) Cumulative age distributions of CTTSs and WTTSs as a function of stellar age. Solid line shows the age distribution for CTTSs and dashed line shows for WTTSs. Age axis is labelled in million years. (b) Cumulative mass function of the A-type (filled circles) and B/C-type BRCs (open circles). Error bars represent poissionion errors. The CMF for the standard MF is shown by short dashed lines (Chauhan et al. 2009)	30
1.18 Number density of sources as a function of the distance to the H II region for YSO-selected sources (solid line), non-YSO sources (dashed line), clump centers (dot-dashed line), and a random sample of points (triple-dot-dashed line). The upper axis shows angular scale in degrees and the lower axis linear scale, assuming a distance of 2 kpc. Negative distances indicate sources inside the H II region (in projection); note the strong peak there. Error bars are Poissonian. Karr & Martin (2003)	31
1.19 Star formation efficiency in the cores (filled circles) and in the active regions (open circles) with respect to the number of YSOs. Sharma et al. (2016)	32

1.20 Distribution of YSOs in the W5E H II region. Small red circles show the locations of NIR-excess sources, whereas the large blue circles show the YSOs identified using the Spitzer observations (Stahler & Palla 2008).	32
1.21 NIR CC diagram (J-H)/(H-K). Solid curves shows the intrinsic locus of Main sequence (below) and Giants(above), dashed lines are reddening vectors and dotted lines are showing color of from ideal blackbody (Stahler & Palla 2008).	33
1.22 Near-infrared color-color diagram for IRAS 06055+2039 region. The two solid curves represent the loci of the main sequence (thin line) and the giant stars (thicker line) (Bessell & Brett 1988). The long-dashed line is the classical T Tauri locus (Meyer et al. 1997). The parallel dotted lines are reddening vectors with the crosses placed along these lines at intervals corresponding to five magnitudes of visual extinction. Reddening law used is ($A_J/A_V = 0.282$; $A_H/A_V = 0.175$; $A_K/A_V = 0.112$) (Rieke & Lebofsky 1985). The plot is classified into three regions namely F , T , and P (see text for details) (Tej et al. 2006).	35
1.23 SEDs of three sources from ρ Ophiuchi dark cloud complex region (Stahler & Palla 2008). These three sources are example for class I (WL12), class II (SR 24) and class III (SR 20). The dashed curve shows the blackbody distribution ($T_{eff} = 2300$ K).	36
1.24 Example SED of class 0 object (L1448) (Stahler & Palla 2008).	37
1.25 Evolution of low mass stars and their SEDs (Wilking 1989). Left hand side shows the SEDs of the different classes of YSOs, the combined effect of intrinsic blackbody and infrared excess/disk. Right side shows schematic evolution of star from parent clouds (core) to weak line T-Tauri star.	39
1.26 Region of giant molecular complex W5. Color composite image shows two HII regions, W5E and W5W in radio 1.42 GHz (red), Spitzer IRAC 8.0 μ m (cyan). The yellow plus sign shows the position of ionizing source (Deharveng et al. 2012).	40
1.27 Color-composite image of W5E HII region with 250 μ m Herschel-SPIRE (red), 250 μ m Herschel-PACS (green), DSS2 survey (blue). The yellow cross shows HD18326 which is a ionizing star cluster for W5E HII region (Deharveng et al. 2012).	41
2.1 NEWFIRM filter profile	44

2.2	Spitzer IRAC filter profile	45
2.3	Pan-STARR filter profile	45
2.4	Point source photometry showing the aperture radius with the inner and out sky radius to measure background sky value.	46
2.5	Growth of curve showing the trend between magnitude value and aperture radii. Photometry is done on a 2MASS field using ‘phot’ task.	48
2.6	Magnitude vs Magnitude error for a 2MASS field. Photometry is done by IRAF ‘phot’ task keeping the aperture radii fixed.	48
2.7	Example of PSF model fitted using analytic function MOFFAT on linear scale (a) and on two dimensional plane (b).	50
2.8	PSF photometry Flowchart	51
2.9	K-Band NEWFIRM FITS image. In top left panel, yellow box is showing BRC 13 and magenta box is showing BRC 14	52
2.10	Magnitude v/s Error Plots for NEWFIRM JHK images	54
2.11	Distribution of magnitude difference between NEWFIRM and 2MASS . . .	56
2.12	Distribution of color difference between NEWFIRM and 2MASS	57
2.13	Magnitude v/s Error Plots for JHK filter from 2MASS and NEWFIRM . . .	58
2.14	Magnitude v/s Error Plots for MIR IRAC images. Channel 1 (3.6 micron) (top left), Channel 2 (4.5 micron) (top right), Channel 3 (5.8 micron) (bottom left) and Channel 4 (8.0 micron) (bottom right).	60
2.15	Distribution of offset for each MIR filter. Channel 1 (3.6 micron) (top left), Channel 2 (4.5 micron) (top right), Channel 3 (5.8 micron) (bottom left) and Channel 4 (8.0 micron) (bottom right). Offset is calculated from Koenig et. al 2008.	61
2.16	Plot generated by the PNICER showing the density distribution for the feature combinations. This plot is generated as an example for Orion A region.	65
2.17	Color-Color plot generated by the PNICER showing the [J-H] vs [H-K] distribution.	65
2.18	Plot generated by the PNICER showing the kernel density distribution map for the feature combinations, Jmag (top), Hmag (middle) and Kmag (bottom). This plot is generated as an example for Orion A region.	66
2.19	Plot generated by the PNICER showing the extinction map in V-band (top), the uncertainty map (middle) and a number density map (bottom) . This plot is generated as an example for Orion A region.	67
2.20	Flow chart showing the photosphere modelling process.	75

2.21	Uncertainty grid showing the nine points to calculate the age and mass with their own uncertainty.	83
2.22	Interpolation is used to estimate the minimum distance from point P to get D1 and D2 from either side of the point to the respective isochrone.	84
3.1	NEWFIRM K-band image showing the area of image from where sources are considered for results and analysis.	85
3.2	Magnitude distribution for the photometric data in case of Near-Infrared. (a) For J band, (b) for H band and (c) for K band. The vertical axis shows the number of sources and horizontal axis shows the magnitude. The distribution is plotted for all those sources which are falling in the box shown in fig. 3.1.	86
3.3	Magnitude distribution for the photometric data in case of Mid-Infrared. (a) For CH1 ($3.6 \mu\text{m}$) band, (b) for CH2 ($4.5 \mu\text{m}$) band, (c) for CH3 ($5.8 \mu\text{m}$) band and (d) for CH4 ($8.0 \mu\text{m}$). The vertical axis shows the number of sources and horizontal axis shows the magnitude. The distribution is plotted for all those sources which are falling in the box shown in fig. 3.1.	87
3.4	Magnitude distribution for the photometric data in case of PanSTARR optical data. (a) For g ($0.49 \mu\text{m}$) band, (b) for r ($0.62 \mu\text{m}$) band, (c) for i ($0.75 \mu\text{m}$) band, (d) for z ($0.87 \mu\text{m}$) band and (e) for y ($0.96 \mu\text{m}$) band. The vertical axis shows the number of sources and horizontal axis shows the magnitude. The distribution is plotted for all those sources which are falling in the box shown in fig. 3.1.	88
3.5	Color-Color Plots; (a) (J-H) vs (H-K) Near Infrared color-color plot; (b) (i-z) vs (z-y) Optical color-color plot.	89
3.6	Color-Magnitude Plots; (a) J vs (J-H) Color-Magnitude plot; (b) [3.6] vs ([3.6]-[4.5]) Color-Magnitude plot; (c) y vs (z-y) Color-Magnitude plot; (d) z vs (z-H) Color-Magnitude plot;	90
3.7	Column density map given in Deharveng et al. (2012) showing W5E HII region. Colorbar shows the $\text{N}(\text{H}_2)$ value in cm^{-2} . Values of column density is estimated using method discussed in section 2.5.1.	92
3.8	Extinction distribution obtained for sources within the box shown in fig. 3.1. Extinction is calculated from column density map given in Deharveng et al. (2012).	93

3.9 Extinction distribution obtained for sources within the box shown in fig. 3.1. Extinction is calculated JHKs[3.6][4.5] photometric data (Gutermuth et al. 2009).	94
3.10 Color-color diagram (J-H)/(H-K) for W5E HII from area shown in Fig. 3.1. The Continuous curves shows the intrinsic locus of Main sequence (below) and Giants(above) (Bessell & Brett 1988). The dashed line represents the locus of intrinsic color of classical T-Tauri (Meyer et al. 1997). The dashed-dotted lines are reddening vectors from (Cohen et al. 1981). All the sources lies leftward to the middle reddening vectors are used as field stars to calculate extinction based on intrinsic color of field stars. The extinction map built using that is shown in fig, 3.11.	95
3.11 Extinction map of W5E HII region made by using the background field stars. The colorbar shows extinction in K-band i.e. A_K . The map has 315 arcmin ² field of view and resolution if 1 arcmin.	95
3.12 Color-Color plot produced by PNICER (J-H) vs (H-K). The data is taken from 2MASS point source catalog in JHK band with read flag as '222'. . .	96
3.13 Plot generated by the PNICER showing the density distribution for the feature combinations. This plot is generated for W5E HII region in order to make the extinction map of the same region for all three filter combination.	97
3.14 Plot generated by the PNICER showing the kernel density distribution map for the feature combinations, Jmag (left), Hmag (middle) and Kmag (right). This plot is generated for W5E HII region.	97
3.15 Histogram distribution of extinction values in V-band (A_v) for all those sources falling in green box in fig. 3.1. The extinction values are taken from PNICER map shown in fig. 3.16.	98
3.16 Extinction map generated by PNICER for W5E HII region. The colorbar shows the extinction values in V-band (A_v). The map shown has field of view of 0.5 deg ² with the resolution of 0.5 arcsec.	99
3.17 Extinction uncertainty map generated by PNICER for W5E HII region. The colorbar shows the extinction uncertainty values in V-band (σA_v) which is calculated from PNICER map. The map shown has field of view of 0.5 deg ² with the resolution of 0.5 arcsec.	99

3.18 color-color diagram [Ks] - [3.6] vs [3.6]-[4.5] showing the class II (green) and class I (blue) sources with field/class III sources (red). The color cutoff are given in detail in section 2.6. The identification scheme is taken from Gutermuth et al. (2005, 2009).	101
3.19 The HR diagram plot for the source (in black) identified in section 3.4. The horizontal axis is temperature in K and vertical axis given bolometric luminosity (L/L_{\odot}) in logscale. The red lines are the isochrones of 0.007 Myr (right most) till 10 Myr (left most). The blue dotted curves are the evolutionary tracks of mass $0.1 M_{\odot}$ (very bottom) to $30 M_{\odot}$ (very top). The isochrones and evolutionary tracks are taken from Siess et al. (2000). . .	102
3.20 Mass distribution for all the sources identified in section 3.4 and modelled by VOSA.	103
3.21 Age distribution for all the sources identified in section 3.4 and modelled by VOSA. Distribution shown for BRC 13 (in red) and BRC 14 (in blue), histograms are fitted with gaussian (dotted curves) to calculate the mean age for the two BRCs.	103

List of Tables

1.1	Physical Properties star formation sites	2
1.2	Classification of Ionization fronts	14
1.3	Classification of BRCs	24
1.4	H II Regions in Northern hemisphere selected by Sugitani et al. (1991) . .	24
1.5	H II Regions in Southern hemisphere selected by Sugitani & Ogura (1994) .	25
1.6	Mean age inside/on and outside the rim	30
1.7	YSO classification	38
2.1	Mean Wavelength and Bandwidth for all twelve filters used for this project .	43
2.2	Pan-STARR PS1 5σ depth and seeing	45
2.3	Parameter used for source detection	51
2.4	Parameters used in Aperture Photometry (PHOT)	53
2.5	Parameters used for PSF and ALLSTAR	53
2.6	Offsets used for calibration	55
2.7	MIR: Parameter used for source detection	57
2.8	Parameters used in Aperture Photometry (PHOT)	58
2.9	Parameters used for PSF and ALLSTAR	59
2.10	Offsets used for calibration	60
2.11	Sample Catalog of BRC 13 and BRC 14 for NIR (J, H, K), MIR(CH1, CH2, CH3, CH4), Pan-STARR (g,r,i,z,y)	62
2.12	Some commonly used theoretical modeles with their parameter grid space .	76
2.13	Sample VOSA input file	78
3.1	Completeness limit (90%) for the distributions shown in fig. 3.2, fig. 3.3, fig. 3.4.	89

Chapter 1

Introduction

1.1 Star Formation Scenario

A star is defined as a gaseous body which qualifies two conditions. First, it is bounded by its self-gravity and second, it should radiate energy produced by its internal source. A common inference of this condition is that stars evolve as they internally supply energy, which changes the structure and composition of star throughout its life. Birth of a star is an intricate process which is extremely important and interesting science. These processes are known as Star formation and it must have happened innumerable times since Big Bang, though Big Bang did not result in a universe full of stars and galaxies, but the left over of this explosion was diffused gas which later on, by virtue of many complex processes, fabricated our present universe.

Young stars usually forms in huge structures known as *Giant Molecular Cloud* or *Cloud Complexes*. The gas in these structures is predominately molecular hydrogen H_2 . These cold dense clouds have total mass of the order of $10^5 M_\odot$. Gas in these clouds is very cold to radiate at higher frequencies like optical and X-ray, such that they are mostly brighter at higher wavelengths such as radio, millimeter and sub-millimeter by tracing molecules like CO.

Dust grains are next significant component of these clouds. Other than gas, molecular clouds accommodate small solid particles of dust which efficiently absorb/scatter light with wavelength smaller than their diameter. These dust grains re-radiate this energy into infrared wavelengths. These are the main cause of *Extinction* or *Reddening* observed along the line of sight towards these clouds.

Stars born within *Dense cores* in the molecular cloud (Blitz et al. 1993). These dense cores are the main site of star formation within the molecular clouds. Stars born within such cores produce lots of optical photons but they are unable to pass through the dense

column density caused by gas and dust. The dust grains absorbs these optical photons and again re-emit the energy which are detected at infrared wavelength.

In addition to dense cores, star formation also happens in Bok Globules (Bok & Reilly 1947). These are relatively small dark nebulae containing gas and dense cosmic dust, though star formation in these globules are rarer than molecular clouds. Physical properties of such kind of star formation sites are given in table 1.1.

Stars which consumes hydrogen as nuclear fuel at their core to produce energy are called *Zero-age Main Sequence stars*. But the evolution of a star starts as *Pre-main sequence source*. One of the main pre-main sequence sources are known as *T-Tauri stars*, these are objects identified by their circumstellar disk structure and they show near-infrared excess because of such disks. In such regions, there are also some even massive stars called *Herbig Ae/Be stars*.

Table 1.1: Physical Properties star formation sites

Diffuse	A_V (mag)	n_{tot} (cm^{-3})	L (pc)	T (K)	M (M_\odot)	Example
Diffuse	1	500	3	50	50	ζ Ophiuchi
Giant Molecular Clouds	2-20	100	50	15	10^5	Orion
Dark Clouds						
Complexes	5-30	500	10	10	10^4	Taurus-Auriga
Individual	>10	10^3	2	10	30	B1
Dense Cores/Bok Globules	>20	10^4	0.1	10	10	TMC-1/B335

In this project, we have attempted to study one of such region called *Bright-Rimmed Clouds*. They are the small globular structure found at the outskirts of ionized regions called *H II regions* made by the massive star (or star cluster) sitting at its center. We have studied the star formation process at bright-rimmed cloud region, mainly the pre-main sequence sources. It involves photometry, identification of pre-main sequence sources and their spectral senergy density (SED) modelling. Our final goal is to estimate the star formation efficiency and star formation rate in that region.

1.2 Effects of Massive star on interstellar medium

Feedback provided by massive star on ambient medium have profound influence. Observational manifestations of the interplay between the high mass stars and the surrounding ISM are important probes for studying the various evolutionary phases involved in their forma-

tion along with various types of feedback mechanism. The very initial stages are marked by the presence of the energetic jets with outflow events. Once the ‘switching-on’ happens, the outpouring of UV photons ionizing the surrounding neutral medium resulting in formation of the H II regions (see sec. 1.2.1). H II regions are formed by a newly formed massive star (or star cluster) expands into ambient ISM driven by various feedback mechanism like thermal over pressure, radiation pressure, power full stellar winds or combinations of all (see sec. 1.3) (Krumholz et al. 2014).

The result is a giant bubble spans about few parsec that shows up as a dense shell of swept up dust and gas between the shock front and ionization front, circumferential to a relatively low density, vacated cavity round the central star or star cluster. The coming section discusses more about such effect and their consequences. But before that its a good option to first look at the formation of H II region and some of its properties in next subsection.

1.2.1 H II Regions

Massive stars made up within the giant molecular cloud ionizes the neutral hydrogen in cloud. Massive star (with spectral type O and B type) are known to generate photons having energy greater than ionization energy of neutral hydrogen atom which is known to be 13.6 eV. Stellar *Lyman continuum radiation* which are generated by hydrogen recombination ionizes a spherical volume of neutral hydrogen gas circumferential to such massive stars which spans few parsec in radius. Recombination of electron and ionized hydrogen produces several spectral lines which include optical *Balmer series* of hydrogen. Apart from this, emission from such regions has been broadly seen at forbidden lines of N II, O II and many other. In addition to this, continuum emission at infrared (IR) and radio frequencies, millimeter, submillimeter and hydrogen recombination lines in radio regime is observed.

Temperature of such H II regions are estimated in several ways, such as from fraction of emission lines in visible and radio regions of spectrum, and from measures of Balmer and radio continuum (Spitzer Jr 2008). These analysis yields temperature around 7000 K to 10000 K. An illustrative H II region is shown in fig. 1.1, it shows the shock front and the ionization front with central ionizing star.

The existence of dust inside the H II region are the main source of observable optical continuum and observable infrared emission. Dense and bright photo-ionized clouds known as *Ultra-compact H II regions* are heavily obscured by dust. They are not observ-

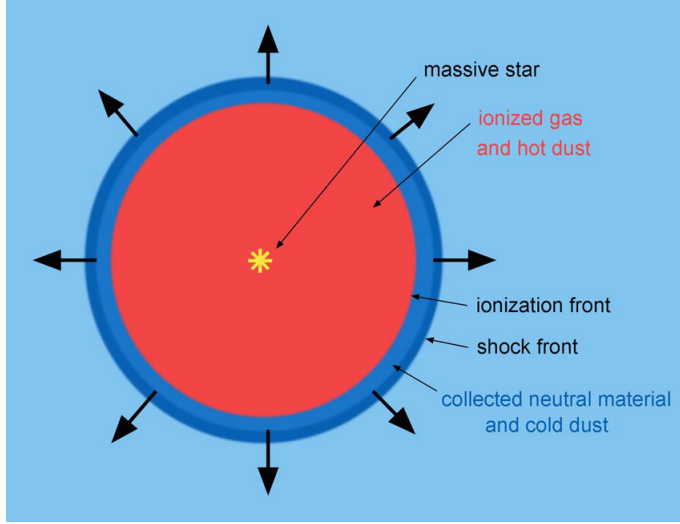


Figure 1.1: Schematic of H II region. This shows a central ionizing star within a spherically symmetric cloud. The ionization front is trailing to shock front, where the number density within the H II region is n_H^1 and number density for ambient ISM is n_H^0 Stahler & Palla (2008). This shows the collected neutral material and cold dust at the outskirts of H II region. It shows the hot ionized gas and hot dust within the Strömgren radius (Zavagno et al. 2006).

able at visible wavelengths but these are mainly detected by their free-free radio emission. Although, the ionization and recombination are continuous and concurrent processes, it is very easy to compute the scale at which these two processes balance each other. That is, the volumetric rate at which any parcel of gas is being ionized just offsets the recombination rate of free electron and protons in the same parcel. Integrating this over the whole sphere of gas, the total number of ionization events per unit time equals to the total rate of recombination.

Lets consider recombination first, to describe it quantitatively, lets introduce $\alpha_{recom}(T)$, *Recombination coefficient*. It has units of $cm^3 s^{-1}$ and it is a function of the local temperature in H II region. The volumetric rate at which free electrons and protons combine to produce atomic hydrogen assuming charge neutrality in ionized plasma is given by:

$$R = n_e n_p \alpha_{recom}(T) = n_e^2 \alpha_{recom}(T) \quad (1.1)$$

Similarly, in case of recombination within the sphere follows by integrating R over the volume. Assuming, for simplicity, that both n_e and T are spatial constant, lets balance total

ionization and recombination as;

$$N_* = \frac{4\pi}{3} n_e^2 \alpha'_{recom}(T) R_{str}^3 \quad (1.2)$$

On combining 1.1 and 1.2, the definition of *Strömgren radius* (Dyson & Williams 1997; Stahler & Palla 2008) is given by;

$$R_{str} = \left(\frac{3 N_*}{4\pi \alpha'_{recom}(T) n_e^2} \right)^{1/3} \quad (1.3)$$

1.2.2 H II region expansion: phase I

The equation derived for the Strömgren radius shows that the region of ionization is a static entity. But this is a dynamical system, hence it has to expand with time. At the very beginning, consider when there is no H II region exists around the massive star. Later, it expands rapidly to first, at the length scale of Strömgren radius, and then slowly afterwards.

The moving edge of H II region, known as *ionization front*, though it has some finite width, but it is narrow enough compared to the scale of Strömgren radius that it is treated as a sharp discontinuity. At the earliest stage, when the radius of the ionization front is negligible compared to Strömgren radius, the total rate of recombination inside the H II region is inadequate to match the rate of ionization by Lyman continuum radiation. Hence the leftover photons reach the edge of the shell and thus ionizing the gas beyond this. This explains the first phase of expansion and movement of ionization front radially outward. The equation governing this expansion is given by;

$$\lambda = [1 - e^{(-2\tau/3)}]^{1/3} \quad (1.4)$$

where, the λ is the radial distance normalized to Strömgren radius and $\tau (\equiv t/t_{rec})$ is the time constant of this expansion such that $t_{rec} (\equiv \frac{1}{n_H^0 \alpha_{rec}})$ is the recombination time within the H II region (Spitzer Jr 2008; Stahler & Palla 2008).

Now the pressure gradient plays the key role in transferring the event from phase I to phase II. With temperature over 10^4 K, the inner part of the H II region has pressure thrice as compared to outskirts. As the length scale approaches the Strömgren radius ($\lambda \rightarrow 1$) and ionization front starts slowing down (eq. 1.4), pressure difference drive the second phase of expansion of H II region. In addition to this, the pressure gradient is so high that ionization front is left behind the shock front produced at first in the cloud (see fig. 1.2).

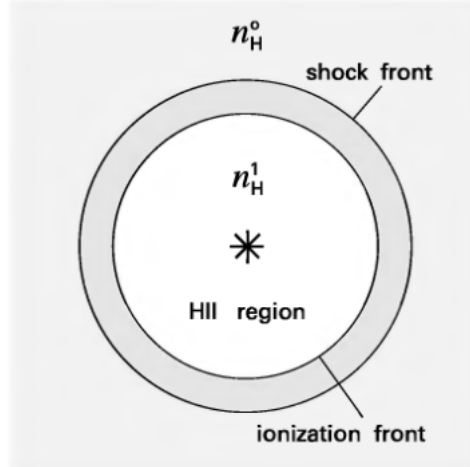


Figure 1.2: Spherical H II region showing first and second phase of expansion. Ionized material surrounding central star has relatively low density n_H^1 , surrounded by thin neutral shell of matter. This shell expands supersonically to ambient cloud with density n_H^0 (Stahler & Palla 2008).

1.2.3 H II region expansion: phase II

Decline in velocity of ionization front marks the commencement of the next phase of expansion. The value at which this turn over happens is the one at which the ionization front velocity declines to internal sound speed. During the early first phase expansion the ionization front speed ($> 10^3 \text{ kms}^{-1}$) exceeds way more than sound speed ($\approx 11 \text{ kms}^{-1}$, in a ionized gas at tempareture $\approx 10^4 \text{ K}$). It is known that the small pressure perturbation can propagate at the speed of sound in that medium, hence at initial first phase of expansion, these small pressure perturbation can not cross the ionization front.

But as the second phase begins, the ionization front moves with velocity close to sound speed in that medium. At this moment, the pressure perturbation from inside the H II region can cross the ionization front which leads to an expanding shock. Material outside the ionization front is compressed to make a relatively thin and neutral shell surrounding H II region. At this point the ionization and shock front moves almost at the same speed which later on declined below the sound speed of medium. This makes ionization front trail the shock front (see fig. 1.1 and fig. 1.2). Following is the equation of second phase expansion;

$$\lambda = \left[1 + \frac{7\tau'}{4} \right]^{4/7} \quad (1.5)$$

where, the λ is the radial distance normalized to Strömgren radius and $\tau' (\equiv (\nu t)/R_s)$ is

the time constant of this expansion such that ν is the speed of sound in the H II region and R_s is Strömgren radius (Dyson & Williams 1997; Spitzer Jr 2008; Stahler & Palla 2008).

1.3 Feedback Driven Regions

As discussed in previous section, young stars have significant effects on their neighboring regions. These stars affect the next generation of stars in many ways. In this section we have discussed some decisive feedback mechanism provided by these massive young stars. They have different classification but broadly they are divided into three categories (Krumholz et al. 2014):

- **Momentum Driven Feedback:** *Momentum feedback* is the deposition of momentum on the neighboring star forming cloud. This action pushes on the gas, stimulate turbulent motions within gas. If this feedback is adequate, it rips the neighboring medium apart entirely. This feedback is mainly designated by its identity of alleviating the radiative energy. Dense molecular clouds and lesser dense ISM are very good and efficient in radiative cooling such that when a young star injects energy into these clouds, the absorbed energy re-radiates away with time scale less than dynamical time scale of that cloud.

In this case, the amount of energy inserted does not influence the medium rather than momentum transferred by this feedback affects it as impossible to radiate away the momentum component. This momentum transfer is provided in two ways:

1. **Protostellar Outflow:** *Protostellar outflows* eject a huge bulk of mass from the regions around newborn stars. Such outflows inject energy and momentum into their surroundings which affects the environment in which the stars form (Norman & Silk 1980; McKee 1989). Protostellar outflow feedback is important wherever a large number of stars form in proximity and about in same epoch. Low-mass protocluster NGC 1333 is a classic paradigmatic object for this type of feedback, where molecular line and infrared observations reveal numerous outflows packed closely together (Bally et al. 1996; Knee & Sandell 2000; Bally et al. 2008).

Walawender et al. (2005) have studied NGC 1333 (Located at the west end of the Perseus molecular cloud) is a very active and young region of star formation that drives outflow activity. The molecular mass determined in the core of NGC

1333 is approximately $450 M_{\odot}$. They have investigated that the star cluster associated with NGC 1333 hosts approximately 150 young stars and approximately 30 groups of HH objects, with dozens and perhaps many more currently active outflows (Warin et al. 1996; Aspin et al. 1994; Greene & Lada 1996; Bally et al. 1996). Bally et al. (1996) defined the region as a *microburst of star formation* of interval estimated as less than 1 Myr within a cluster radius of less than 1 pc.

Study by Sandell & Knee (2001) found that outflows has crucial role in the balancing of the energy budget of NGC 1333. NGC 1333 has a filamentary cloud structure which consist of several cavities, some of which can be followed to some of the remnants of past outflow activity and some of the action of current outflows.

Knee & Sandell (2000) also estimated the energy and momentum injection rate by outflows in NGC 1333 (using an estimated age of an outflow of 0.1 Myr estimated by [Bally et al. (1996)]) to be $\dot{P} \sim 10 M_{\odot} \text{ kms}^{-1}$ and $L \sim 0.1 L_{\odot}$, sufficient to breach the cloud if these analysis holds for a typical cloud lifetime of about 10 Myr. Sandell & Knee (2001) illustrates that star formation activity could be triggered by density intensification at the exterior of such cavities. This implies that star formation could be triggered by previous events of star formation and the affiliated outflow activity. Different HH object along with associated outflow activities is shown in fig. 1.3.

2. **Radiation Pressure:** The second form of momentum feedback is radiation pressure which also seen at regions with massive stars. Radiation feedback mechanism of the dispatch of momentum and energy from the massive stars to the surrounding medium. Except for photons above 13.6 eV, this transfer of energy and momentum is mostly carried by the dust grains. Only a few observational study has been carried out for the investigation of the effects of radiation pressure feedback. Scoville et al. (2001) studied the M51 region and indicated that Radiation pressure from young clusters forming there exceeds their self-gravity. Lopez et al. (2011) and Lopez et al. (2014) studied the giant H II region 30 Doradus in the LMC as well as a larger sample of H II regions in the Magellanic Clouds (Pellegrini et al. 2011).

The formation of OB stars in a cloud core region is ceased at the point when the radiation pressure on the surrounding dust exceeds the self-gravity of the core star cluster and that is the key limit i.e. the maximum mass of standard

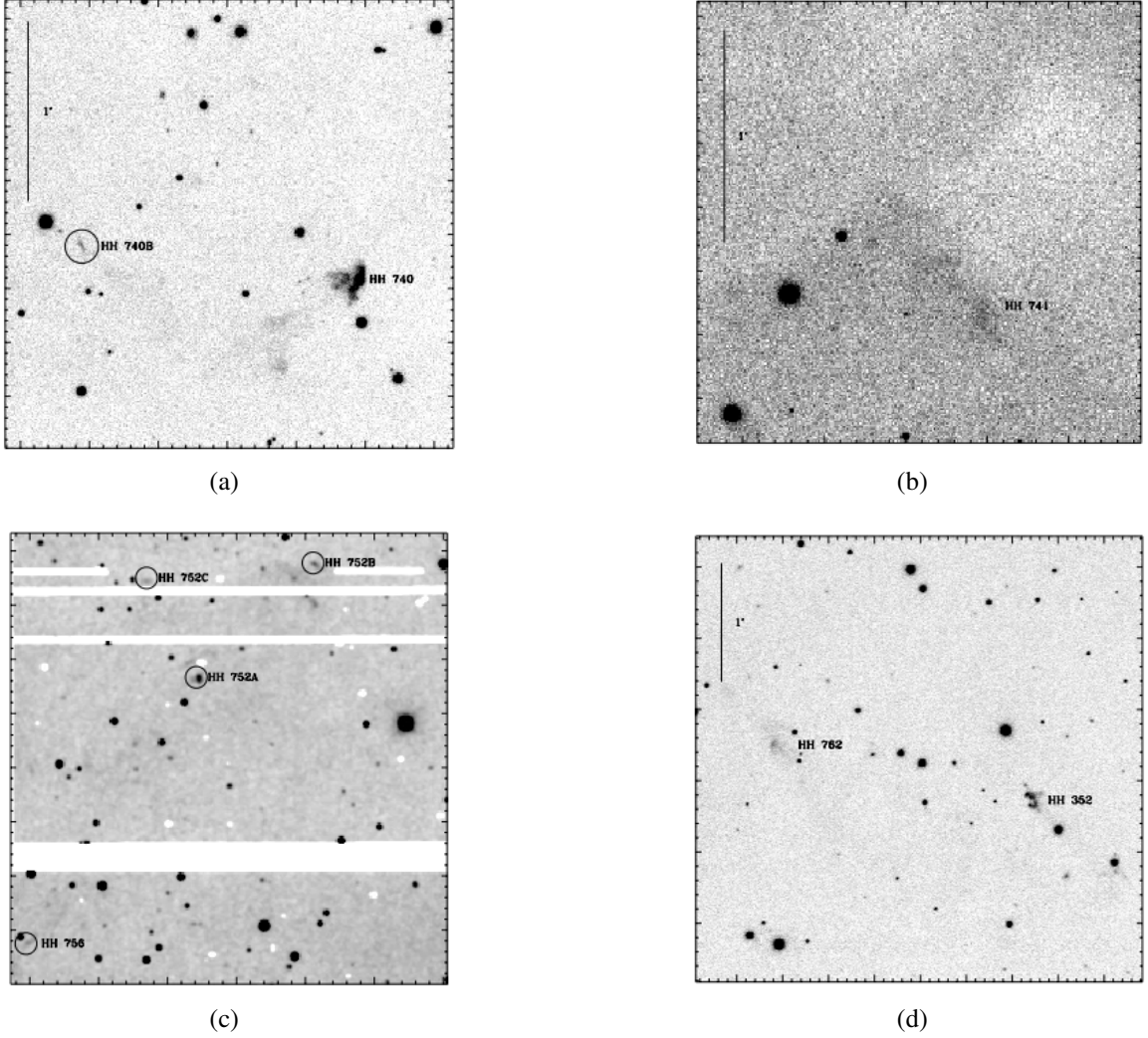


Figure 1.3: Protostellar outflow activity at NGC 1333. (a) [S II] image of HH 740A and 740B. The image is centered southwest of NGC 1333; (b) $H\alpha + [S\text{ II}]$ image showing HH 741, image is centered southwest of NGC 1333; (c) Smoothed $H\alpha + [S\text{ II}]$ image showing HH 756, 752A, 752B, and 752C, centered north of NGC 1333; (d) Smoothed [S II] image centered south of NGC 1333, showing HH 352 and 762 (Walawender et al. 2005).

OB star clusters. This happens to be at a stellar luminosity-to-mass ratio of $\sim 500 - 1000 (L/M)_\odot$ which results for clusters around $> 750 M_\odot$ (Scoville et al. 2001). A hydrodynamic model with an initial R^{-2} density distribution in free-fall collapse certify that the core star cluster is expected to self-limit at $\sim 10^3 M_\odot$.

Radiation pressure at this given limit effectively terminates further dust and gas accretion to the central dense core. However, radiatively compressed shell will

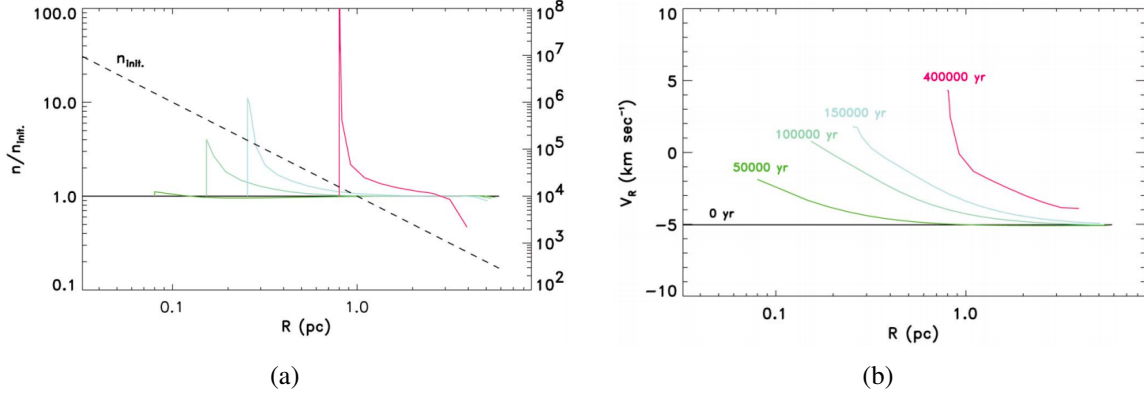


Figure 1.4: Effect of Radiation pressure feedback. (a) Density profile for the simulated cloud core. Cluster formation is shown at 0, 50, 100, 150, 500 Myr (black, green, turquoise, blue, red respectively). (b) Radial velocity of compressed shell, the radiatively compressed shell estimated to move outward at around $2-6 \text{ km s}^{-1}$. Horizontal axis shows radial coverage in parsec. (Scoville et al. 2001)

then propagate towards the outskirts with velocities around few kilometers per second which may possibly trigger a second wave of star formation out to a few parsec distance. Fig. 1.4 shows the density profile for the simulated cloud core. Cluster formation is shown at 0, 50, 100, 150, 500 Myr. The initial state was considered as free-fall collapse in a R^{-2} density distribution normalized to 10^8 cm^{-3} at 0.01 pc.

Final mass estimated of core cluster was $881 M_\odot$ and the luminosity was $10^6 L_\odot$. The core accretion was fully terminated by radiation pressure within 0.1 Myr. After this, the radiatively compressed shell estimated to move outward at around $2-6 \text{ km s}^{-1}$. Since the compressed shell is expected to show the Rayleigh-Taylor and Jeans instability, the star formation activity may continue in the outward moving shell. This will be discussed in more detail in sec. 1.4.1 and 1.4.2.

- **Explosive Feedback:** *Explosive feedback* is seen when stars heats up the gas at very rapid and fierce rate, also at very high temperature, such that it is no longer able to cool down itself on cloud's dynamical timescale. In this case, fraction of the energy added to the cloud is not lost as radiation to the ambient ISM.

Also the feedback ensue when the hot, over-pressured dense gas parcel expands explosively and does sweeps away the surrounding cold molecular material. This feedback has three types:

1. **Solar Winds:** Massive stars of spectral type O and early B type having photospheric surface temperature above 2.5×10^4 K produce strong winds (Vink et al. 2000). Main sequence stars have this temperature at mass around $40M_{\odot}$ or more and star with such high mass have Kelvin-Helmholtz time scales such that, they reach their main sequence while they are still under formation process (still accreting material from surrounding gas cloud) (Hosokawa & Omukai 2009). This implies that stellar winds starts to impinge the surrounding media of gas and dust at very early stage of their evolutionary process. Such stellar winds carry less momentum than radiation field (Kudritzki et al. 1999).

The radiation driven solar winds presumes to show a strong correlation between total mechanical momentum ($\dot{M}_{v_{\infty}}$) transferred to ambient ISM by stellar wind outflow and luminosity of mass lossing giant star (Castor et al. 1975a,b; Pauldrach et al. 1986; Kudritzki et al. 1989). The relation is given by;

$$\dot{M}_{v_{\infty}} \propto R_*^{-1/2} L^{1/\alpha_{eff}} \quad (1.6)$$

where, $\dot{M}_{v_{\infty}}$ is mass-loss rate, v_{∞} is terminal velocity of stellar wind and R_* is the stellar radius and α_{eff} is dimensionless number of the order of 2/3. It shows the power law exponent of the distribution function of line strengths of many spectral lines driving the stellar wind.

2. **Photo-ionization Feedback:** Massive stars $> 10M_{\odot}$ are known to produce large amount of UV photons which ionizes the surrounding gas and dust medium, this creates a ionized bubble (see 1.2.1). Equilibrium between heating and cooling processes inside H II regions maintains constant temperatures of about $10^4 K$ and internal sound velocity of 10 km s^{-1} (Osterbrock & Ferland 2006; Spitzer Jr 2008). This influences the evolution of YSOs in nearby region. On smaller scales, photo-ionization is expected to quench the growth of OB stars. Many simulation based studies has been done so far to study feedback by photo-ionization (Krumholz et al. 2006; Dale et al. 2012, 2013).

Krumholz et al. (2006) presented a semi-analytic dynamical models for giant molecular clouds evolving under the influence of H II regions made up by young massive star clusters. Here they have derived the equation of mass, radius and velocity dispersion of giant molecular cloud with given initial approximation of homologous motion of gas. They have also suggested that the predominant destruction mechanism for giant molecular clouds is dynamical unbinding by

the momentum propagated by an expanding H II region. But in case of massive clouds, this unbinding event does not happen till the H II region has been photoionized away about 90% of the giant molecular cloud's mass.

3. **Supernovae:** Supernovae are known as the most energetic source of feedback.

Around 10^{51} erg energy is transmitted into surrounding ambient medium as thermal energy as well as kinetic energy of particles. This thermal energy has very long cooling span. Even though, study by Krumholz & Matzner (2009); Fall et al. (2010) pointed out that supernovae are of quite limited affecting process on the scales of individual star clusters because due to timescales of the process but the first supernovae do not occur until around 4 Myr after the commencement of star formation. However, study by Krumholz et al. (2014) emphasize that supernovae are unimportant in case of star clusters and does not apply on the larger scales of diffuse giant molecular clouds or galaxies.

- **Thermal Feedback:** *Thermal feedback* is a process in which gas parcel does not endure large scales flows, though it should alter the temperature of it. Non-ionizing radiations are known to be as main source of thermal feedback. In the star formation process, as gravitational potential energy turns to thermal and kinetic energy during collapse of cloud. This process ends up with formation of stellar core. After that it results in three types of thermal feedback:

- Radiation originating from the core itself
- Luminosity from accretion onto the star
- Luminosity from continued collapse of the cloud and disk accretion

1.4 Triggered Star Formation

The mechanism in which the role of some external factor to a specific region, which is driving some conditions for star formation activity, where other internal factors of that specific region are not decisive is called *Triggered star formation*. This condition can be accomplished by many ways, either directly altering the density distribution of cloud or may be by propagating the shock into cloud, which to some particular location in that specific region, achieves the jeans instability limit to make protostellar core.

These triggering events can be achieved with any of the feedback mechanism explained in previous section 1.3. Combining those feedbacks mechanism, two most popular trigger-

ing mechanisms have been proposed for triggered star formation, *Collect and Collapse* and *Radiation driven implosion* which are discussed in this section.

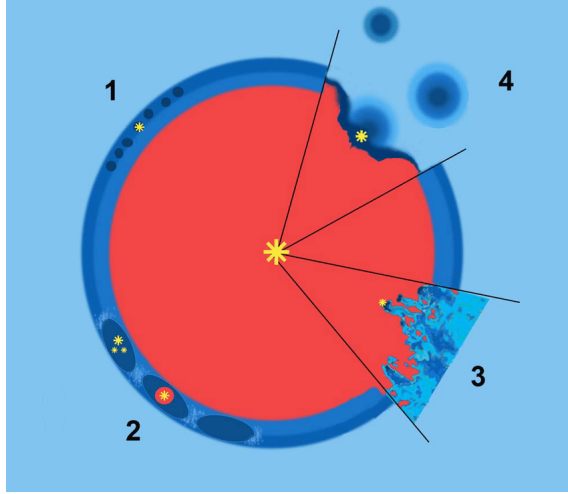


Figure 1.5: Schematic view of a H II region showing its second phase of expansion along with different mechanism of triggered star formation: (1) Small-scale gravitational instabilities; (2) Large-scale gravitational instabilities resulting in the formation of high-mass protostellar cores; (3) Ionizing radiation imploding on a turbulent ambient medium; (4) Radiation-driven implosion of pre-existing dense clumps (Deharveng et al. 2010).

1.4.1 Collect and Collapse

Collect and Collapse process is driven internally by massive stars that have formed inside a molecular cloud and is known to be a large scale process taking place on relatively long span of time, as it takes time for a sufficient mass of gas to be swept up by the fronts and achieves the jeans instability limit. The mass of gas required in this mechanism is also large enough to form many stars finally ending up as a formation of star cluster.

Collect and Collapse mechanism was first put forward by Elmegreen & Lada (1977). This is one of the simplest model to explain induced star formation. Whitworth et al. (1994) has studied this in great detail. When ionizing source turned on inside a uniform gas distribution, initial UV photon flux drives a spherical ionization front radially outward from the source. Velocity of the ionization front at this stage is much higher than the speed of sound in the cold neutral gas and the number of extra ionizing photons after ionizing the gaseous medium are still too large (see sec. 1.2.2). This is called as *R-type ionization front* (Kahn et al. 1954; Osterbrock 1974).

As the region expands, the gas inside the R-type ionization front also increases, also

Table 1.2: Classification of Ionization fronts

Ionization Front Type	Mach Number	Pressure	Density	Relative Velocity
Strong R	$M_1 > 1, M_2 < 1$	$P_2 > P_1$	$\rho_2 > \rho_1$	$v_2 < v_1$
Critical R	$M_1 > 1, M_2 = 1$	$P_2 > P_1$	$\rho_2 > \rho_1$	$v_2 < v_1$
Weak R	$M_1 > 1, M_2 > 1$	$P_2 > P_1$	$\rho_2 \geq \rho_1$	$v_2 \leq v_1$
Weak D	$M_1 < 1, M_2 < 1$	$P_2 \leq P_1$	$\rho_2 < \rho_1$	$v_2 > v_1$
Critical D	$M_1 < 1, M_2 = 1$	$P_2 < P_1$	$\rho_2 < \rho_1$	$v_2 > v_1$
Strong D	$M_1 < 1, M_2 > 1$	$P_2 < P_1$	$\rho_2 < \rho_1$	$v_2 > v_1$

it takes more and more photons to ionize the medium. This leads to decrease in speed of ionization front. As the speed of ionization front matches with the speed of sound of that medium, ionization front changes from R-type to *D-type ionization front* (at $\sim 10 \text{ kms}^{-1}$, for Hydrogen at 10^4 K) (sec. 1.2.3). This is at distance we know as Strömgren radius (sec. 1.2.1). The different properties of these ionization fronts are given in table 1.2. Here M_1 and M_2 are the mach number at the two sides of ionization front (subscript 1 corresponds to upstream and 2 corresponds to downstream) which is defined by the ratio of velocity of front to the sound speed in that medium (Newman & Axford 1968).

The expansion of H II region through the surrounding neutral gas is highly supersonic and drives a shock front sweeping up an increasingly massive and dense shell of cool and neutral medium. This is known as *Collect Phase*. In this phase ionization front acts as a snowplough. If this process continues for long enough such that the density, mass and temperature of the shell reaches the point where Jeans instability is touched and entire thing turns out to be a self gravitating. The shell will start going through fragmentation and then individual shell will start a non-linear *Collapse Phase* which finally leads to triggered star formation.

1.4.1.1 Collect and Collapse: Simulation

Study by Zavagno et al. (2006) claims the triggered star formation to be a result of the collect and collapse process. Using SEST-SIMBA 1.2-mm continuum maps and ESO-NTT SOFI JHK_S images of RCW 79, they have identified five large massive fragments along the borders of H II region. The two most massive fragments are found at diametrically opposite each other in shape of a ring.

Their formation has presumably been triggered by the pressure gradient induced collapse of a pre-existing molecular clumps. It is also a possibility that clumps might be

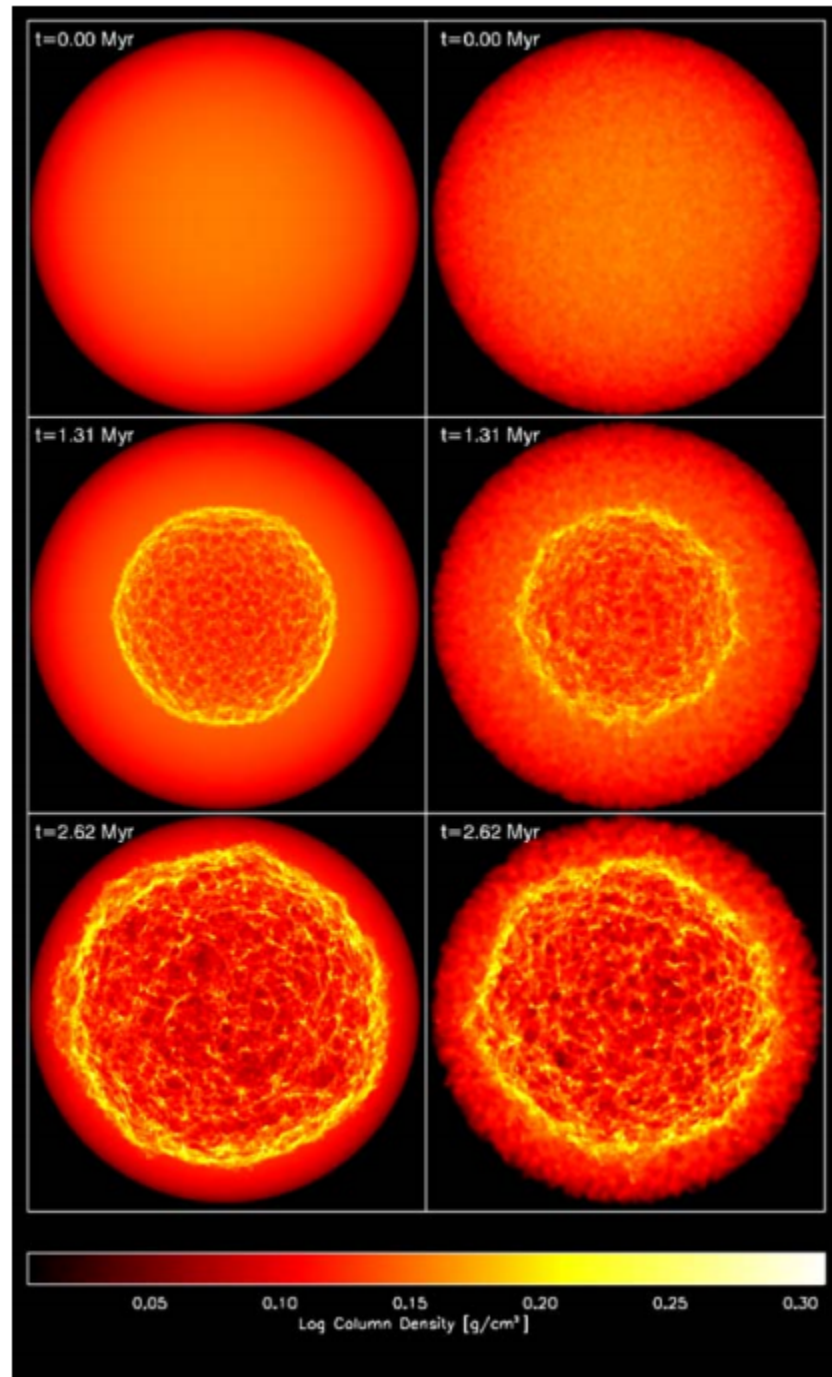


Figure 1.6: Column density maps (viewed along the z-axis) from three epochs of the smooth (left-hand column) and noisy (right-hand column) 1.3×10^6 particle simulation (Dale et al. 2007).

resulting from dynamical instabilities in the collected layer. The large and massive fragments observed at the periphery of RCW 79 found to be most probably result from the gravitational collapse of the layer of collected material by the ionization and shock fronts, according to the collect and collapse process.

This study has conducted smoothed particle hydrodynamics simulations of the collect and collapse mechanism for triggered star formation by an expanding H II region. It simulates the evolution of a uniform and spherical molecular cloud given that ionizing source i.e. a massive young star is present at its centre. Simulations are done using the smoothed particle hydrodynamics (SPH) code. Along with this, Collect and Collapse mechanism has been modelled and simulated with 3-D geometry.

The gas in the cloud is assumed to be self-gravitating, although the cloud is restricted from global collapse. In this dense gravitationally bound and contracting clumps of gas particles can be replaced by point masses called sink particles. This claims that the shell of material driven by the shock fronts in H II region fragments to form number of self-gravitating objects.

This model calculates parameters at four numerical resolutions to confirm that the model is a converging one. Comparing their results to their analytical model with the one presented in Whitworth et al. (1994) shows that their simulations agrees in the same sense that the shell fragmentation predicts at the time and radius given by simulations in Whitworth et al. (1994) to a given deviation by approximatley 20-25 %. Most of the massive fragments predicted in this study has two highest resolution calculations and they are approximately half the mass of those predicted by Whitworth et al. (1994).

They have also claimed that their results are robust against the presence of noise in the gas and that the initial particle distribution has no significant effect on the evolution of the system (see Fig. 1.6), but this conclusion is robust against both numerical resolution and the presence of random noise. In addition to this, several authors have modelled the expansion of H II regions in gas distributions with power-law radial density profiles (Tenorio-Tagle et al. 1986; Franco et al. 1990).

1.4.2 Radiation Driven Implosion

Studies on the stability of weak D-type ionization fronts, considering the effect of diffuse UV radiation caused by recombination to the ground state of hydrogen atoms, shows that weak D-type ionization fronts which reciprocates to the considerable portion of the evolution of H II regions, are expected to be stable against the growth of length scales larger than

0.2 pc. This implies that the hydro-dynamical instability could not be the formation mechanism of structures like elephant trunks, cometary globules, bright rimmed clouds etc. (Spitzer Jr 1954; Pottasch et al. 1956; Axford 1964). Molecular radio observations showed the presence of clumps (and fragmented structures) at periphery of molecular clouds, at elephant trunks or bright rimmed clouds (BRCs) usually been regarded as remnant cloud clumps left in expansion process of HII regions (Ogura 2010).

Unlike the collect and collapse model of triggered star formation, Radiation driven implosion (RDI) involves the photoionization of a pre-existing neutral dense cloud at the peripheral locations of a H II region (see fig. 1.5). This involves the exposure of neutral dense cloud to the ionization and shock fronts, which leads to the photoionization process of these clouds. To understand the RDI, it is must to first look at the physics behind the photoevaporation process (see 1.4.2.2). This is the first step to understand the formation and star formation inside the bright rimmed clouds, which is the soul of this project.

1.4.2.1 Radiation driven implosion: Simulations

Numerical calculations and simulations of the evolution of such clouds carried out by Lefloch & Lazareff (1994). This study involves dynamical evolution of a neutral hydrogen cloud exposed to the ionizing radiation of young OB stars. Results of this 2-dimensional hydrodynamical simulation present a detailed evolutionary process from the begining i.e. from cloud's collapse to the quasi-stationary phase of cometary evolution.

From the results of the simulations, they have generated maps of projected density , emission measure and position-velocity diagrams. Along with this, they claim that the second phase goes approximately 90 % of the cloud's lifetime. The maps of emission measure exhibit a striking resemblance to various bright-rimmed structures different kinds of cometary globules found in HII regions. Simulation shows that they are stable and supported by the magnetic fields. In addition to this, it also checks the gravitational stability of such cometary structures. They also derives the condition for the stability of the ionization and shock fronts in the cometary phase and presented it with results from the simulations.

They showed that the evolution is divided into three phases;

1. Cloud undergoes a short collapse phase ($\sim 10^5$ yr) with the maximum compression.
2. Cloud bounces in the temporary phase of re-expansions and re-compression
3. Cloud settles into a long-lived cometary phase ($\sim 10^6$ yr)

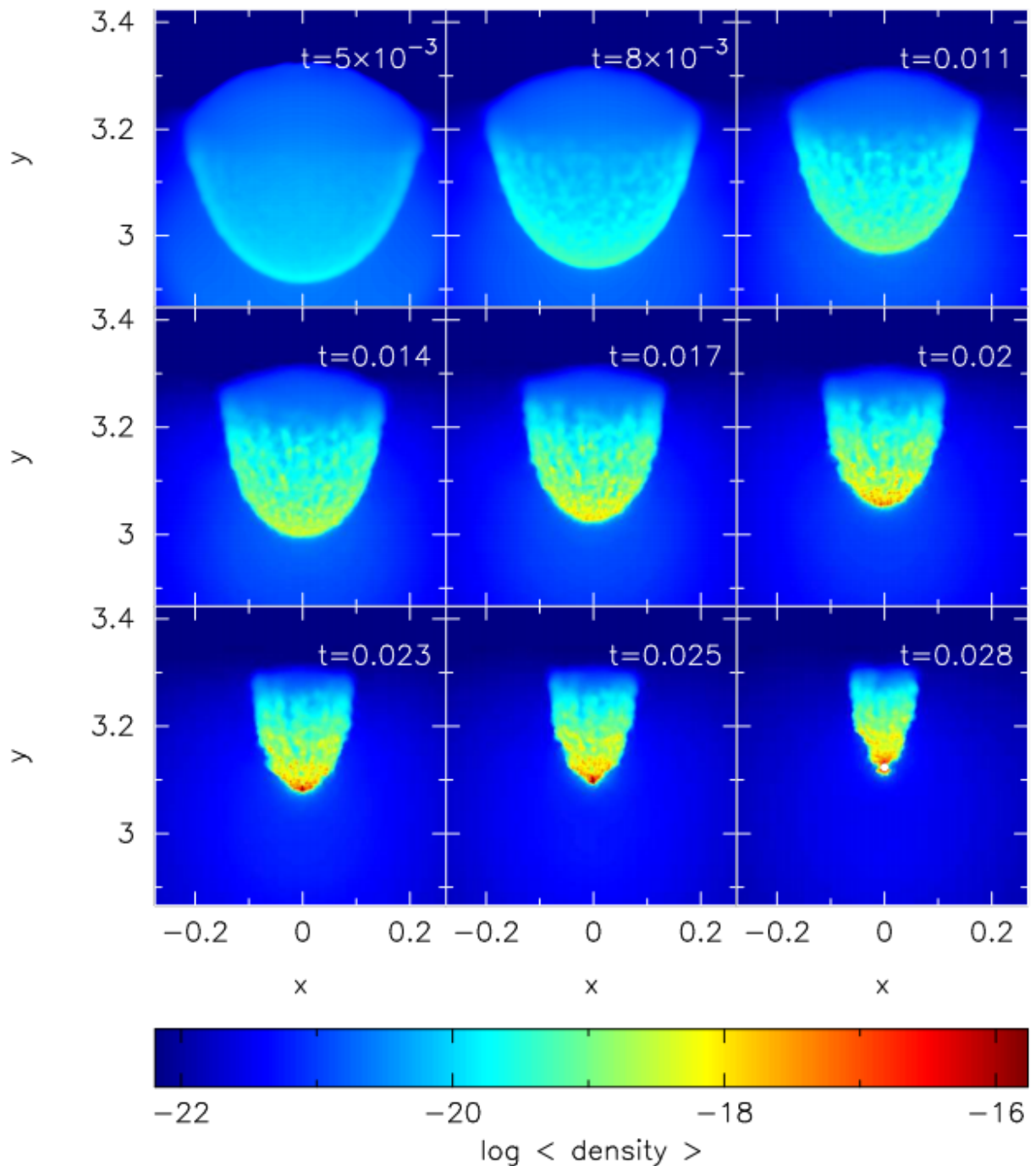


Figure 1.7: Time sequence of column-density images showing the evolution of the simulated cloud when it is exposed to a relatively high ionizing flux. t/Myr is given in the top right-hand corner of figure. The color bar shows the values of column density in log scale and axes are in parsec Lefloch & Lazareff (1994).

Kessel-Deynet & Burkert (2003) present three-dimensional simulation and calculations of a molecular clouds exposed to radiation driven implosion. This simulation involves self-gravity and ionization through diffuse UV radiation. It demonstrate that radiation driven implosion could be an efficient process for injecting disordered kinetic energy into neutral isolated clouds in the neighbourhood of massive stars. Results shows that the effects of density perturbations of globules, and show that the begining of gravitational collapse can be haulted for a various of the implosion time-scales. The simulation is shown in fig. 1.8

Following are the four different phases that one can identify from fig. 1.8

1. After the ionizing source is switched on, a weak R-type ionization front is propogated supersonically into the ambient H II region. After ~ 1.5 kyr, the denser region of the cloud is shovled and encircled by a region of ionized gas. The ionization front stalls and slows down to nearly sonic. It converts R-type ionization front into a weak D-type front, (fig. 1.8, top panels).
2. In the second phase, pressure imbalance drives a shock front into the cloud with velocity around 5 kms^{-1} which is approximatly equal to sound speed in that medium. The shock front sweps a thin layer of dense cloud shocked material (fig. 1.8, middle panels). Simulation starts converging to a finger-like structure ‘globule’. Giving that the structure depends on curvature of the ionization front once it enters the globule.
3. The globule reaches a stage of maximum compression about in 130 Myr (fig. 1.8, bottom panels). Considering the intense surge in pressure, the globule starts to expand again.
4. After that the structure enters the final phase, in which gas is ionized off the surface continuously facing the ionizing source. Thats how the bright rimmed cloud takes its shape.

Results shows that it will have mass loss of $10^{-4} M_{\odot} \text{yr}^{-1}$. Velocity of gas leaving the ionization front is estimated to be around 13 kms^{-1} . This causes a *rocket effect*, which accelerates the gas at the tip of the cloud towards the direction of photon flow i.e. towards the ionization source (see arrow in fig. 1.8).

This makes the structure in which the gas spreads within the globule in lid-shaped fashion which faces the ionization source. After about ~ 600 kyr, dynamical instabilities disintegrates the cloud partially and leaving behind the remaining fragments, which are after some tens of kyr, ionized completely and shaped into various structure that we observe like BRCs, pillars etc.

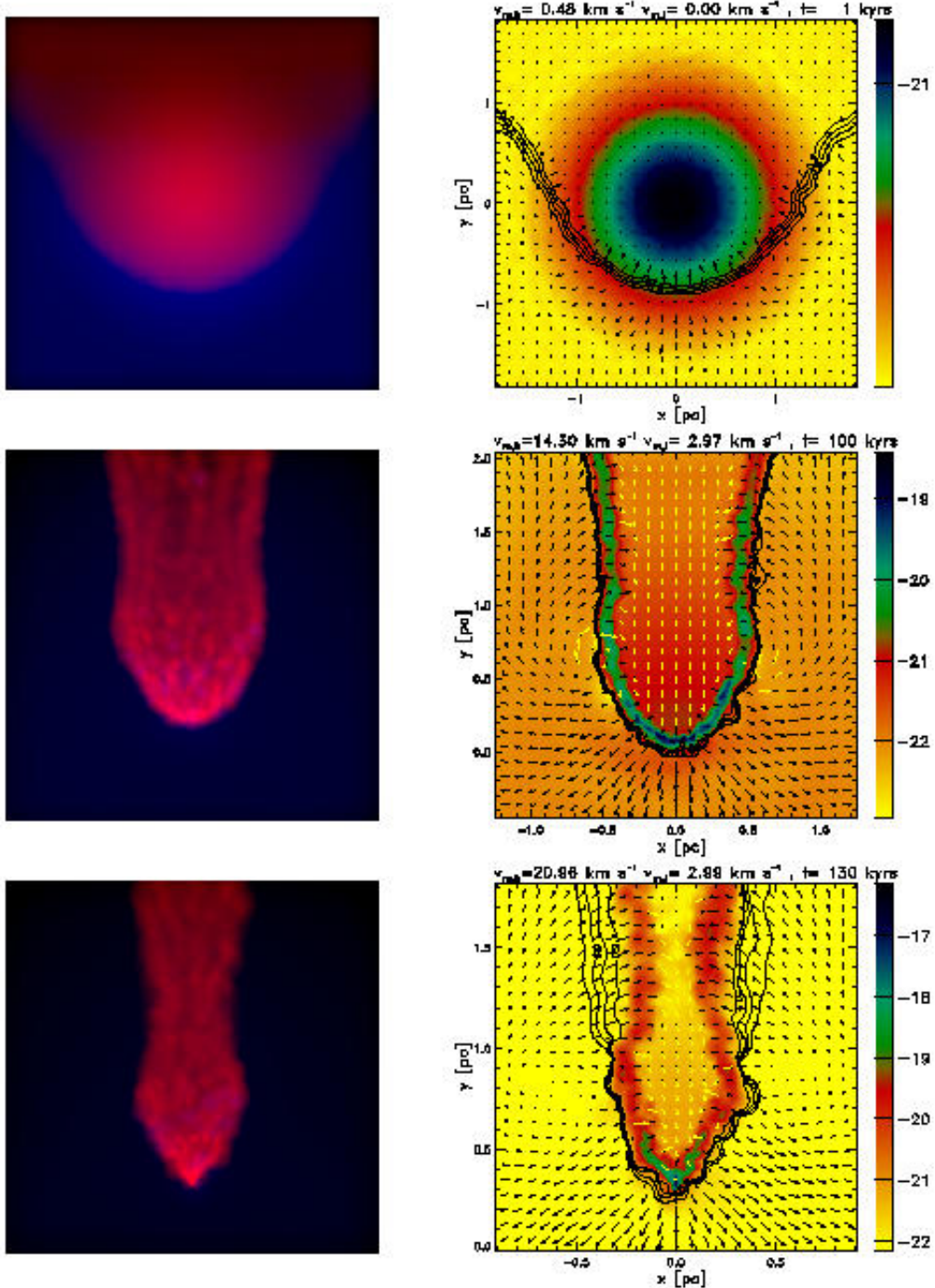


Figure 1.8: Time evolution of bright rimmed cloud. Three-dimensional projection of bright rimmed cloud is shown in left side. Right side column shows the evolution, color-coded with column density, contour shows the ionization fraction. Ionized gas is shown in blue, neutral gas in red (Kessel-Deynet & Burkert 2003).

In addition to these studies, there are several numerical simulation done to understand the radiation driven implosion and how it shapes different types of structure like BRCs, pillars, trunks etc. Although they all shows somewhat similer results, but they differe it from the other in various minor details (Pavlakis et al. 2001; Miao et al. 2006, 2009; Gritschneider et al. 2009; Henney et al. 2009; Bisbas et al. 2011)

Bright rimmed clouds (BRCs), Cometary globules, Pillars, Elephant trunks etc. are found in H II region and they are believed as the result of radiation driven implosion to the neutral dense cloud at the outskirts of expanding H II region. They are classified according to their appearance (Wasserburg et al. 1985). They found to have typical mass of about $0.3\text{--}100 M_{\odot}$, size of ~ 0.1 pc and density about $10^5\text{--}10^6 \text{ cm}^{-3}$. Their origin is supposed from *Rayleigh-Taylor instability* at the periphery of expanding H II regions and it was first proposed by Spitzer Jr (1954). This will be discussed in more detail in coming section 1.5.

1.4.2.2 Photoevaporation of Interstellar Cloud with Radiation Driven Implosion

In Fig. 1.9 a spherically symmetric cloud of neutral hydrogen is shown. The direction of ionizing photon flux is shown by arrows. The ionization front is shown at distance r_0 from the center of the cloud. The velocity of the ionization front depends on the density of the medium, normal and the direction to the star.

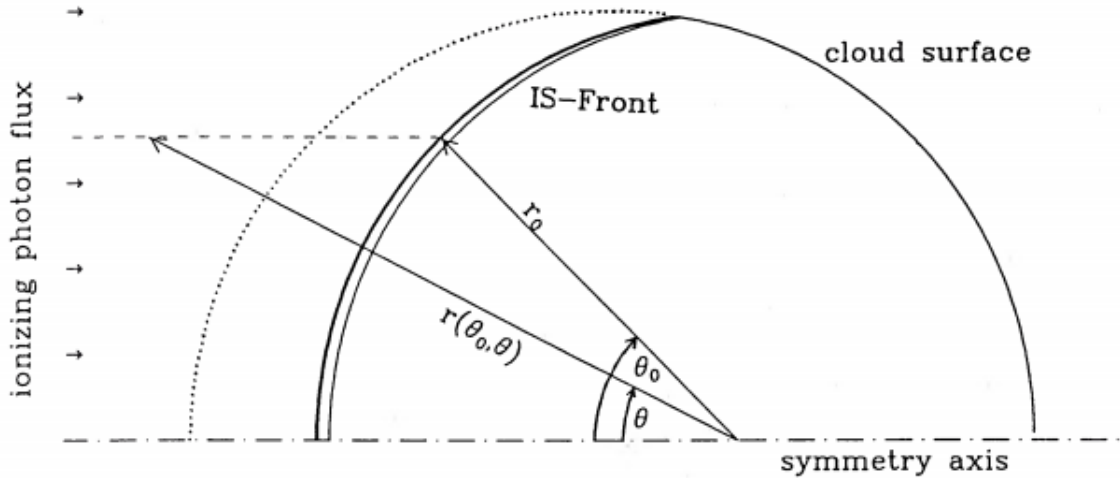


Figure 1.9: Dense cloud along the symmetry axis is shown (Only the top half portion). An ionization-shock front propagates into this initially spherical cloud. The ionizing photon flux at (r_0, θ_0) depends on the absorption along the dashed line toward the ionizing star (Bertoldi 1989).

The total ionizing flux reaching the I-front at some angle θ_0 is equal to the incident flux, F_i diminished by the number of recombination to excited levels of hydrogen in a column of unit cross section extending from the ionizing source to the point on the surface shown. The latter is specified by the radius of curvature of the front and the azimuthal angle from the axis: (r_0, θ_0) . The ionizing flux reaching the I-front at θ_0 is then;

$$F(r_0, \theta_0) = F_i - \int \alpha_{recomb} n_e^2 ds \quad (1.7)$$

where the integration is carried out along the line connecting (r_0, θ_0) with the ionizing star. Where the Lyman continuum flux at a distance R_0 from the ionizing source is given by;

$$F_i = \frac{S}{4\pi R_0^2} = 8.36 \times 10^{10} \frac{S_{49}}{R_{0,pc}^2} s^{-1} cm^{-2} \quad (1.8)$$

where S is the central ionizing star's emission rate of photon beyond Lyman limit.

Consider the point on the cloud surface closest to the star, the Lyman continuum flux here is such that conditions are M-type, i.e. ionization front drives a shock into neutral gas, compressing it to such pressure that ionization front are approximately D-critical. The initial shock velocity at the symmetry axis, V_0 can be calculated by equating the shock ram pressure $\rho_0 V_0^2$ to the total pressure at D-critical point such that;

$$v \equiv \frac{V_0}{c_i} = \left(\frac{2F_i}{n_0 c_i} \right)^{1/2} = 12.1 \left(\frac{S_{49}}{n_{0,3} R_{0,pc}^2} \right)^{1/2} \quad (1.9)$$

Notice that the velocity of shock front is inversely proportional to number density in cloud (Bertoldi 1989). In Fig. 1.9, the velocity of the shock front will be different at different geometrical positions of the cloud. Which implies that velocity of the portion of shock front which propagates along the symmetry axis will trail the shock front which propagates along the direction offset to symmetry axis as shown in fig. 1.9.

1.5 Bright Rimmed Clouds

We have discussed the formation mechanism and the evolution of bright rimmed cloud in detail in section 1.4. The evolution of a neutral dense cloud of hydrogen to become an ionized cometary shaped structure is a long process and takes several kyr to finally get its final shape. Only after it hits the Rayleigh-Taylor instability and Jeans instability mass, star formation process begins.

Almost every aspect of formation and evolution of Bright Rimmed Clouds have been studied in great detail. Pioneering work done by Oort, Spitzer and Kahn on the structure and evolution of steady photo-evaporation gas flow off spherical ionization front that helped in understanding the physical processes in these regions (Oort et al. 1955; Kahn et al. 1954; Kahn 1958, 1969). The first complete theory of photo-evaporation of interstellar clouds was put forward in Bertoldi (1989); Bertoldi & McKee (1990).

In this section we have discussed several properties of various BRCs like their classification, star formation scenario, spatial distribution, YSOs classification, Initial Mass Function (IMF), Spectral energy distribution (SEDs), small-scale sequential star formation etc.

In addition to that, Wasserburg et al. (1985) classified the observed clumps in these regions according to their appearance. Their shape is typically spherical or elongated and directed away from the main ionizing source. We have seen in section 1.4.2 that the bright rims are seen on the cloud's side facing the ionizing source (Pottasch et al. 1956, 1958; Pottasch 1958).

The dense shells surrounding H II regions as well as the neutral globules have been cited as possible centers for star formation (Elmegreen & Lada 1977; Sandford et al. 1982). Understanding the evolution of neutral condensations is the key to answering the question, whether star formation can be triggered by the dynamical effects of O and B stars.

Detailed model that we have discussed in section 1.4.2.1, calculations of the RDI process have been carried out by several authors (Bertoldi 1989; Lefloch & Lazareff 1995; Kessel-Deynet & Burkert 2003; Miao et al. 2006). BRCs are generally believed to be the sites of RDI. Many BRCs are indeed associated with Herbig-Haro (HH) objects, and Infrared Astronomical Satellite (IRAS) point sources indicative of recent star formation.

1.5.1 Classification of Bright-Rimmed Clouds

The bright-rimmed clouds are classified into three types according to their rim morphology: (1) Type A, moderately curved rim; (2) Type B, tightly curved rim; and (3) Type C, cometary rim.

Their rim sizes, length (L), and width (W), are defined in Fig. 1.10. Type A should have a length to width ratio, L/W , less than 0.5, and type B greater than 0.5. The range of their sizes is 0.2-3 pc and most of them are less than 1 pc. The average lengths and widths of these three types of rims are given in the table 1.3 (Sugitani et al. 1991).

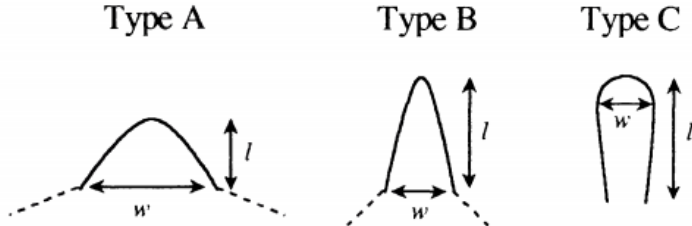


Figure 1.10: Classification of the rim shape (Sugitani et al. 1991). Relation between W and L for all three types of BRCs shown above are given in table 1.3.

Table 1.3: Classification of BRCs

Morphology	L	W	X (L/W)	Feature
A	0.39	1.0	$X < 0.50$	Moderately Curved Rim
B	1.0	1.20	$0.5 < X < 1.0$	Tightly Curved Rim
C	0.58	0.18	$X > 1.0$	Cometary Rim

1.5.2 Observations of BRCs and SFO catalogs

Table 1.4: H II Regions in Northern hemisphere selected by Sugitani et al. (1991)

H II region	Size (arcmin)	d (kpc)	Other Name
S49	90	2.20	M16
S117	240	1.00	NGC7000
S131	170	0.75	Cep OB2
S142a	30	2.40	Cep OB1
S145	90	0.91	
S171	180	0.85	NGC7822
S185	120	0.19	γ Cas
S190	150	1.90	IC1805
S199	120	1.90	IC1848
S236	55	3.40	IC410
S249	80	1.60	
S264	390	0.40	λ Ori
S273	250	0.78	NGC2264
S275	100	1.42	Rostee Nebula
S276	1200	0.40	Barnard's loop
S277	120	0.40	S434
S281	60	0.46	Orion Nebula
S296	200	1.15	CMa OB1

Three well known sites of radiation driven implosion were reported by Sugitani (1989). After that, using Palomar sky survey, the same group has considered 44 BRCs which are associated with IRAS sources which were also considered as an excellent site for triggered star formation induced by RDI (Sugitani et al. 1991). Out of these, about 9 BRCs had been reported as source associated with the molecular outflow activity. Two of them are associated with HH objects. Size of most of the BRC sources were found to be within 1 pc which are comparable to Bok globules. The luminosities of the such associated IRAS sources are relatively large, about 10 to 10,000 L_{\odot} . IRAS luminosity to cloud mass ratios found to be more than those in dark globules or in dense cores in dark cloud complexes.

These 44 BRCs were then cataloged and now they are known as *SFO catalog*. Since these are the

sources which belongs to the northern hemisphere, hence this is considered to the first part of the catalog. The H II region associated with these BRCs from the northern hemisphere are listed in table 1.4 with there approximate size and there distances.

Next part of the same catalog involves regions from southern hemisphere. Forty-five bright-rimmed clouds associated with IRAS point sources selected ESO (R) Atlas. Four of them are associated with HH objects and three sources with molecular outflows. Like the first part of catalog, this catalog has most of their sizes less than 1 pc. The luminosities of the associated IRAS sources are approximately $20L_{\odot} - 3 \times 10^4 L_{\odot}$.

About 80% of the BRCs have radii of <0.5 pc. Forty percent of the clouds found to have small masses of $<100 M_{\odot}$. About 40% of the associated IRAS sources have spectral energy distributions of the type I and about 30% have spectral energy distributions of the type II (see 1.6.2 for the classification of YSOs based on their spectral index). The H II region associated with these BRCs from the northern hemisphere are listed in table 1.5 with there approximate size and their distances.

In addition to this, a molecular outflow survey of the northern BRCs have been carried out by the same group with the KOSMA (Kolner Observatorium for Submillimeter Astronomy) 3 m telescope in order to look for evidence of molecular outflows with CO(J=2-1) and CO(J=3-2) transitions.

Table 1.5: H II Regions in Southern hemisphere selected by Sugitani & Ogura (1994)

H II region	Size (arcmin)	d (kpc)	Other Name
S306	30	4.40	
S307	6	2.45	
RCW14	60	1.55	
Gum Nebula	2000	0.45	
NGC2626	100	0.95	Pup R2
RCW27	100	1.15	
RCW32	27	0.70	
RCW38	40	1.20	vdB26
NGC3503	120	2.88	Car R1
BBW347	45	2.70	Stock 13
RCW62	80	1.66	IC2944
Cen R1	30	2.00	vdB59
RCW75	18	1.90	Stock 16
RCW85	20	1.17	
RCW98	11	3.60	
RCW105	45	1.80	
σ Sco	50	1.65	σ -Oph
RCW108	210	1.32	NGC6193
RCW113	300	1.75	NGC6231
RCW134	60	1.26	Sco R7
M8	90	1.38	NGC6530
Simeis 188	40	1.38	

1.5.3 Star Formation in Bright Rimmed Cloud

As Sugitani et al. (1991); Sugitani & Ogura (1994) found that the BRCs are extreamly important site for checking the radiation driven implosion affecting on the star formation activity. They have found number of young stellar objects (we will see YSOs in detail in section 1.6) within them and claimed these sites as active star forming regions. Infact,

Sugitani et al. (1991) claimed that, stars formed through the RDI activities are expected to contribute $\sim 5\%$ of the total stellar mass in the Galaxy as well as a significant number of intermediate mass stars may be formed in BRCs around H II regions.

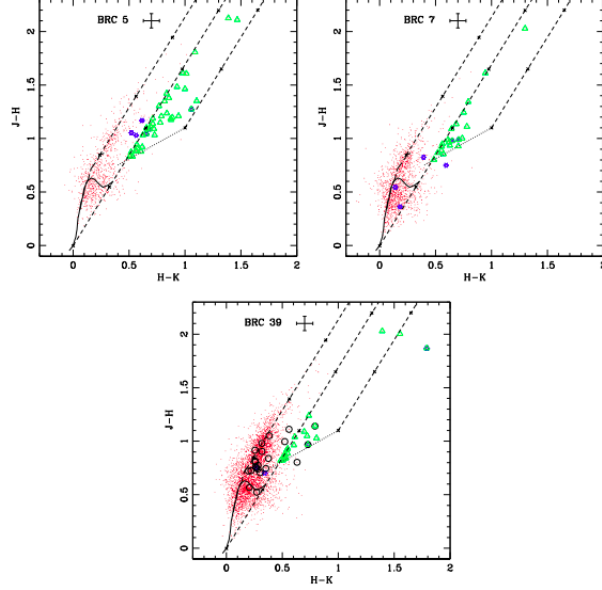


Figure 1.11: (J-H)/(H-K) NIR colour-colour diagrams. Open triangles represent NIR excess stars and blue asterisk represent the $H\alpha$ emission sources. The continuous and dashed curves represent the intrinsic MS and giant locus respectively (Bessell & Brett 1988). The dotted line represents the intrinsic colours of CTTSs (Meyer et al. 1997), and the parallel dashed lines are the reddening vectors with crosses separated by $AV = 5$ mag. The error bars in the top middle show average errors in the colours. (Panwar et al. 2014).

Another study by Sugitani et al. (1995) used 44 BRCs in NIR observation that revealed elongated aggregates of YSOs around BRCs with older stars near ionizing source. In six BRCs, the point sources are elongated toward the ionizing source. There is a tendency for bluer stars to be located closer to the ionizing source and for redder stars to be closer to the IRAS sources. This asymmetric distribution suggests small-scale sequential star formation i.e. propagation of star formation from the side of the ionizing source to the IRAS position in a few times 10^5 yr, as a result of the advance of the shock caused by the UV radiation from the ionizing source.

Study by Panwar et al. (2014) also found young stars at the head of BRC 7, BRC 5 and BRC 39. These are low mass stars of range $0.5-2 M_\odot$. In their approach to YSO identification, they have used three ways, first using $H\alpha$ emission survey, second using 2MASS/IRAC photometry and third using WISE survey. For BRC 5, 7 and 39, the NIR color-color diagram (J-H)/(H-K) from this study is shown in fig. 1.11. The identified YSOs

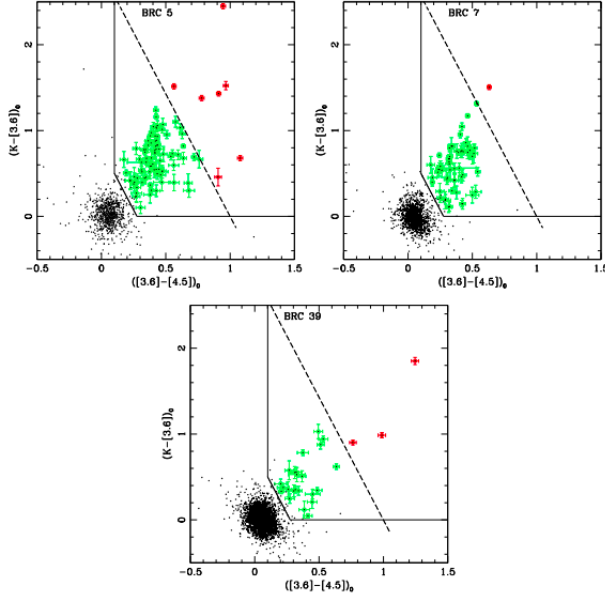


Figure 1.12: Colour-Colour diagrams for BRC 5, BRC 7 and BRC 39. Red squares and green circles are Class I sources and Class II sources respectively. The continuous lines and dashed lines are the criteria used by Gutermuth et al. (2009). The error bars show the errors in the respective colours of Class I and Class II sources. (Panwar et al. 2014).

are shown here with open triangles and H α emission sources with open circles (for more detail on NIR CC diagram and YSO identification see section 1.6).

Similarly with 2MASS-IRAC sources, they have identified more YSOs, which were not first identified with the previous method. The color-color diagram for this is shown in fig. 1.12. They have used criteria from Gutermuth et al. (2009). The class I sources are shown in red squares and class II sources by green circles. With this method, they have identified 7 class I, 86 class II in BRC 5, 1 class I and 55 class II in BRC 7 and 3 class I, 25 class II in BRC 37.

Using WISE survey 9 class I, 11 class II in BRC 5, 4 class I and 20 class II in BRC 7 and 6 class I, 19 class II in BRC 37. The CC diagram using WISE data is shown in fig. 1.13, green circle and red square are showing class II and class I sources respectively.

1.5.4 Mass and Age estimation at BRCs

Bright rimmed clouds are active star formation sites of low mass stars. Chauhan et al. (2011) have studied W5 H II region. It has three BRCs namely, BRC 13, BRC 14 and BRC NW. By considering photometric data from 2MASS, MIR-spitzer data, they have estimated the mass and the age of the YSOs in all the three BRCs. To identify the YSOs, they have

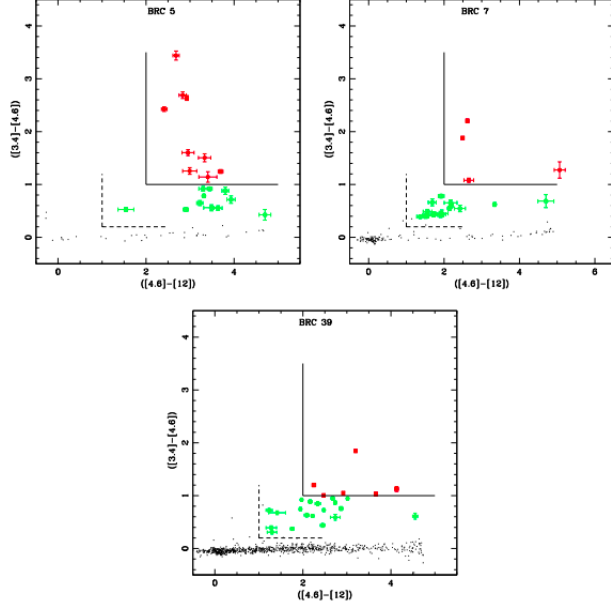


Figure 1.13: colour-colour diagrams for BRC 5, BRC 7 and BRC 39. Red squares and green circles are Class I sources are Class II sources respectively. The continuous lines and dashed lines are the criteria used by Koenig et al. (2011). The error bars show the errors in the respective colours of Class I and Class II sources. (Panwar et al. 2014).

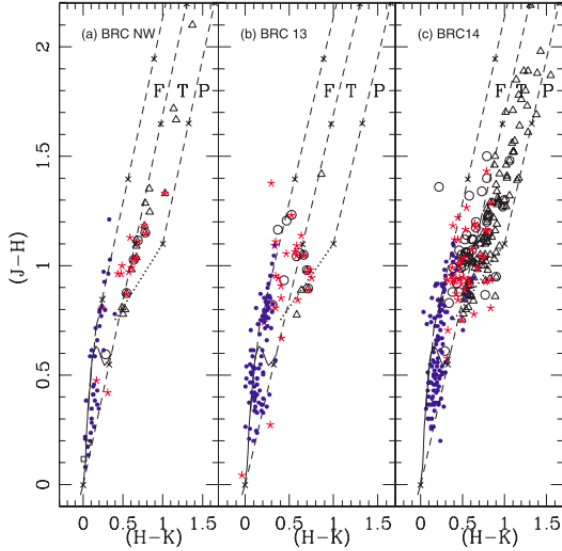


Figure 1.14: Near-infrared color-color diagram $(J-H)/(H-K)$. The Continuous curves shows the intrinsic locus of Main sequence (below) and Giants(above). The dashed lines are reddening vectors. The dotted lines are showing color of from ideal blackbody distributions (Chauhan et al. 2011).

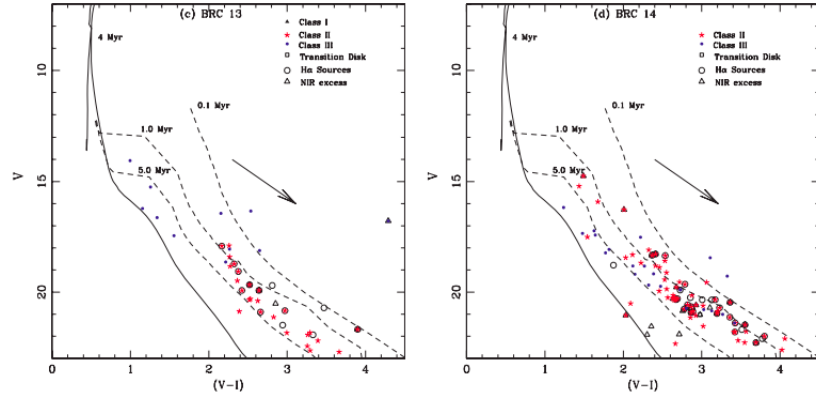


Figure 1.15: V/(V-I) color-magnitude diagram for BRC 13 and BRC 14. It shows 0.1, 1.0 and 5.0 Myr from Siess et al. (2000). Isochrones are corrected for distance and mean reddening. (Chauhan et al. 2011).

used method described in section 1.6.1. The NIR (J-H)/(H-K) CC diagram is shown in fig. 1.14. Mass of the YSOs estimated by using V/(V-I) color-magnitude diagram (CMD) as explained in Pandey et al. (2008); Chauhan et al. (2009). The CMD is shown in fig. 1.15. The resultant mass distribution for both of the BRCs is shown in fig. 1.16. They have also estimated the mean age of the YSOs inside and outside the rim of the BRCs. They are given in table 1.6. A similer analysis has done by Panwar et al. (2014) for BRC 5, BRC 7 and BRC 39. They are also shown in table 1.6.

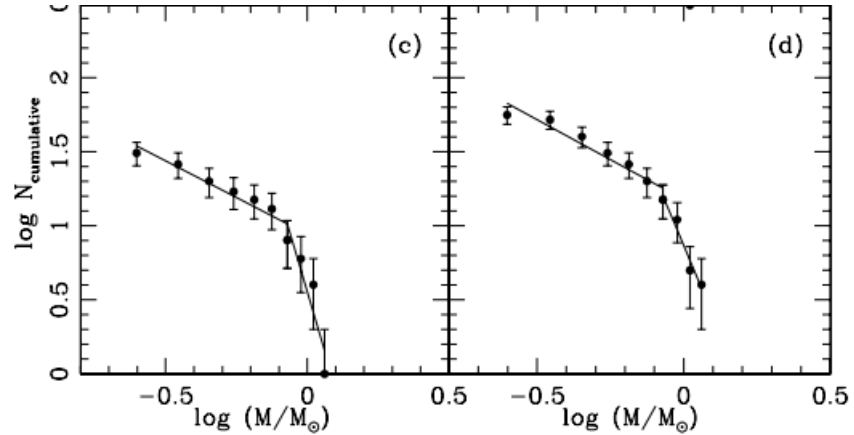


Figure 1.16: Cummulative mass function (CMF) for BRC 13 (c) and BRC 14 (d). The error bars represents poission error (Chauhan et al. 2011).

It is interesting to note that the CMFs (fig. 1.16) of the these BRCs show a break in the slope at $\sim 0.8 M_\odot$. The slopes in the mass range $0.2 \leq M/M_\odot \leq 0.8$, for both the BRCs are almost same.

Table 1.6: Mean age inside/on and outside the rim

Region	Mean age inside/on the rim (number of YSOs)	Mean age outside the rim (number of YSOs)
BRC NW	0.92 ± 0.56 (12)	1.29 ± 0.54 (19)
BRC 13	1.61 ± 1.41 (10)	2.44 ± 1.37 (24)
BRC 14	1.01 ± 0.73 (18)	2.32 ± 1.22 (58)
BRC 5	1.76 ± 1.17 (19)	2.06 ± 1.24 (17)
BRC 7	0.92 ± 0.74 (12)	1.35 ± 0.77 (26)
BRC 39	2.01 ± 1.65 (5)	2.51 ± 1.31 (15)

Ogura et al. (2007) has studied age sequence in small clusters associated with BRCs. They have used dereddened BVI_c photometry in 4 BRCs, BRC 11NE, BRC 12, 14 and 37. In this region they have estimated extinction in same region using JHK_s photometry. Using CMD $V/V - I_c$, they have estimated age of the every point sources. Since the age estimate from CMD depends on adopted distance and distances were not well measured, so the age estimate has poor standard deviation. Although they have quantitatively showed that mean age of YSOs inside the bright rim are relatively younger than outside sources.

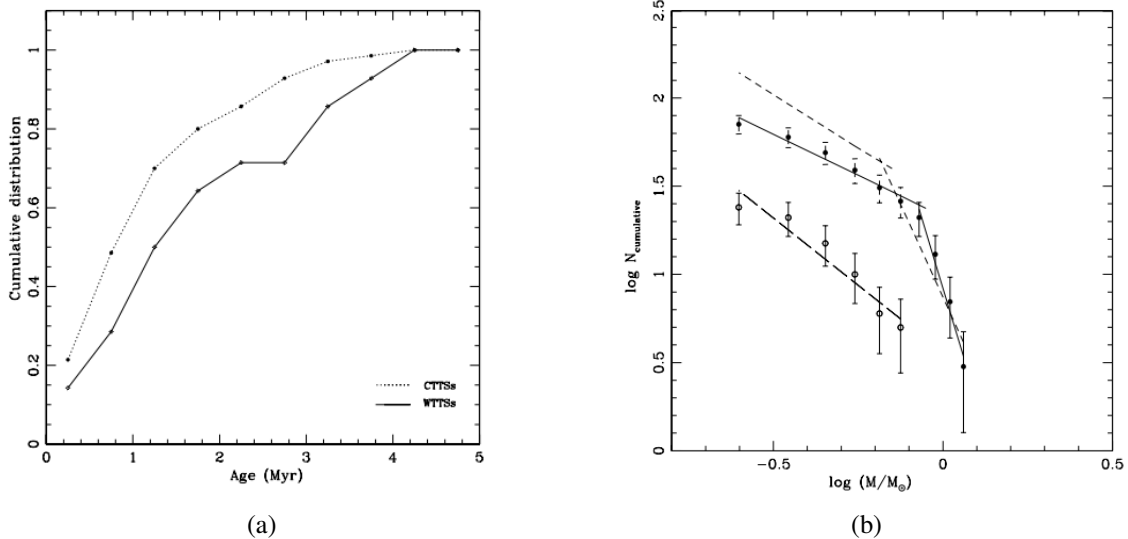


Figure 1.17: (a) Cumulative age distributions of CTTSs and WTTSs as a function of stellar age. Solid line shows the age distribution for CTTSs and dashed line shows for WTTSs. Age axis is labelled in million years. (b) Cumulative mass function of the A-type (filled circles) and B/C-type BRCs (open circles). Error bars represent poissionion errors. The CMF for the standard MF is shown by short dashed lines (Chauhan et al. 2009).

Similar study was done by Chauhan et al. (2009) for 6 more BRCs following the study

of Ogura et al. using optical and NIR analysis. In conclusion, they have estimated ages of individual stars in BRCs in CMD after doing reddening correction. By comparing mean age of sources inside and outside the bright rim. The age and mass distributions are shown in fig. 1.17 .

1.5.5 Some other properties of BRCs

In addition to this, many authors have also studied triggered star formation in different regions. Study by Karr & Martin (2003) shows example of interaction between massive young stars and surrounding interstellar medium. The target region of their study is W5 H II region. They have quantitatively shown that star formation rate is higher towards the edges of H II regions. Fig. 1.18 shows the number density of sources as function of distance to the H II region for YSOs selected sources (solid line) and non YSO sources (dashed line) and random points (triple dot dashed line).

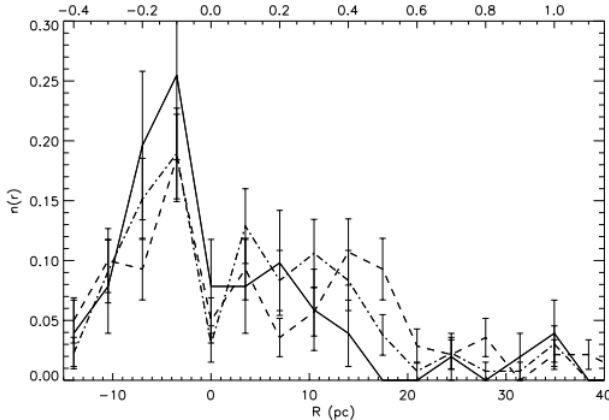


Figure 1.18: Number density of sources as a function of the distance to the H II region for YSO-selected sources (solid line), non-YSO sources (dashed line), clump centers (dot-dashed line), and a random sample of points (triple-dot-dashed line). The upper axis shows angular scale in degrees and the lower axis linear scale, assuming a distance of 2 kpc. Negative distances indicate sources inside the H II region (in projection); note the strong peak there. Error bars are Poissonian. Karr & Martin (2003)

There are some studies on the structural analysis and star formation efficiencies in BRCs. Sharma et al. (2016) have done this observations on 8 BRCs by identifying YSOs of different classes. In addition to it, they have also obtained a linear relation between number of YSOs and density of cloud. Also they have found a higher star formation efficiency (fig. 1.19). The star formation efficiency (SFE) is defined by the percentage of neutral hydrogen gas mass converted into stellar mass. Recent study by Evans II et al. (2009) indicated

that YSO clustering of higher surface density leads to show higher SFE than lower surface density.

Sugitani & Ogura (1994) found that elongated small clusters or aggregates of YSOs aligned towards the direction of the ionizing star. These YSOs showed a tendency that ‘redder’ (relatively younger) stars tend to be located closer to the BRCs, and relatively ‘bluer’ (relatively older) stars are found outside/away the clouds, indicating an age gradient. This hypothesis is called *small-scale sequential star formation (S⁴F)*. If the BRCs is relatively large, the star formation might have propagated along the axis of the BRCs as the ionization front and shock front advances towards into the molecular cloud (Kessel-Deynet & Burkert 2003).

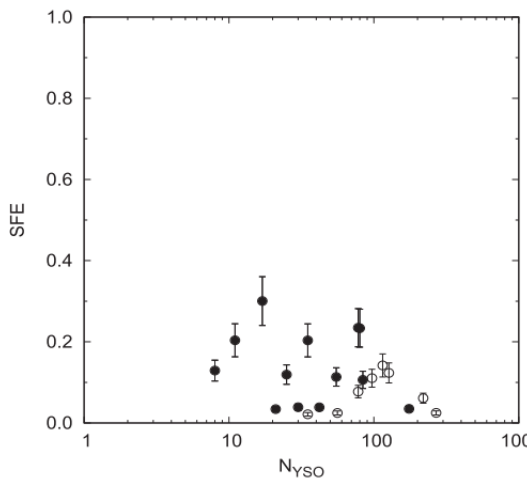


Figure 1.19: Star formation efficiency in the cores (filled circles) and in the active regions (open circles) with respect to the number of YSOs. Sharma et al. (2016)

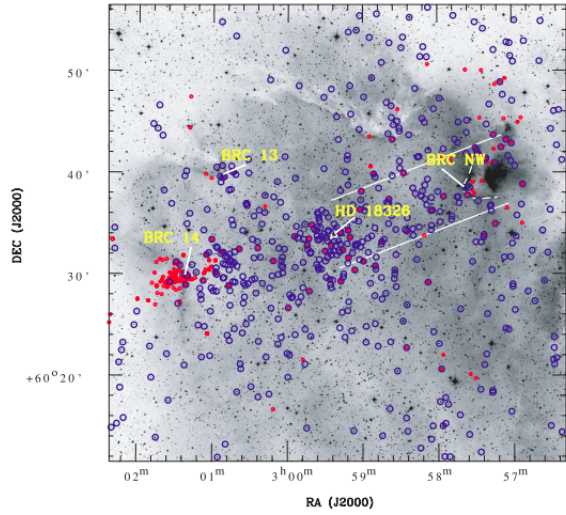


Figure 1.20: Distribution of YSOs in the W5E H II region. Small red circles show the locations of NIR-excess sources, whereas the large blue circles show the YSOs identified using the Spitzer observations (Stahler & Palla 2008).

One of such evidence is presented by Chauhan et al. (2011). The global distribution of YSOs identified (as mentioned in section 1.5.3) by NIR-excess sources and spitzer data is shown in fig. 1.20. This shows that the young sources with higher NIR-excess (larger A_V) with the age estimated shows a age gradient from center of the ionizing cluster towards the BRCs. This suggested that the process of radiation driven implosion in past begin from center of H II region towards the present location of BRCs.

1.6 Young Stellar System

As explained earlier, the life cycle of stars starts with dense core, which further evolves as a pre-main sequence star or *Young stellar object* (YSOs). This section will deal with the ways to understand the evolution and identification of such object along with their classification.

The pre-main sequence object are embedded within the envelop (or surrounded by disk if it evolved) of gas and dust. This gas and dust provides obscuration of light such that it is not possible to see such object in visible wavelengths. Though these structures are characterized to re-emit the energy of absorbed radiation as near infrared radiation, hence such objects are identified as NIR excess sources.

1.6.1 NIR Color-Color Diagram

The basic photometric method to identify such young objects with near-infrared excess, which often consider K-band observations with J-band and H-band. The main technique here is to study *Near infrared color-color diagram* which is shown in fig. 1.21. The $(J - H)$ and $(H - K)$ color indices are displayed as the vertical and horizontal axes, respectively. The solid curve shows the relation between these indices for main-sequence stars (lower branch) and giants (upper branch). The dotted curve shows the colors of blackbody spectra at the indicated temperatures. Straight dashed lines indicate the relative color changes due to interstellar reddening.

To obtain this relationship, consider that stellar surface radiates as perfect blackbody, such that for an unique temperature T_{eff} , the ratio of fluxes at any two wavelengths will be unique. This is shown as dotted line in fig. 1.21. Though stellar ph-

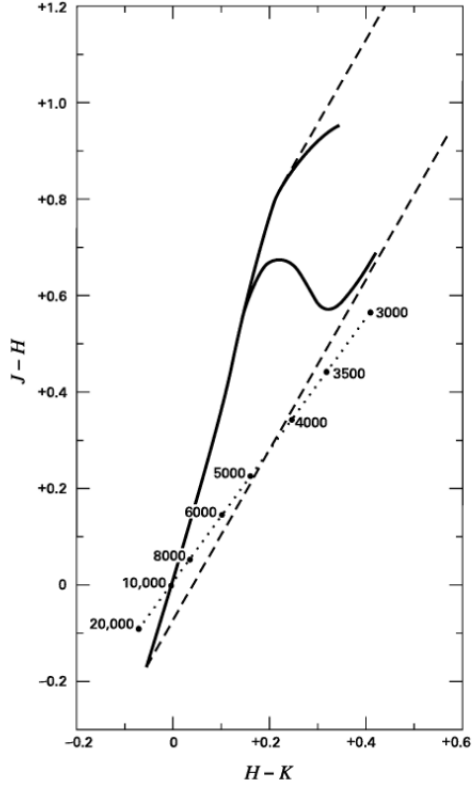


Figure 1.21: NIR CC diagram $(J - H)/(H - K)$. Solid curves shows the intrinsic locus of Main sequence (below) and Giants(above), dashed lines are reddening vectors and dotted lines are showing color of from ideal blackbody (Stahler & Palla 2008).

tosphere deviates from perfect blackbody because they are not equally opaque at all wavelengths. There are many dominant sources of opacity like H^- ion, electron scattering etc. (Prialnik 2000; Carroll & Ostlie 2017).

H^- opacity has broad minimum at about $1.6 \mu\text{m}$ which falls close to H-band. This implies that for redder stars that emit much energy in this regime will have NIR color which will differ significantly from blackbodies. This deviation is shown in solid curve in fig. 1.21, which is showing a set of photospheres for both main-sequence stars and giants.

As we move towards lower temperature, the surface opacity is increasingly dominated by molecular lines. A prime source in NIR is CO. The depth of CO absorption lines is lower in case of giants. Hence the solid line divides into two parts, at the spectral type of early K. The upper branch represents giant, while lower represents main sequence (Bessell & Brett 1988; Meyer et al. 1997).

This same analysis is done for classical T-Tauri stars (CTTS) (Meyer et al. 1997). The value of color excess E_{J-H} and E_{H-K} depends on the column density, but it can be estimated generally for interstellar medium by using extinction curve and is given by Stahler & Palla (2008):

$$\frac{E_{J-H}}{E_{H-K}} = 1.74 \quad (1.10)$$

This implies that for any background star with intrinsic color $(J - H)_o$ and $(H - K)_o$, the observed colors lie along the reddening vectors given by;

$$(J - H) - (J - K)_o = 1.74[(H - K)_o - (H - K)_o] \quad (1.11)$$

Stars which do not belong to the star forming region i.e. background stars or *Field stars* fall inside the two dashed curves. The parallel dashed lines are called *Reddening vectors*. They are drawn from the tip (\sim spectral type M4) of giant branch (left most reddening vector), from the base of main sequence branch (\sim spectral type A0) which is middle vector and from the tip of intrinsic CTTS line (right reddening vector). There are many studies on reddening vectors (Cohen et al. 1981; Rieke & Lebofsky 1985; Flaherty et al. 2007; Indebetouw 2015). Fig. 1.22 shows a color-color diagram for IRAS 06055+2039 region which uses reddening law of Rieke & Lebofsky (1985).

For clarity, sources are classified the CC diagram into three regions (Fukuda et al. 2002; Ojha et al. 2004a,b). The *F type sources* are located within the reddening bands of the main sequence and the giant stars. These sources are generally considered to be either field stars, Class III objects, or Class II objects with small NIR excess. *T type sources* populate the

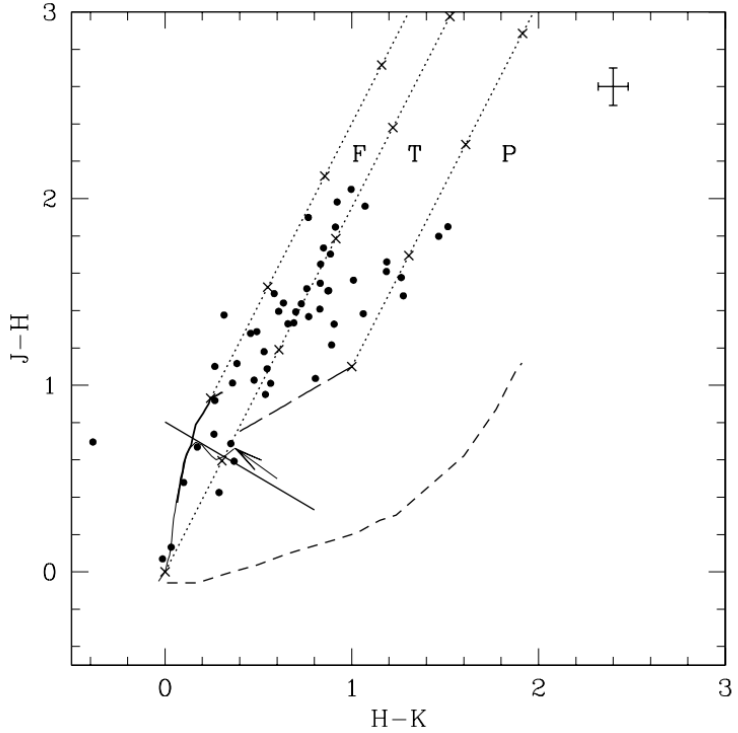


Figure 1.22: Near-infrared color-color diagram for IRAS 06055+2039 region. The two solid curves represent the loci of the main sequence (thin line) and the giant stars (thicker line) (Bessell & Brett 1988). The long-dashed line is the classical T Tauri locus (Meyer et al. 1997). The parallel dotted lines are reddening vectors with the crosses placed along these lines at intervals corresponding to five magnitudes of visual extinction. Reddening law used is ($A_J/A_V = 0.282$; $A_H/A_V = 0.175$; $A_K/A_V = 0.112$) (Rieke & Lebofsky 1985). The plot is classified into three regions namely **F**, **T**, and **P** (see text for details) (Tej et al. 2006).

region redward of the F region but blueward of the reddening line corresponding to the red end of the T Tauri locus. These sources are classical T Tauri stars (Class II objects) with large NIR excess or Herbig AeBe stars with small NIR excess. Redward of the T region is the P region, which has mostly protostar-like Class I objects and Herbig AeBe stars, namely *P type sources* (Tej et al. 2006).

1.6.2 Spectral Energy Distribution and Classification of YSOs

Since the infrared excess of young stars are because of excess emission relatively close to stellar surface, hence this is a *circumstellar* rather than *interstellar* process. It is rather easy to use A_V to calculate A_λ for cloud. With this the stellar population is *dereddened* and its spectral energy distributions (SEDs) is constructed. Fig. 1.23 shows SEDs for three

sources SR 20, SR 24 and WL 12 which are located in ρ Ophiuchi dark complex Adams et al. (1987). Fig. 1.23 also includes a blackbody curve of $T = 2300K$.

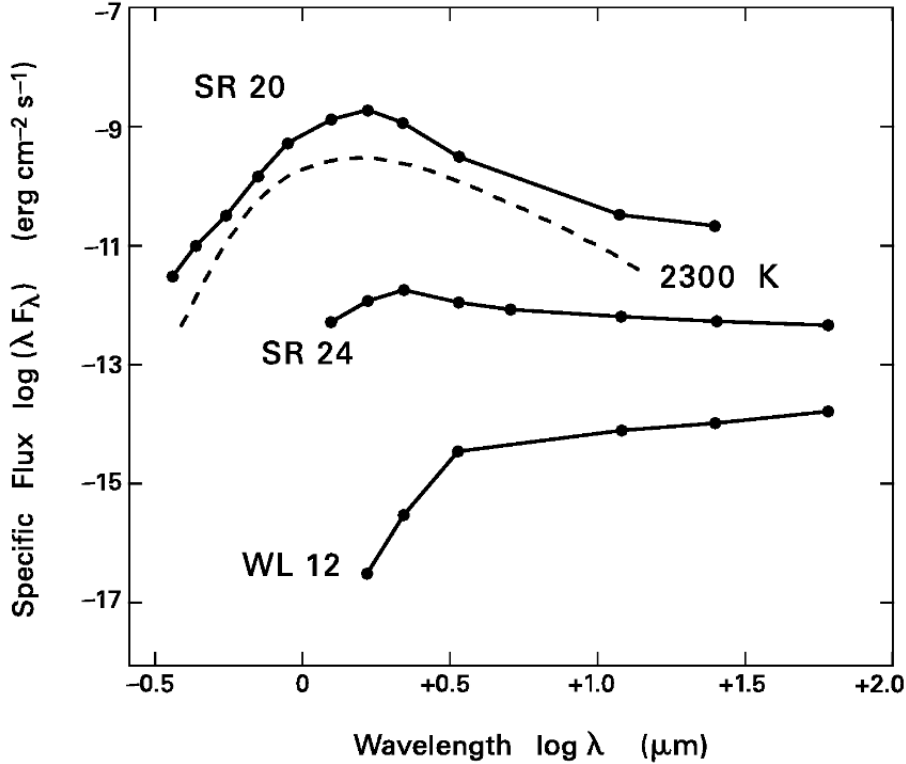


Figure 1.23: SEDs of three sources from ρ Ophiuchi dark cloud complex region (Stahler & Palla 2008). These three sources are example for class I (WL12), class II (SR 24) and class III (SR 20). The dashed curve shows the blackbody distribution ($T_{eff} = 2300$ K).

The de-reddened spectral energy distribution for star WL 12 shows a strong infrared excess, in vertical scale λF_λ , a main sequence or late-type star normally peak at 1 micron but in case of WL 12, it still increases to 60 micron. However, for sub-millimeter (and longer wavelengths) the flux eventually does decrease. Whereas in case of star SR 24, the plot shows relatively shallow slope in the mid and far-infrared spectrum, however for SR 20 it goes even steeply shows beginning to resemble a blackbody curve.

Infrared emission from WL 12 and SR 24 stems from heated dust grains. The typical infrared excess does not follow blackbody spectrum which implies that it can have large range of temperature. Moreover, these temperature are high enough that dust could be relatively closer to star and indicates that these dust particles could be a part of cloud material that is either participating in protostellar collapse or else it was leftover of collapse process.

It is empirically defined to measure the infrared excess as slope of SEDs to estimate the stellar youth. These slop is called *Infrared spectral index* and it is given by:

$$\alpha_{IR} \equiv \frac{d \log (\lambda F_\lambda)}{d \log \lambda} \quad (1.12)$$

Classification of YSOs are done by defining range of this slop (Adams et al. 1987; Robitaille et al. 2007). Objects like WL 12 with infrared excess having $\alpha_{IR} > 0$ are called *Class I objects*. These objects are generally associated with dense cores which are seen by NH_3 emission. The less embedded star, like SR 24 is called *Class II object*, which shows $-1.5 < \alpha_{IR} < 0$ as spectral index. Objects like SR 20 are classified as *Class III objects* having spectral index $\alpha_{IR} < -1.5$. There is also another class of object namely *Class 0 objects*, these are deeply embedded and can be detected only at far-infrared or millimeter wavelengths (Lada & Lada 2003). Fig. 1.24 shows example SED of one of such object L1448/mm lies in Bok globule in Perseus region. A short summery of YSO identification is given in Table 1.7.

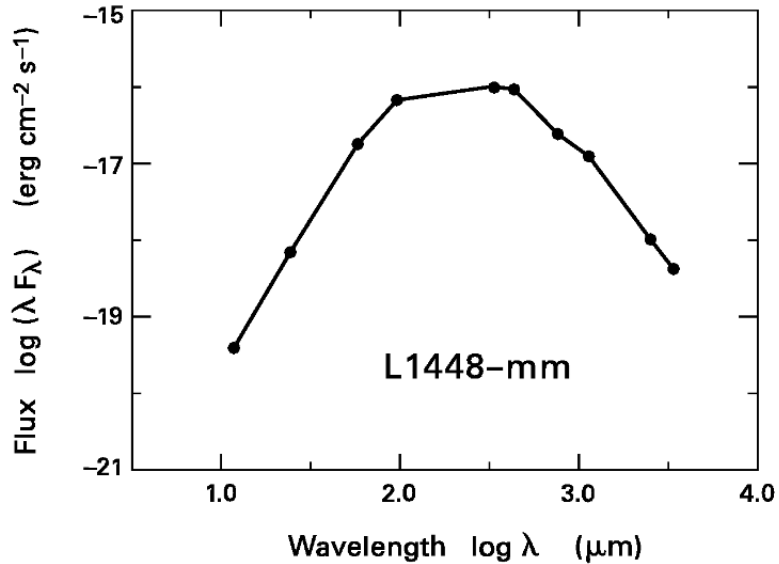


Figure 1.24: Example SED of class 0 object (L1448) (Stahler & Palla 2008).

Following is the brief discussion of three categories of young stellar objects:

- **Class 0 sources** ($\alpha_{IR} > 0$): Class 0 sources are embedded very deep and they are impossible to get observed even in near-infrared. Extended sub millimeter continuum emission shows the presence of spheroidal circumstellar dust envelope and peak comes in sub-millimeter wavelengths. In addition to this, they have also observed

Table 1.7: YSO classification

S. No.	YSO class	NIR spectral index	Comments
1	Class 0	$\alpha > 0$	Deeply embedded, Rising SEDs, sources with strong, spherical envelopes
2	Class 1	$\alpha > 0$	Rising SEDs, sources with strong spherical envelopes
3	Class 2	$-2 < \alpha < 0$	Pre-Main Sequence star with optically thick accretion disk
4	Class 3	$-3 < \alpha < -2$	Little or no disk left

high ratio between sub-millimeter luminosity to bolometric luminosity which suggest that envelope mass must have exceeded the central stellar mass. It also shows bipolar CO outflows (Bally et al. 1999).

- **Class I sources** ($\alpha_{IR} > 0$): These are the sources whose SED fits the models of mass accreting YSOs from circumstellar disk. These are completely obscured in visible spectrum that implies that the sources must be deeply embedded. The strong NIR excess is the result of the emission from the accreting circumstellar disk. They are often associated with the molecular outflows.
- **Class II sources** ($-2 < \alpha_{IR} < 0$): These are the evolved version of class I objects in which the surrounding envelope is pushed away by strong stellar winds or may be molecular outflows. Unlike the class I sources, these are visible in optical wavelengths. This phase of evolution is popularly known as classical T-Tauri phase (CTTs). SEDs of such sources can be fitted by a photo-sphere with circumambient disk. These sources often have molecular outflows.
- **Class III sources** ($-3 < \alpha_{IR} < -2$): This phase of evolution includes sources known as Weak line T-Tauri (WTTs). In these sources the circumstellar disk is partially or completely accreted (or dispersed by stellar winds and molecular outflows). SEDs of such sources very much resembles a stellar blackbody and can be modelled by a simple blackbody source with interstellar medium in between. They might show a little (or none) excess in NIR spectrum because of the cold dust particles presence. Fig. 1.25 shows an illustration of SEDs of different stages of young stellar objects. Along with these, the age and schematic representation of YSOs is also shown.

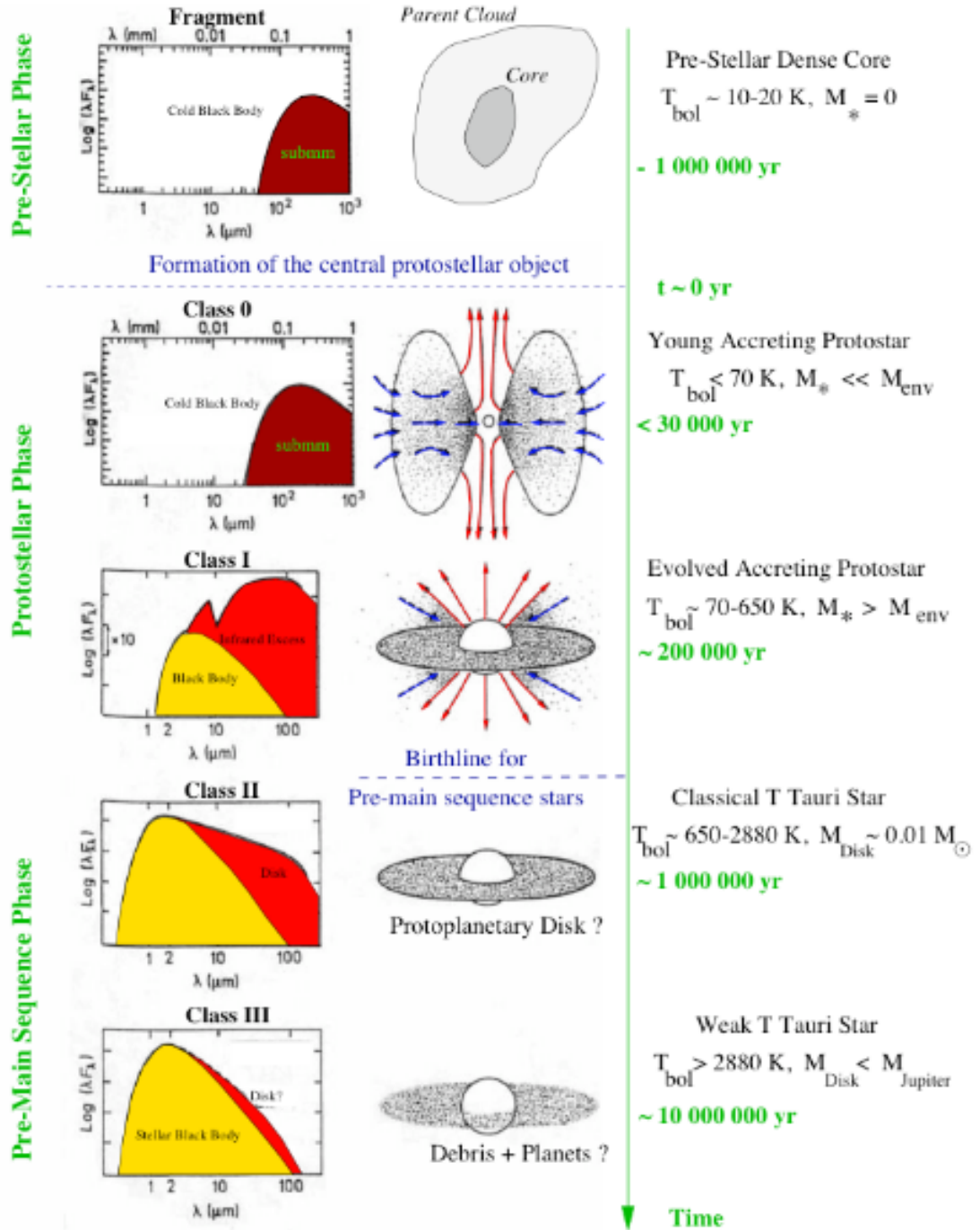


Figure 1.25: Evolution of low mass stars and their SEDs (Wilking 1989). Left hand side shows the SEDs of the different classes of YSOs, the combined effect of intrinsic blackbody and infrared excess/disk. Right side shows schematic evolution of star from parent clouds (core) to weak line T-Tauri star.

1.7 Motivation and Region of Study

This project involves study of such BRCs in different H II complexes like W3, W4 and W5. In the beginning of project, we have started with studying W5E H II region which includes two BRCs, BRC13 and BRC14 (see Fig. 1.26 and Fig. 1.27). This H II region is located in the Perseus arm of the Galaxy. The region is ionized by star cluster HD 18326. The cluster center turned out to be at $\alpha_{2000} = 02^h 59^m 22.0^s$; $\delta_{2000} = 60^\circ 34' 37''$. Distance of this region is close to 2.372 ± 0.231 Kpc. The spectral type of ionizing cluster members are B0 or earlier.

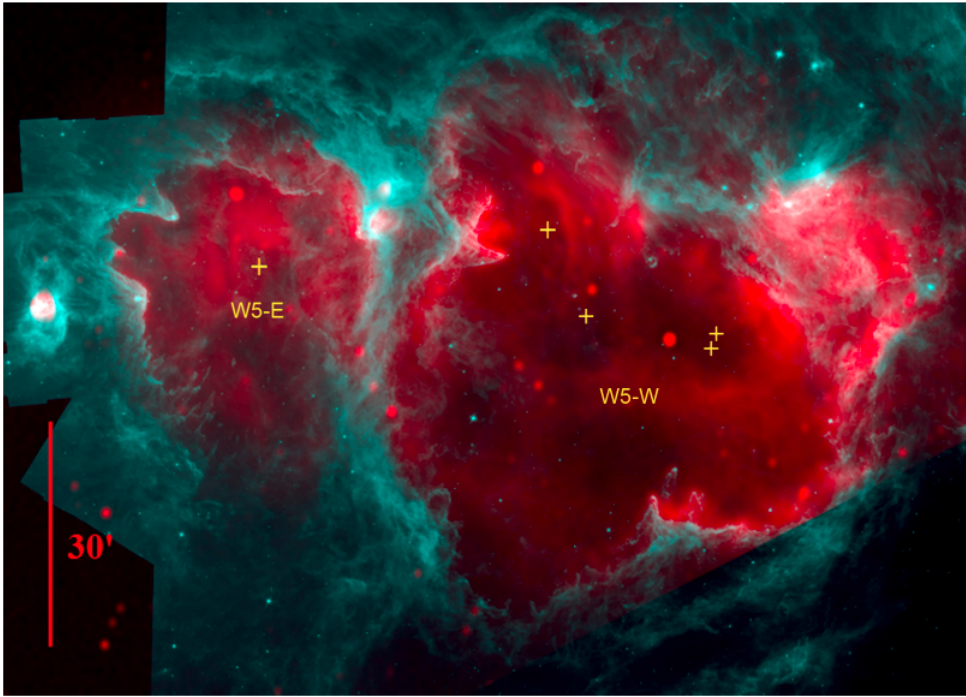


Figure 1.26: Region of giant molecular complex W5. Color composite image shows two HII regions, W5E and W5W in radio 1.42 GHz (red), Spitzer IRAC 8.0 μ m (cyan). The yellow plus sign shows the position of ionizing source (Deharveng et al. 2012).

The data analysis on two BRCs involves multi-wavelength photometric study followed by analysis of spectral energy distribution. For multi-wavelength study we are considering Near Infrared data from NEWFIRM and 2 Micron all sky survey (2MASS), for Mid-Infrared study, Spitzers data will be analyzed. For optical window, Pan-Starrs data will be used. Using Image Reduction and Analysis Facility (IRAF), we have carried out, first, the aperture photometry in all 7 bands (three for NEWFIRM and four for Spitzer), and then using that result we have modelled the point spread function (PSF) in order to do PSF

photometry.

All the results from different photometric bands were matched to prepare a complete catalog. The source matching was done using a python based code, which uses the concept of finding the counterpart using least distance method. The results of all the photometry were cataloged along with the photometric data available from the DS1 survey of PAN-STARR. In order to calibrate the catalog, two other standard catalogued were used. In case of NIR calibration, we have used 2MASS point source catalog, and for MIR calibration we have used catalog from Koenig et al. (2008).

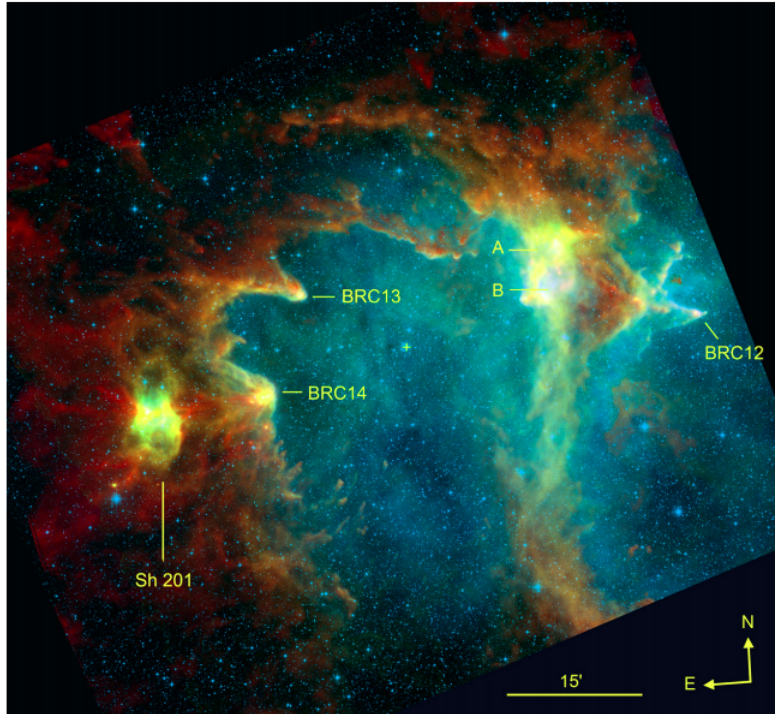


Figure 1.27: Color-composite image of W5E HII region with $250 \mu\text{m}$ Herschel-SPIRE (red), $250 \mu\text{m}$ Herschel-PACS (green), DSS2 survey (blue). The yellow cross shows HD18326 which is an ionizing star cluster for W5E HII region (Deharveng et al. 2012).

Later using all these, the project involves the study of star formation rate, star formation efficiency in all possible complexes W3, W4 and W5. This project also involves the looking at the star formation at the luminosity level of brown dwarf. This project will also investigate to look at the initial mass function at the lowest possible mass range, also to check whether the trend of IMF will be same as it goes towards higher mass ranges.

Chapter 2

Methodology and Data Analysis

2.1 Instruments

This project involves the photometric study in 12 filters, mainly in Optical, Near infrared and Mid infrared spectrum. In optical spectrum, this project utilizes the 3π -survey catalogue of Panoramic Survey Telescope and rapid response system 1 (Pan-Starrs 1) and used g, r, i, z and y band photometric data for SED fitting.

In Mid infrared spectrum, IRAC PBCD fits images have been used for photometric analysis, by doing PSF photometry, photometric data has been retrieved. Similarly for near infrared, NEWFIRMs images is used and PSF photometry is done to get J, H and K band data. Brief introduction to all these instruments is given in following sections.

2.1.1 NEWFIRM

Near Infrared Observation has been taken by NEWFIRM instrument on 2009-11-14. NEWFIRM, the NOAO Extremely Wide Field Infrared Imager, images a 28×28 arcmin 2 field of view on the NOAO 4-m telescopes. It covers a wavelength range of 1 - 2.4 microns at plate scale 0.4 arcsec/pixel. It was offered on the 4-m Mayall telescope on Kitt Peak through April, 2009. It is currently operating on the 4-m Blanco telescope on Cerro Tololo. The detector

Table 2.1: Mean Wavelength and Bandwidth for all twelve filters used for this project

Filter	λ_{mean} (Å)	λ_{min} (Å)	λ_{max} (Å)
NEWFIRM (NOAO)			
J	12511.50	11393.00	13612.00
H	16319.10	14575.00	18105.00
K	21451.70	19462.00	23480.00
Spitzer IRAC			
CH 1	35572.60	31296.00	39614.00
CH 2	45049.30	39173.00	50561.00
CH 3	57385.70	48983.00	65089.00
CH 4	79273.70	62994.00	95876.00
Pan-STARR (PS1)			
g	4900.10	3943.00	5593.00
r	6241.30	5386.00	7036.00
i	7563.80	6778.00	8304.00
z	8690.10	8028.00	9346.00
y	9644.60	9100.00	10838.00

focal plane consists of four 2048 x 2048 arrays arranged in a 2 x 2 mosaic. We have used three images, J filter (1.3 micron with bandwidth 1048.4 nm, FWHM 160.6 nm), H filter (1.5 micron with bandwidth 1555.7 nm, FWHM 174.7 nm) and K filter (2.2 micron with bandwidth 2165 nm, FWHM 257nm) for our study. The filter profile is shown in fig. 2.1.

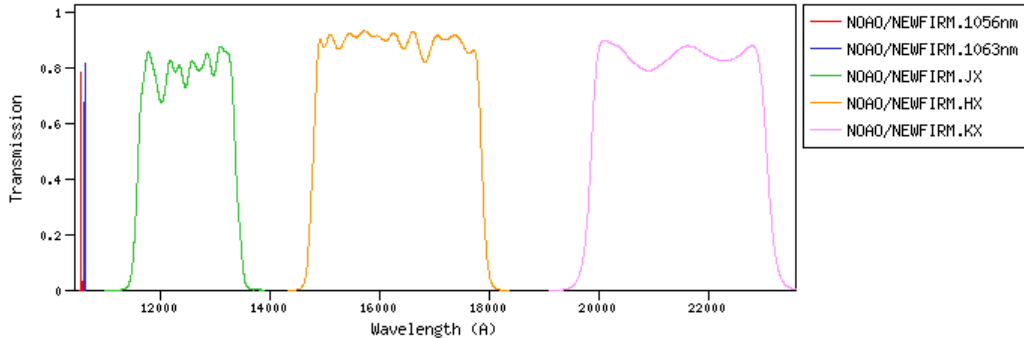


Figure 2.1: NEWFIRM filter profile

2.1.2 Spitzer IRAC

Mid infrared observations has been taken from the Spitzer archive observed by infrared array camera (IRAC) (PI: Fazio, Giovanni, program id 201, AOR Key:6610688), observation dated 2004-01-18. The observations were taken during the Spitzer cryogenic mission. This observations are available in all four IRAC bands. Details of these bands are shown in Fig. 2.2 along with filter profiles. This project utilizes Post-Basic Calibrated Data (PBCD) product of Spitzer centers IRAC pipeline, they have been already processed as mosaics with dithering scale ‘medium’ and dither N-position equals to 3. These observations came with frame time of 12 sec for each channel. They have a plate scale of 0.6 arcsec/pix.

2.1.3 Panoramic Survey Telescope and rapid Response System I (Pan-STARR I)

Panoramic Survey Telescope and rapid Response System (Pan-STARRS) is system of wide astronomical imaging situated at Hawaii on a 1.8 meter telescope with 1.4 Gigapixel camera (GPC1). This image the sky in five broadband filters (g,r,i,z,y). Pan-STARR 1 is the first data release. The field of view of Pan-STARR 1 is 3 degrees in diameter and 7 square degrees FOV towards 30 degrees north of declination. This has 60 orthogonal transfer arrays. This survey has been done in two parts, 3π steradian survey and medium deep survey.

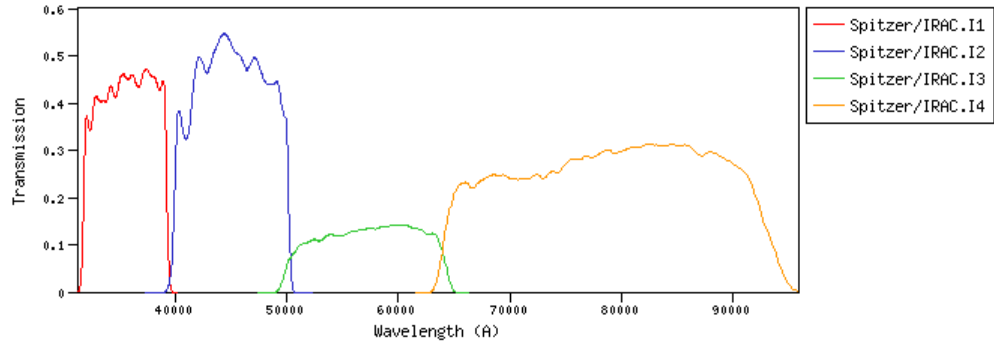


Figure 2.2: Spitzer IRAC filter profile

The filter profile for all five filters is shown in Fig. 2.3. Unlike the Spitzer and NEWFIRM spectrum, this project do not involve direct PSF photometry, but we have used the catalog values from the archive.

The 5σ depth in magnitude scale for all five filters along with seeing is shown in Table 2.2. This project also involve values utilization of data in g band below 20.0, since the uncertainty towards the edge of the depth is high, hence they have been ignored. All the point sources included by the catalog were matched by procedure given in 2.3.4.

Table 2.2: Pan-STARR PS1 5σ depth and seeing

Pan-STARR Filters	5σ depth (mag)	Median Seeing (arcsec)
g	23.30	1.31
r	23.20	1.19
i	23.10	1.11
z	22.30	1.07
y	21.30	1.02

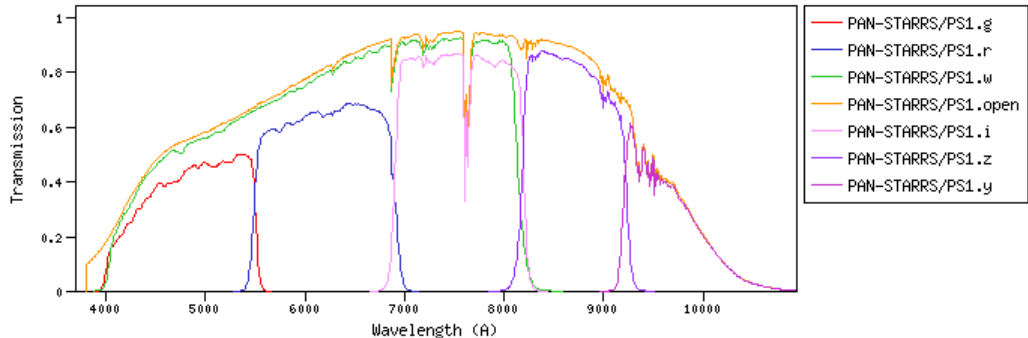


Figure 2.3: Pan-STARR filter profile

2.2 Photometry

The word ‘Photometry’ originated from Greek *photo* and *metry* which is a technique used by astronomers deals with measuring the photon flux (or intensity) radiated by astronomical objects. In this section we will introduce some of the basic concepts of photometry and then a few advance approaches like point spread function modelling methods. After that, using techniques discussed in this section, we will proceed to next section 2.3.2 which use these to make data reduction. First lets talk about the basic method of photometry, the Aperture photometry below;

2.2.1 Aperture Photometry

The basic principle of aperture photometry is to add up the flux observed inside a given radius also called as ‘Aperture’ from the center of an astronomical object. Leading to this, subtracting the sky background within the same area where the object lies on sky and measuring only the flux from the astronomical object. Aperture radius is a tricky parameter. As we know that seeing, focusing errors, tracking, mount errors etc. may bias the amount of flux within the aperture radii. This leads to one more issue, as noise grows proportional with aperture radius as the source flux blends up towards the edge of the profile. Figure 2.4 shows the aperture radii, inner and outer radii to measure the source flux and background flux respectively.

As we increase the aperture radii, it increases the poisson shot noise of the background sky. The S/N ratio of the flux approaches a maxima at a moderatae aperture radius (Howell 1989). Using a smaller radius brings the issue that the fraction of the total flux will different for objects of different flux. In this case, aperture corrections are used. Image Reduction and Analysis Facility (IRAF) provides following tasks to perform aperture photometry;

1. *imexamine* - single aperture photometry (defind at ‘rimexam’) using the image display software ds9.
2. *phot* - User interactive or batch mode multi-aperture photometry for a several point sources with several more parameters to tune.

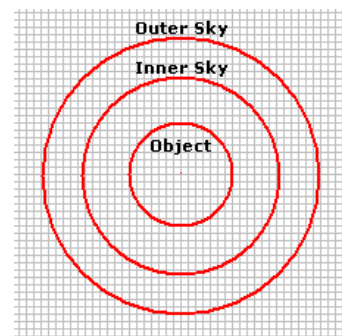


Figure 2.4: Point source photometry showing the aperture radius with the inner and out sky radius to measure background sky value.

3. *qphot* - User interactive or batch mode multi-aperture photometry for several point sources with a minimal parameter to tune.
4. *polyphot* - User interactive or batch mode single aperture photometry for several of polygon-like sky regions.
5. *wphot* - User interactive or batch mode multi-aperture photometry for several of point sources with weighting available.

In order to calculate the magnitude of point source, following are the quantities measured by IRAF for photometric operation (Davis et al. 1994).

$$Flux = Sum - (area \times msky) \quad (2.1)$$

$$Magnitude = Zmag - 2.5 \log_{10}(Flux) + 2.5 \log_{10}(itime) \quad (2.2)$$

$$err = \left(\frac{\left[\frac{Flux}{epadu \times Rdnoise} + (area \times stdev^2) + (area \times stdev)^2 \right]}{nsky} \right)^{1/2} \quad (2.3)$$

$$merr = 1.0857 \times \frac{error}{Flux} \quad (2.4)$$

Where itime: integration time, Flux: Total flux inside aperture excluding sky value, Sum: Total counts including sky value in aperture, area = Aperture area, msky: Mean sky value, Zmag: Zero-point magnitude, itime: Exposure time (Sec), epadu: CCD Gain in adu, Rdnoise: CCD Read Noise, stdev: Standard deviation of background, nsky: Number of sky pixels

Growth of curve is a plot which shows the trend of aperture radii with magnitude measured. The plot is generated after doing the ‘phot’ operation for a 2MASS field. This shows the trend that magnitude value decreases (i.e. flux value inside the aperture radii increases) as the aperture radii increases. This growth of curve is shown in fig. 2.5. Other than this, if we see the trend between the magnitude value and magnitude error (merr), keeping the aperture radii fixed, this trend shows that the magnitude error increases for fainter sources as shown in fig. 2.6.

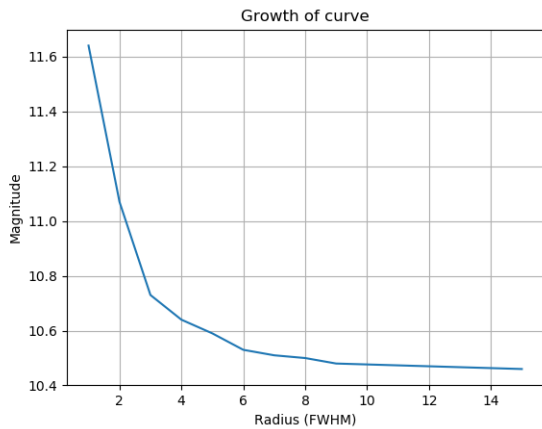


Figure 2.5: Growth of curve showing the trend between magnitude value and aperture radii. Photometry is done on a 2MASS field using ‘phot’ task.

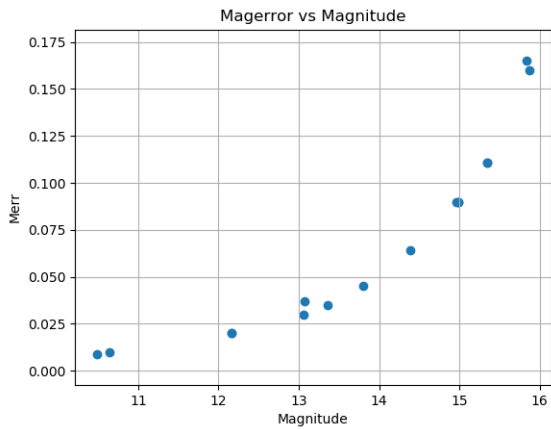


Figure 2.6: Magnitude vs Magnitude error for a 2MASS field. Photometry is done by IRAF ‘phot’ task keeping the aperture radii fixed.

2.2.2 Point spread function (PSF) Photometry

The motivation behind PSF model fitting method is crowded field photometry, where point sources are blended with the neighbourhood and any possible size of aperture radius could include more than one point source. DAOphot was first developed by Dr. Peter Stetson for precise ground-based photometry for the crowded fields in case of globular clusters. After that, it has since been included into IRAF as the PSF model fitting package.

The PSF profiles of point sources from the ground found to have an approximately Gaussian core. These profiles have large wings decreasing because inverse square law. This method can remove the variations due to seeing and enabling larger effective radii to be used. Following are the main tasks involved in PSF photometry;

1. *daofind* - search point sources in an FITS image using the DAOFIND algorithm.
2. *phot* - This compute initial magnitudes for a list of stars, it is simply a aperture photometry with one or more than one aperture radius, the results from this photometry is used to model the PSF. In place of ‘phot’ any other aperture photometry tasks can be used mentioned in section 2.2.1.
3. *psf* - Estimates the point spread function for the list of point sources.
4. *peak* - This fits the PSF model to single point source.

5. *nstar* - This modelles the PSF model for groups of point sources defind earlier by user.
6. *allstar* - This task groups and fits the PSF model to multiple point source simultaneously.
7. *substar* - This subtracts the fitted point source from the FITS image.

Followg is the summery of PSF photometry including all the steps and tasks to perform modelling and estimating photometric results out of this;

- In order to prepare list of all the point sources above the threshold of user defind background (usually $3-5\sigma$), task *daofind* is used which convolves Gaussian kernel to all pixel. By doing this, it makes decision to consider source to be point sources like stars or extended sources like galaxies or defects like cosmic rays. In order to do this operation, two pset parameter files are important to configure, *datapars* and *findpars*. It is important to fix parameters like ‘datamin’, ‘datamax’, ‘readnoise’, ‘epadu’ etc. before doing the *daofind* task. These all parameters can be found at the header of the image.
- Doing the aperture photometry all the identified point sources from *daofind*. Before doing this task, it is important to fix another set of parameters. There are three pset parameter files, *photpars*, *centerpars* and *fitskypars*. *photpars* mainly handles parameters related to setting aperture radii. Parameter file *centerpars* fix parameters like ‘calgorithm’ and ‘CBOX’ which are important to initiate the aperture photometry. Similerly *fitskypars* sets parameters which are important to estimate the background. This sets parameters like ‘annulus’ and ‘dannulus’.
- To begin the PSF modelling, identify the point source close to the edge of FITS image or too faint and remove them from list. Consider only bright, isolated stars spread across the FITS frame. This is done by tasks like *psselect*, this fixes the parameters like ‘maxnpsf’ (the number of PSF point sources to be modelled) or ‘interac’ (the process can be done manually or interactively).
- In order to build a semi-empirical PSF model, all the PSF point sources identified from previous steps. The analytic functions used to model the PSF are chosen from bivariate Gaussian, Moffat or Lorentz functions. This requires a iterative process to produce a ‘clean’ PSF in some cases, whereby PSF modelling and fitting is performed. Faint neighbors point sources of PSF point sources are identified and are

subtracted, fitted. In order to model the PSF, first *daopars* parameter file has to be set. This includes choice of analytic function to be modelled (e.g. auto, gaussian, moffat, lorentz etc) by setting ‘function’ parameter. The other two most important parameters here are ‘psfrad’ and ‘fitrad’.

1. *psfrad*: This defines the radius of circle within which the PSF model is set. It can be 1-2 pixel greater than 2-3 times FWHM of the bright star in FITS image. This should never set more than size of PSF model. But this can be set smaller in task *ALLSTAR*.
2. *fitrad*: This parameter defines fitting radius in scale unit. Only pixel fall within this radius from the center of point source will add to the fits by *ALLSTAR*. This has to be equal to the average FWHM of the list of PSF point sources.

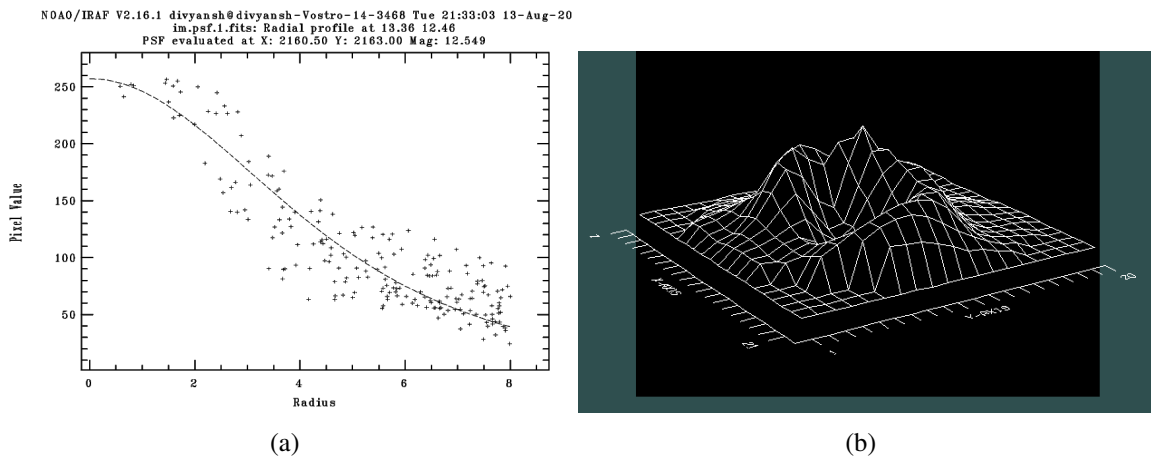


Figure 2.7: Example of PSF model fitted using analytic function MOFFAT on linear scale (a) and on two dimensional plane (b).

The psf model is shown in fig. 2.7.

- Using the centroid of a point source as the profile center and sky background as determined for aperture photometry in step 2, the PSF model is shifted and scaled to fit the observed stellar FITS image by non-linear least-squares. The scaling estimates the magnitude values.

This process of photometry including aperture and PSF photometry is illustrated in fig. 2.8 as a flowchart.

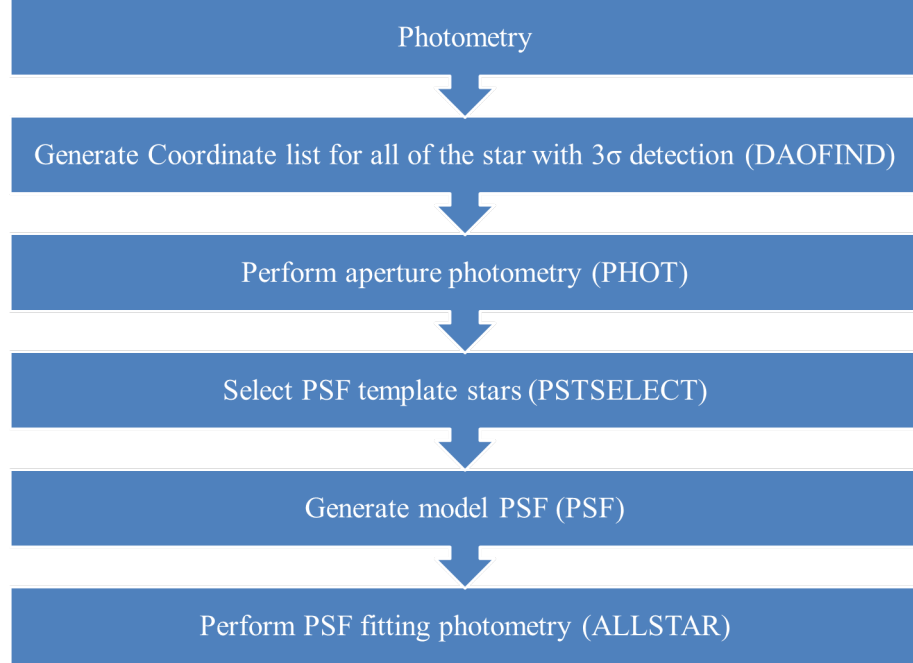


Figure 2.8: PSF photometry Flowchart

2.3 Near Infrared Data Reduction

2.3.1 NIR Source Detection

To identify the sources in all three bands, automated source identification algorithm is considered. To do that, we have used IRAF v2.16 APPHOT package with DAOFIND task. The average full width at half maximum (FWHM) of point spread function (PSF) was estimated by plotting 30 bright unsaturated point source's radial PSF plot and then averaging it. To estimate the background, more than 10 regions sized about the average PSF were selected such that no bright sources should fall close to them. The standard deviation of the pixel value enclosed in that region is taken as sigma. The background is taken as 3σ to identify as a valid point source.

Table 2.3: Parameter used for source detection

Parameter	Value
Scale	1.00
FWHMPSF	2.20
DATAMIN	INDEF
DATAMAX	INDEF
NOISE	Poisson
SIGMA	0.70
THRESHOLD	3.00

Total number of sources that we detected by this task are 31835 in K-band image. Some important parameters for this task are given in table 2.3. Rest of the parameters are set to default (Wells 1994).

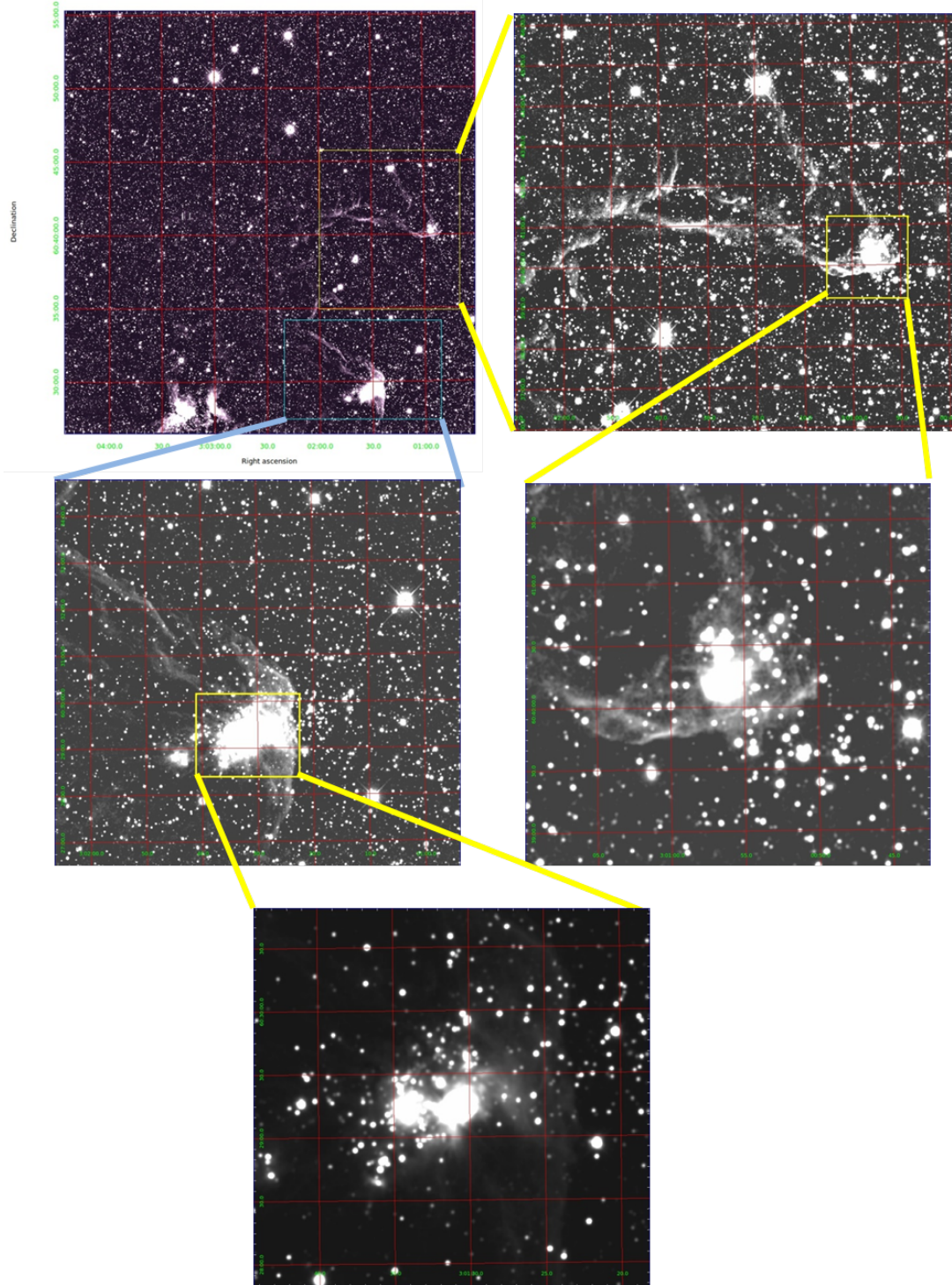


Figure 2.9: K-Band NEWFIRM FITS image. In top left panel, yellow box is showing BRC 13 and magenta box is showing BRC 14

2.3.2 NIR Aperture Photometry

The aperture photometry is done by using IRAFs AP-PHOT package and PHOT task for all three filters. In aperture photometry, a point source is marked by an aperture of few time of its FWHM (usually 2-3 times of FWHM). After that an annulus is marked over the source to estimate the background value which is further subtracted from apertures value. Using this method, the magnitude and its uncertainty is calculated. Since there are many crowded regions in the field of view, hence the results of aperture photometry are insufficient for our study. We have done PSF photometry for all three filters using the results of aperture photometry as initial values for tasks like psf and allstar. Table 2.4 includes main parameters used in aperture photometry. Rest of the parameters are set to default values.

Table 2.4: Parameters used in Aperture Photometry (PHOT)

Paramters	Value
CALGORITHM	Centroid
CBOXWIDTH	4.00
SALGORITHM	Centroid
CMAXITR	10.00
ANNULUS	10.00
DAANUSLU	5.00
BINSIZE	0.10
APERTURES	2:10:1
Zero-point Magnitude (mag)	J: 22.40 H: 22.57 K: 21.66

2.3.3 NIR PSF Photometry

When doing photometry on crowded star fields, such as globular clusters or open clusters, aperture photometry will not yield reliable results. PSF photometry involves modelling the point spread function (PSF) by using appropriate number of bright stars. This modelled PSF is then fitted with different available functions. As an initial guess of magnitude value, the result of aperture photometry result is used. Fig. 2.8 shows the flow chart for doing entire photometry procedure. Output of PSF is the model PSF file which fits the model PSF to all stars in field. Fitting result for J filter shown here with some important parameters is given in table 2.5.

Performing ALLSTAR results in rejection of some stars which do not fits the model psf well enough. That's why we get different number of photometric result in all three filters. Out of 31835 point sources identified using DAOFLIND, 29766 point sources converged after ALLSTAR in K filter. Similarly 29048 point sources

Table 2.5: Parameters used for PSF and ALLSTAR

Parameters	Value
FITRAD	4.00
PSFMAG (J)	12.50
RECENTER	YES
FITSKY	YES
GRPSKY	YES
ANNULUS	10.00
DANNULUS	5.00
MAXGROUP	60.00
INTERAC	YES

for J filter and 29261 point sources for H filter get converged. Fig. 2.10 shows magnitude v/s merr plot for all three filters. These plots include only those sources which are common in all three filters result. Following is the fitting result for J band, here ‘auto’ mode is chosen, the best fit occurs with ‘moffat15’ (Davis et al. 1994).

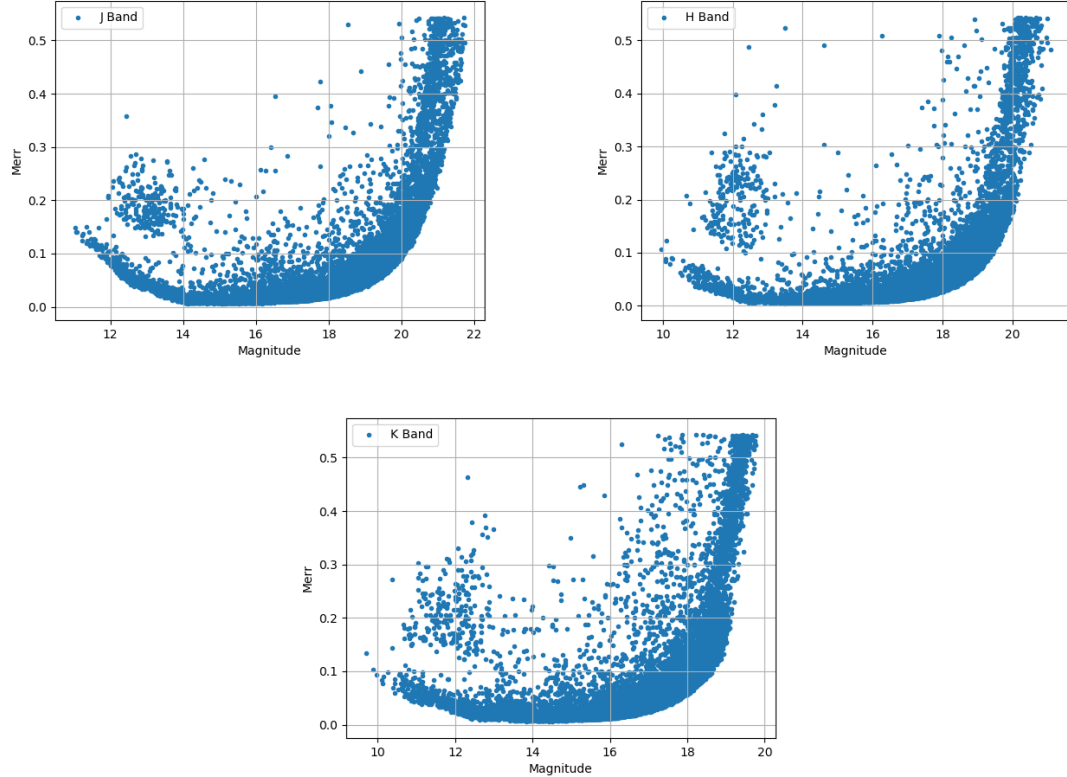


Figure 2.10: Magnitude v/s Error Plots for NEWFIRM JHK images

FITTING PARAMETRS:

MODE: AUTO

56 PSF STARS READ FROM IM.PST

TRYING FUNCTION GAUSS NORM SCATTER = 0.04098054

TRYING FUNCTION LORENTZ NORM SCATTER = 0.03926116

TRYING FUNCTION MOFFAT15 NORM SCATTER = 0.0310756

TRYING FUNCTION MOFFAT25 NORM SCATTER = 0.02764714

TRYING FUNCTION PENNY1 NORM SCATTER = 0.02984296

TRYING FUNCTION PENNY2 NORM SCATTER = 0.02979425

BEST FITTING FUNCTION IS MOFFAT25 ANALYTIC PSF FIT

**FUNCTION: MOFFAT25 X: 2160. Y: 2162. HEIGHT: 608.4891 PSFMAG: 12.504
 PAR1: 0.9208277 PAR2: 0.8829506 XYTERM: -0. 03165133 MOFFAT: 2.5**

2.3.4 NIR Source Matching

Since the number of point sources in all three filter photometry are different, so it is important to identify the counterpart of every point source in other filter's result. To do this astropy package is used and a python script has been prepared. Concept behind source counterpart identification is to find the distance of every point source with all the point sources in other filter. The criterion for point source to be identified as the counterpart is that if the distance turns out to be the size of one pixel length or accuracy is comparable with the seeing of the observation. After doing this, a raw NEWFIRM catalog is prepared which includes more than >28500 point sources photometric data in JHK band.

2.3.5 Calibration and Catalog merger

2.3.5.1 Calibration of raw NEWFIRM catalog

Our raw NEWFIRM catalog is calibrated by 2MASS photometric data. Online available photometric data of 2MASS for the same field of view (30 arcmin cone) with error constraint ($\text{merr} < 0.1$) and magnitude constraint ($13 < \text{mag} < 15$) is fetched. The magnitude constraints are given because in NEWFIRM image, point sources brighter than about 11-12 mag are close to saturation or saturated. Whereas in case of 2MASS survey, as the magnitude of point source approaches to values faint as 18 mag, the error in observation rapidly increases. To do the calibration, magnitude range of 13-15 mag from both the catalog are used to plot the distribution of difference in magnitude for all filters.

This is done after carefully identifying

Table 2.6: Offsets used for calibration

Filter	δMag (2MASS-NEWFIRM)	Standard Deviation σ
J	0.0591	0.098
H	-0.0964	0.079
K	-0.0331	0.086

the source counterpart in 2MASS catalog using the same approach discussed in section 2.3.4. The distribution histogram with 50 bins and its Gaussian best fit is shown in Fig. 2.11. The offset values in NEWFIRM catalog is calculated from Gaussian best fit. Mean values and Sigma values for all the distribution is shown in table 2.6. Also the similar distribution is plotted for all three colours (J-H), (H-K) and (J-K) and that is shown

in Fig. 2.12. Since the color offset tends to zero for all three filters, hence we have not given any color correction.

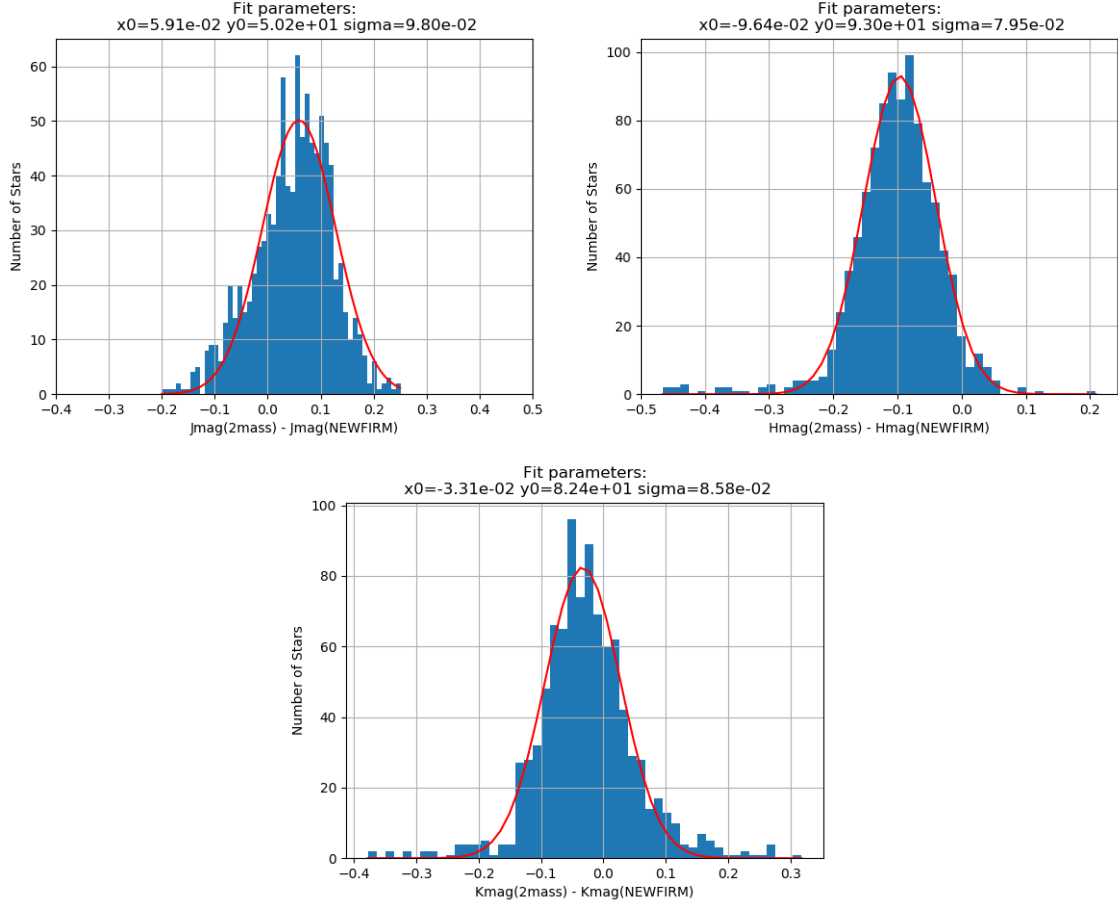


Figure 2.11: Distribution of magnitude difference between NEWFIRM and 2MASS

2.3.5.2 Catalog merger (2MASS and NEWFIRM)

Two telescopes used for observation by 2MASS and NEWFIRM are having 1m and 4m aperture. Because of that in case of 2MASS data, point sources bright enough (10 mag or less) are unsaturated and have very less photometric uncertainty. In contrast with this, for NEWFIRM, the point sources faint enough (17mag or more) shows good accuracy. Hence this study bounds to use mixture of data from both the observations. The cut-off/saturation limit set for the merger of two catalogs is 13 mag. Hence point sources brighter than 13 mag in NEWFIRM are discarded and point sources fainter than 13 mag in 2MASS are discarded. The rest of the point sources in both the catalog are merged to make a complete catalog. The Magnitude v/s merr plot for this new catalog is shown in Fig. 2.13.

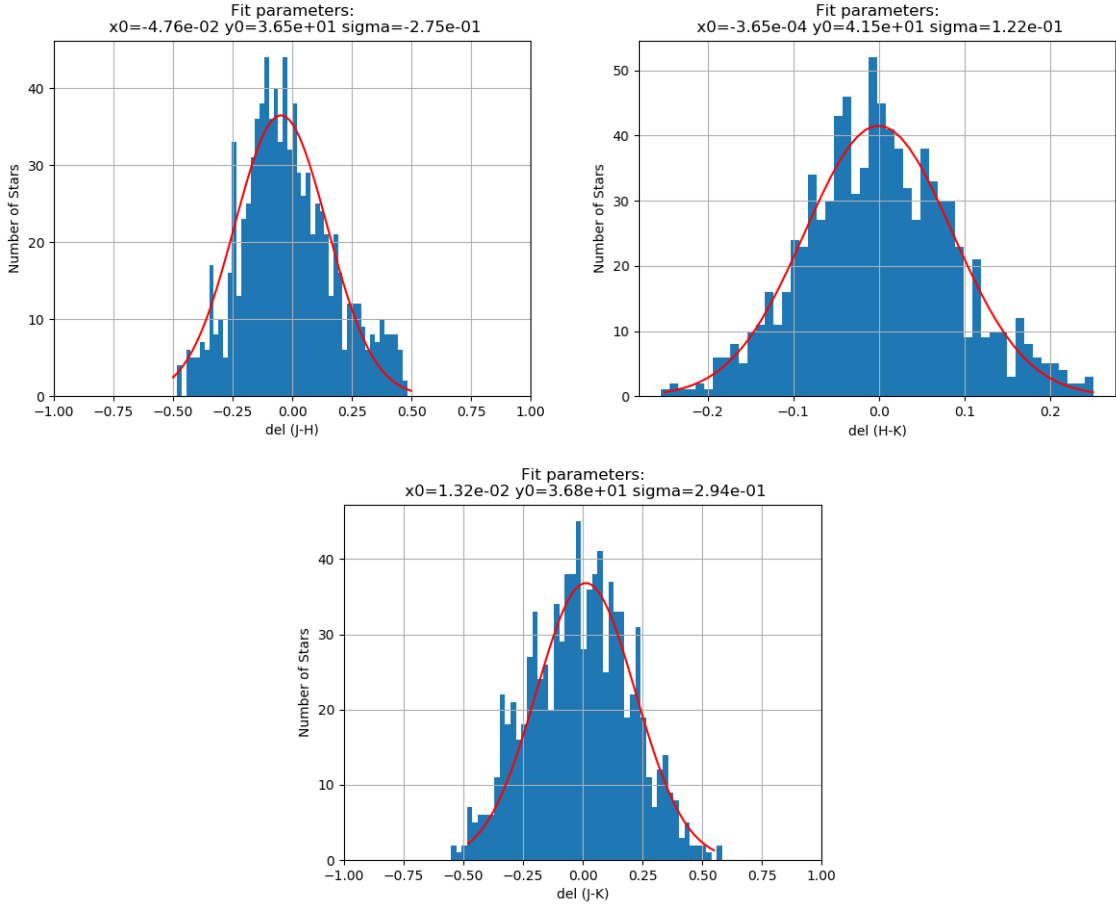


Figure 2.12: Distribution of color difference between NEWFIRM and 2MASS

2.4 Mid-Infrared Data Reduction

2.4.1 MIR Source Detection

To identify the sources in all four bands, automated source identification algorithm is considered. To do that, we have used IRAF v2.16 APPHOT package with DAOFLUX task. The average full width at half maximum (FWHM) of point spread function (PSF) was estimated by plotting 25 bright unsaturated star's radial PSF plot and then averaging it. Total number of sources that we detected by this task are 13443 in channel 1 image. Some important parameters for this task are given in table 2.7. Rest of the parameters are set to default.

Table 2.7: MIR: Parameter used for source detection

Parameter	Value
Scale	1.00
FWHMPSF	3.20
DATAMIN	INDEF
DATAMAX	INDEF
NOISE	Poisson
SIGMA	0.50
THRESHOLD	3.00

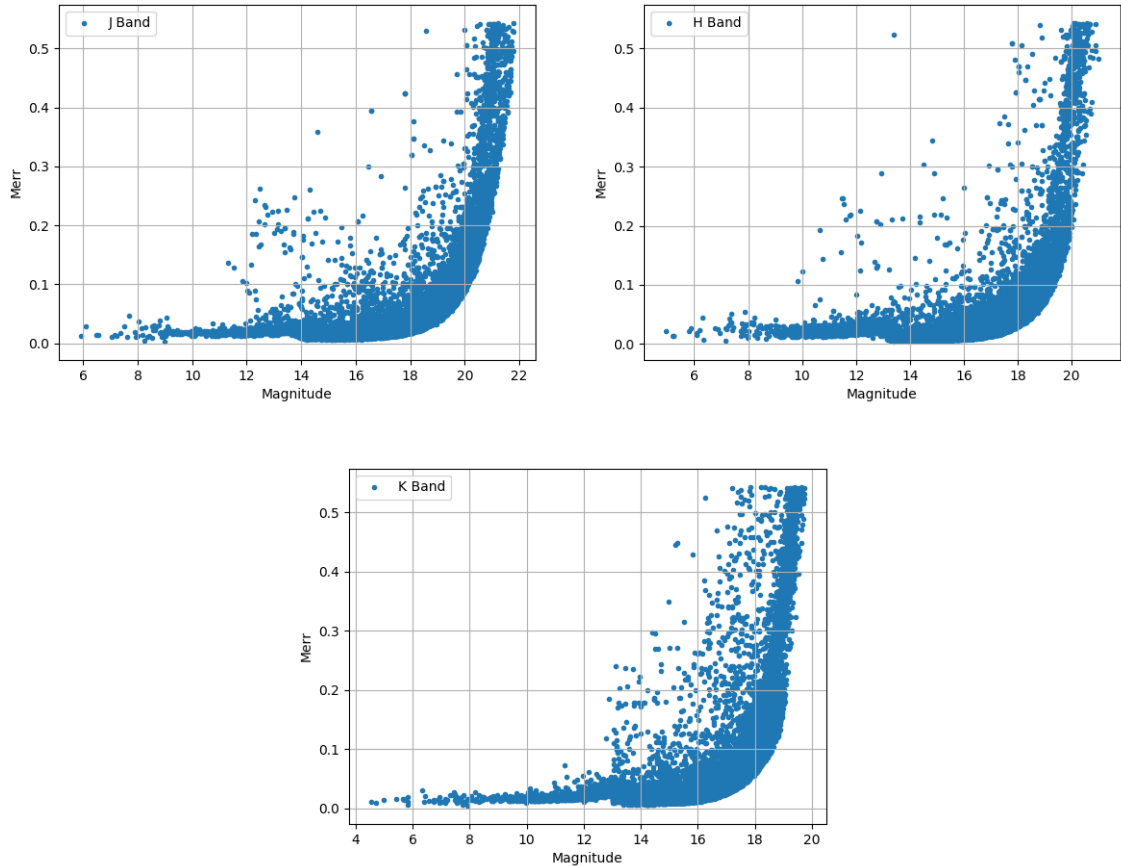


Figure 2.13: Magnitude v/s Error Plots for JHK filter from 2MASS and NEWFIRM

2.4.2 MIR Aperture Photometry

The aperture photometry is done by using IRAFs APPHOT package and PHOT task for all four filters. In aperture photometry, a point source is marked by an aperture of few time of its FWHM (usually 2-3 times of FWHM). After that an annulus is marked over the source to estimate the background value which is further subtracted from apertures value. Using this method, the magnitude and its uncertainty is calculated. Since there are many crowded regions in the field of view, hence the results of aperture photometry are insufficient for our study. We have done PSF photometry for all four filters using the results of aperture photometry as initial values for tasks like psf and allstar (see table 2.8).

Table 2.8: Parameters used in Aperture Photometry (PHOT)

Paramters	Value
CALGORITHM	Centroid
CBOXWIDTH	4.00
SALGORITHM	Centroid
CMAXITR	10.00
ANNULUS	10.00
DAANUSLU	5.00
BINSIZE	0.10
APERTURES	2:10:1
Zero-point Magnitude (mag)	CH1: 18.79 CH2: 18.32 CH3: 17.83 CH4: 17.20

2.4.3 MIR PSF Photometry

When doing photometry on crowded star fields, such as globular clusters or open clusters, aperture photometry will not yield reliable results. PSF photometry involves modelling the point spread function (PSF) by using appropriate number of bright stars. This modelled PSF is then fitted with different available functions. As an initial guess of magnitude value, the result of aperture photometry result is used. Output of PSF is the model PSF file which fits the model PSF to all stars in field. Fitting result for channel 1 is shown here with some important parameters is given in table 2.9. Performing ALLSTAR results in rejection of some stars which do not fits the model psf well enough. That's why we get different number of photometric result in all four filters. Out of 13443 point sources identified using DAOFLIND, 8244 point sources converged after ALLSTAR in channel 1. Similarly 5299 point sources for channel 2, 7088 in channel 3 and 4800 point sources for channel 4 get converged. Fig. 2.14 shows magnitude v/s merr plot for all four filters. These plots include only those sources which are common in all four filters result (Davis et al. 1994).

Table 2.9: Parameters used for PSF and ALLSTAR

Parameters	Value
FITRAD	4.00
PSFMAG (CH1)	14.11
RECENTER	YES
FITSKY	YES
GRPSKY	YES
ANNULUS	10.00
DANNULUS	5.00
MAXGROUP	60.00
INTERAC	YES

2.4.4 MIR Source Matching

Since the number of point sources in all three filter photometry are different, so it is important to identify the counterpart of every point source in other filter's result. To do this astropy package is used and a python script has been prepared. Concept behind source counterpart identification is to find the distance of every point source with all the point sources in other filter. The criterion for point source to be identified as the counterpart is that if the distance turns out to be the size of one pixel length or accuracy is comparable with the seeing of the observation. After doing this, a raw MIR catalog is prepared which includes more than 12700+ point sources photometric data in all IRAC bands.

2.4.5 Calibration and Catalog merger

Our raw MIR catalog is calibrated by GLIMPSE360 Catalog and catalog given by Koenig et al. photometric data Koenig et al. (2008). This is done after carefully identifying the source counterpart in both the catalog using the same approach discussed in section 2.3.4.

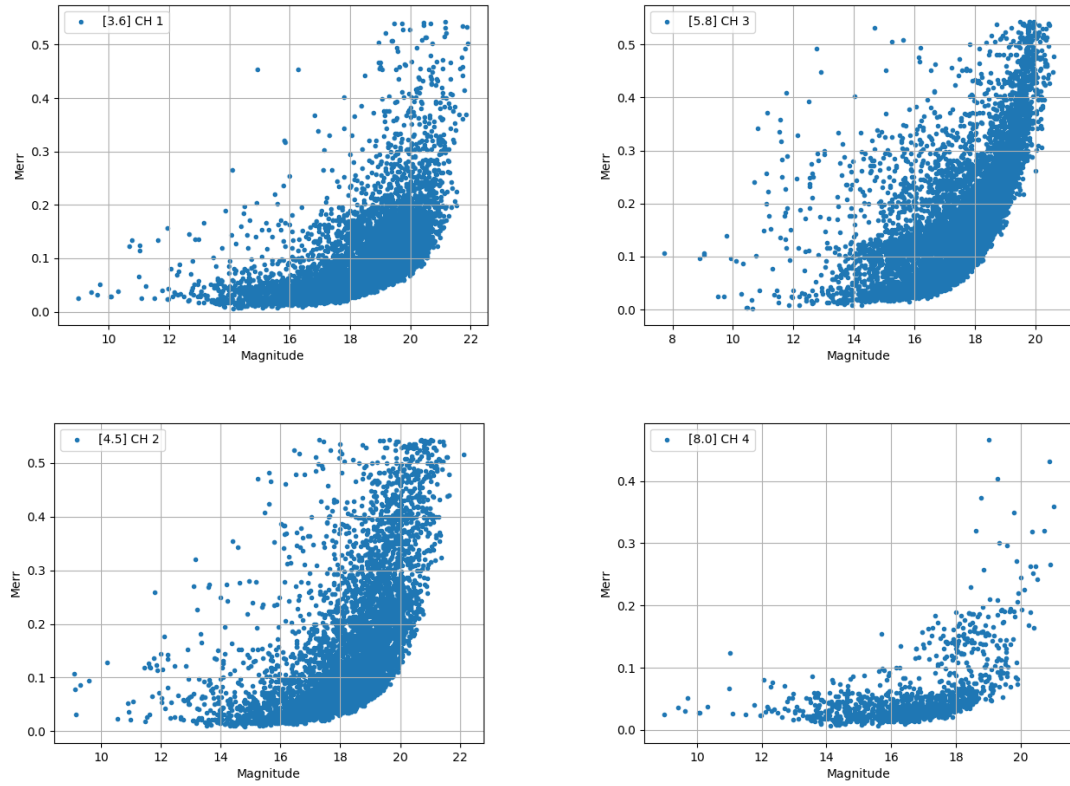


Figure 2.14: Magnitude v/s Error Plots for MIR IRAC images. Channel 1 (3.6 micron) (top left), Channel 2 (4.5 micron) (top right), Channel 3 (5.8 micron) (bottom left) and Channel 4 (8.0 micron) (bottom right).

Channel 3 and 4 data is not covered by GLIMPSE 360 catalog for the region, hence it is used only to calibrate channel 1 and 2. Catalog by Koenig et al. 2008 has sources in all bands, hence it is used to calibrate all four bands. The distribution histogram with 50 bins and its Gaussian best fit is shown in fig. 2.15.

Table 2.10: Offsets used for calibration

Filter	δMag ($Mag_{psf} - Mag_{koenig}$)	Standard Deviation σ
CH1	3.28	0.292
CH2	3.03	0.309
CH3	3.19	0.094
CH4	4.54	0.145

The offset values in MIR catalog is calculated from Gaussian best fit. Mean values and Sigma values for all the distribution is shown in table 2.10. Sample catalog after matching NEWFIRM, Spitzer and Pan-STARR data by same procedure adopted in section 2.3.4 is given in table 2.11.

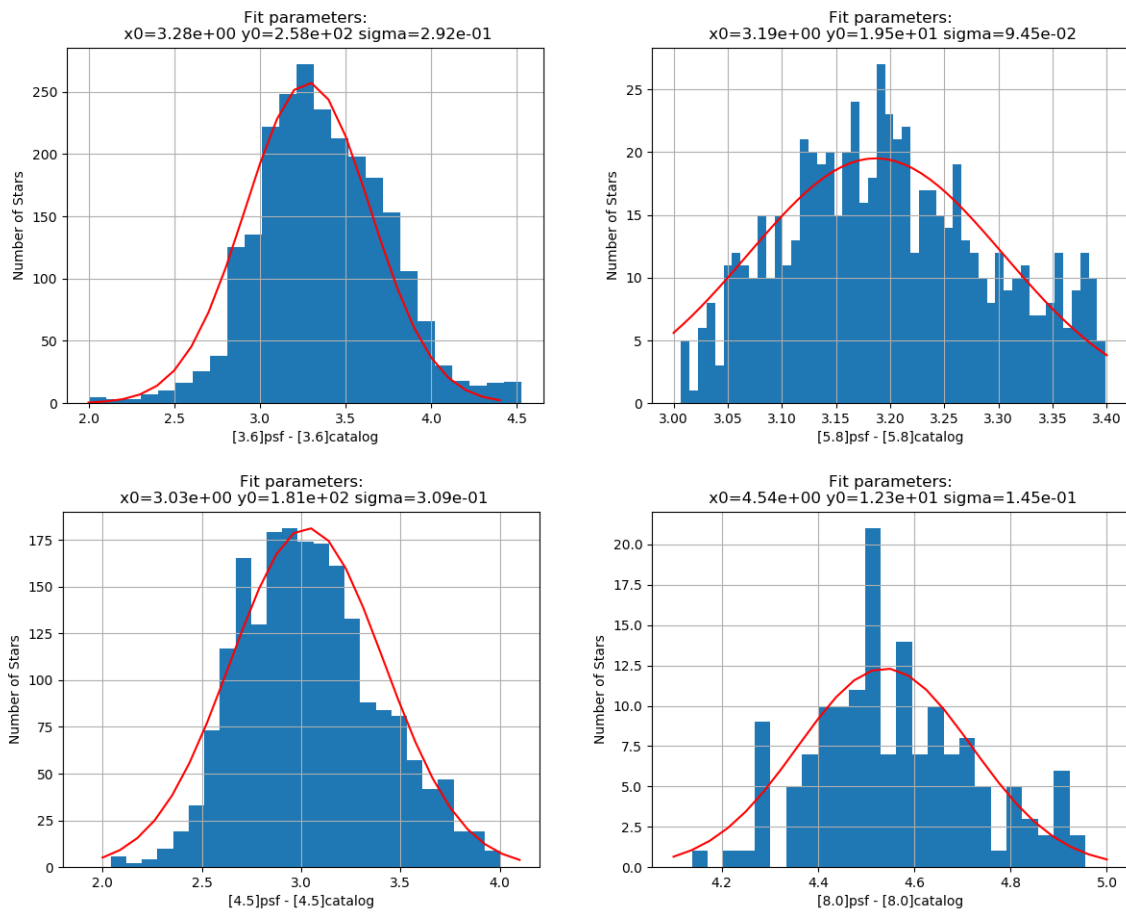


Figure 2.15: Distribution of offset for each MIR filter. Channel 1 (3.6 micron) (top left), Channel 2 (4.5 micron) (top right), Channel 3 (5.8 micron) (bottom left) and Channel 4 (8.0 micron) (bottom right). Offset is calculated from Koenig et. al 2008.

Table 2.11: Sample Catalog of BRC 13 and BRC 14 for NIR (J, H, K), MIR(CH1, CH2, CH3, CH4), Pan-STARR (g,r,i,z,y)

R.A_N	DEC_N	J	Je	H	He	K	Ke	ch1	ch1e	ch2	ch2e	ch3	ch3e	ch4	ch4e	g	ge	r	re	i	ie	z	ze	y	ye
45.16439	60.71191	10.989	0.017	10.773	0.023	10.624	0.018	11.012	0.042	10.641	0.076	10.873	0.068	13.036	0.231	12.727	—	12.347	—	12.149	—	11.984	—	11.902	—
45.57548	60.4964	11.048	0.021	10.769	0.028	10.62	0.02	10.619	0.045	11.201	0.243	10.867	0.058	13.539	0.148	13.425	—	12.802	—	12.43	—	12.13	—	11.9736	0.0067
45.59441	60.53952	11.086	0.021	10.192	0.027	9.939	0.018	—	—	—	—	10.026	0.043	—	—	—	—	—	—	—	—	—	—	—	—
45.17908	60.60609	11.093	0.017	10.913	0.024	10.829	0.019	10.682	0.022	10.49	0.035	10.701	0.032	12.038	0.327	12.84	—	12.444	—	12.194	—	12.029	—	12.0397	0.0005
45.5943	60.62307	11.35	0.021	10.986	0.027	10.906	0.02	—	—	—	—	11.128	0.048	—	—	—	—	—	—	—	—	—	—	—	—
45.24457	60.6005	11.495	0.017	10.701	0.026	10.466	0.019	10.115	0.022	10.078	0.02	10.251	0.012	12.091	0.187	15.9206	0.0029	14.5031	0.0002	13.7255	0.001	13.2484	0.0047	12.9171	0.0022
45.60472	60.51123	11.601	0.019	10.637	0.031	10.332	0.018	—	—	—	—	—	—	—	—	—	—	—	—	—	—	—	—	—	—
45.25435	60.65372	11.607	0.018	10.83	0.023	10.532	0.019	10.307	0.02	10.027	0.02	10.37	0.033	10.423	0.044	16.3303	0.0026	14.8508	0.0002	14.0133	0.0033	13.4654	0.0025	13.098	0.0119
45.56343	60.68442	11.615	0.019	11.305	0.028	11.226	0.02	11.526	0.024	11.293	0.061	11.059	0.052	16.065	0.257	13.4357	0.006	13.364	—	12.975	—	12.694	—	12.5309	0.0032
45.49283	60.76231	11.691	0.023	11.429	0.035	11.298	0.026	—	—	—	—	—	—	13.9435	0.0031	13.262	—	12.961	—	12.713	—	12.6276	0.0068		
45.5403	60.69967	11.703	0.021	11.325	0.031	11.196	0.021	11.505	0.03	11.269	0.047	10.984	0.044	—	—	14.1534	0.0031	13.4129	0.0022	13.137	—	12.887	—	12.7162	0.0022
45.33494	60.7552	11.719	0.021	11.403	0.03	11.24	0.016	11.685	0.03	11.436	0.066	11.639	0.091	—	—	14.2245	0.0004	13.5433	0.0045	13.234	—	12.89	—	12.6607	0.0029
45.43908	60.56294	11.73	0.019	11.404	0.026	11.317	0.02	11.001	0.015	10.859	0.032	11.158	0.015	14.502	0.245	—	—	12.862	—	12.737	—	12.6946	0.0017		
45.46973	60.62446	11.786	0.019	10.988	0.031	10.782	0.023	10.545	0.009	10.382	0.063	10.596	0.028	14.189	0.255	16.0884	0.0032	14.6994	0.0021	13.9584	0.0007	13.4805	0.0019	13.1721	0.0023
45.18121	60.71848	11.791	0.018	10.993	0.022	10.734	0.019	10.803	0.022	10.7	0.079	10.93	0.073	12.852	0.048	16.1763	0.0027	14.7661	0.0034	14.0115	0.0011	13.5466	0.0022		
45.48626	60.7744	11.872	0.019	11.494	0.031	11.383	0.019	—	—	—	—	—	—	—	—	—	—	—	—	—	—	—	—	—	—
45.56286	60.65943	11.894	0.021	11.499	0.031	11.368	0.022	11.636	0.044	11.292	0.057	11.307	0.033	—	—	14.2814	0.0024	13.5946	0.0031	13.3328	—	13.024	0.0201	12.8799	0.0037
45.36104	60.57069	11.968	0.019	11.135	0.027	10.871	0.022	10.479	0.022	10.339	0.025	10.654	0.018	11.929	0.159	16.6412	0.0041	15.1183	0.0016	14.2975	0.0023	13.7992	0.0026	13.4443	0.0008
45.17113	60.76148	11.97	0.018	11.624	0.025	11.567	0.022	—	—	—	—	12.243	0.098	—	—	14.0767	0.0016	13.496	—	13.218	—	13.0563	0.0052	12.9445	0.0013
45.31638	60.61672	11.98	0.018	11.672	0.025	11.541	0.021	11.223	0.011	10.987	0.029	11.479	0.027	9.671	0.043	14.3164	0.0032	13.739	0	13.38	—	13.1585	0.0031	12.9599	0.0032

2.5 Extinction Estimation Methods

2.5.1 Column Density Map

One of the most commonly used method for estimating the extinction is using column density map. In this method, first, the column density is estimated for every pixel and then using that value, extinction is calculated for that pixel. There is a linear relationship used to convert column density $N(H_2)$ to visual extinction A_V . In order to calculate the column density, it is generally assumed that the emission from cold dust at Herschel-SPIRE wavelengths is optically thin. Using this approximation, we can estimate different properties of the region like mass of the different structures, hydrogen column density, temperature etc. Derivation and its limitation are discussed in detail by Hildebrand (1983). The total mass (including both gas and dust) of a region is related to its flux density S_ν by:

$$M_{gas+dust} = 100 \left(\frac{S_\nu D^2}{\kappa_\nu B_\nu(T_{dust})} \right) \quad (2.5)$$

Here D is distance to source, κ_ν is dust opacity per unit mass and $B_\nu(T_{dust})$ is Planck distribution. Usually gas-to-dust ratio is considered as 100 (Deharveng et al. 2012). Calculation of dust opacity depends on the shape, size, its chemical composition, physical structure, grains temperature (Martin et al. 2012; Fischer & Martin 2012; Roy et al. 2013). Preibisch et al. (1993) has suggested to estimate the dust opacity κ_ν for protostellar envelopes as given by;

$$\kappa_\nu = 10 \left(\frac{\nu}{1000 GHz} \right)^2 \quad (2.6)$$

With this method, due to several unknown properties of the dust grains, the dust opacities is uncertain by at least a factor ~ 2 . Hence, the quantities derived by this method also shows uncertainty of the order of ~ 2 . Now using the Herschel fluxes and a modified black-body (also known as grey body), we can estimate the temperature using grey body fitting. This would be the dust temperature and it allows us to estimate the column density of the gas with the same initial assumption. Using the surface brightness F_ν and the temperature T_ν from the grey body fitting, the H_2 column density is given by;

$$N(H_2) = \frac{100F_\nu}{2.8\kappa_\nu B_\nu(T_{dust})m_H\Omega_{beam}} \quad (2.7)$$

where, F_ν is surface brightness expressed in Jy/beam, B_ν is flux density in Jy, m_H is the

hydrogen mass, Ω_{beam} is the beam solid angle and $N(H + H_2)$ is in particles $cm^{-2}mag^{-1}$. The visual extinction can now be estimated from this column density as;

$$N(H + H_2) = 5.8 \times 10^{21} E(B - V) \quad (2.8)$$

And we know from classic relation for interstellar extinction, the color excess can be related to visual extinction as;

$$A_V = 3.1 \times E(B - V) \quad (2.9)$$

Rearranging above two equation will give;

$$A_V = 5.34 \times 10^{-22} N(H + H_2) \quad (2.10)$$

or;

$$A_V = 1.07 \times 10^{-21} N(H_2) \quad (2.11)$$

Hence euqation 2.11 gives the extinction value in V-band for a given line-of -sight.

2.5.2 PNICER

Extinction due to dust is one of the most promising tracer of the gas distribution in interstellar medium. Although, the extinction measurment is limited by several systematic uncertainties occure during calculation of intrinsic color of background sources. To overcome this issue, PNICER is an astronomical software made for estimating extinction using unsupervised machine learning algorithms for individual sources by creating extinction maps (Meingast et al. 2017). Determination of extinction towards a single sources is done by fitting Gaussian Mixture Models along the extinction vector to a nearly extinction-free control field data which makes it possible to define the extinction of sources using probability densities. This fits Gaussian Mixture Models along the extinction vector in arbitrary numbers of dimensions to derive probability densities describing the extinction for each source.

As mentioned, It requires two different regions, namely science field and control field. The science field is the target region and the control field is a region with nearby un-extinct regions (or regions with minimum extinction). This is used to compare the two region's extinction and then using the machine learning algorithm, it makes a map which gives A_v values. It uses JHKs data and their measured color with a given extinction law to get the

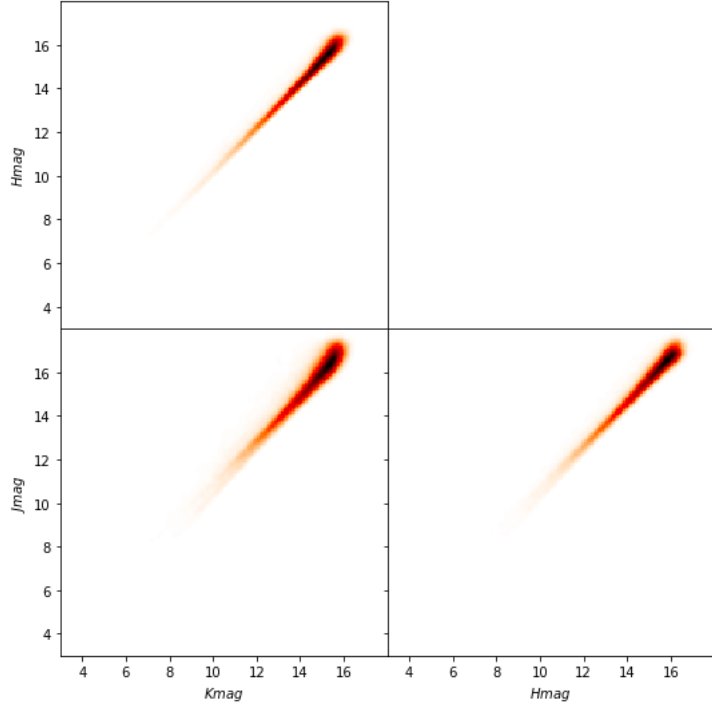


Figure 2.16: Plot generated by the PNICER showing the density distribution for the feature combinations. This plot is generated as an example for Orion A region.

extinction value A_v . PNICER requires few dependencies like numpy, astropy, scipy, matplotlib, and scikit-learn. Using this method, it can effectively eliminates known biases and makes them in cases of deep observational data (in case the number of background sources is significant, or when a large parameter space is used in the intrinsic color distributions). PNICER is offered as an open-source software written entirely in Python.

As mentioned earlier, PNICER uses measured intrinsic magnitudes (or colors) in an extinction-free control field to deredden an extincted sources at the science field. In order to generate an extinction map, let's say of the Orion A molecular cloud, a science field (which is same as Orion A) and another field (may be a few degrees away) as control field.

This two data sets can be retrieved as a FITS table from plateforms like VizieR. After setting up the python environment, one can given the path of these two data sets to initiate the process. An extinction vector is required, which by default set up as a K-

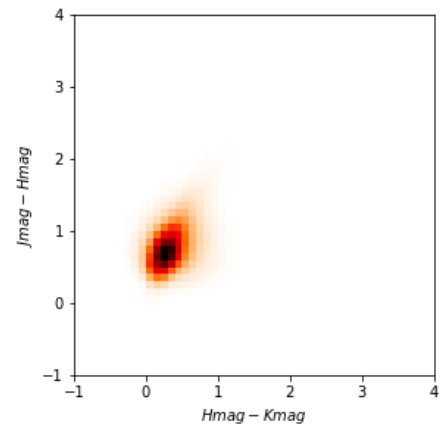


Figure 2.17: Color-Color plot generated by the PNICER showing the $[J-H]$ vs $[H-K]$ distribution.

band normalized array [2.5, 1.55, 1.0] from Indebetouw (2015).

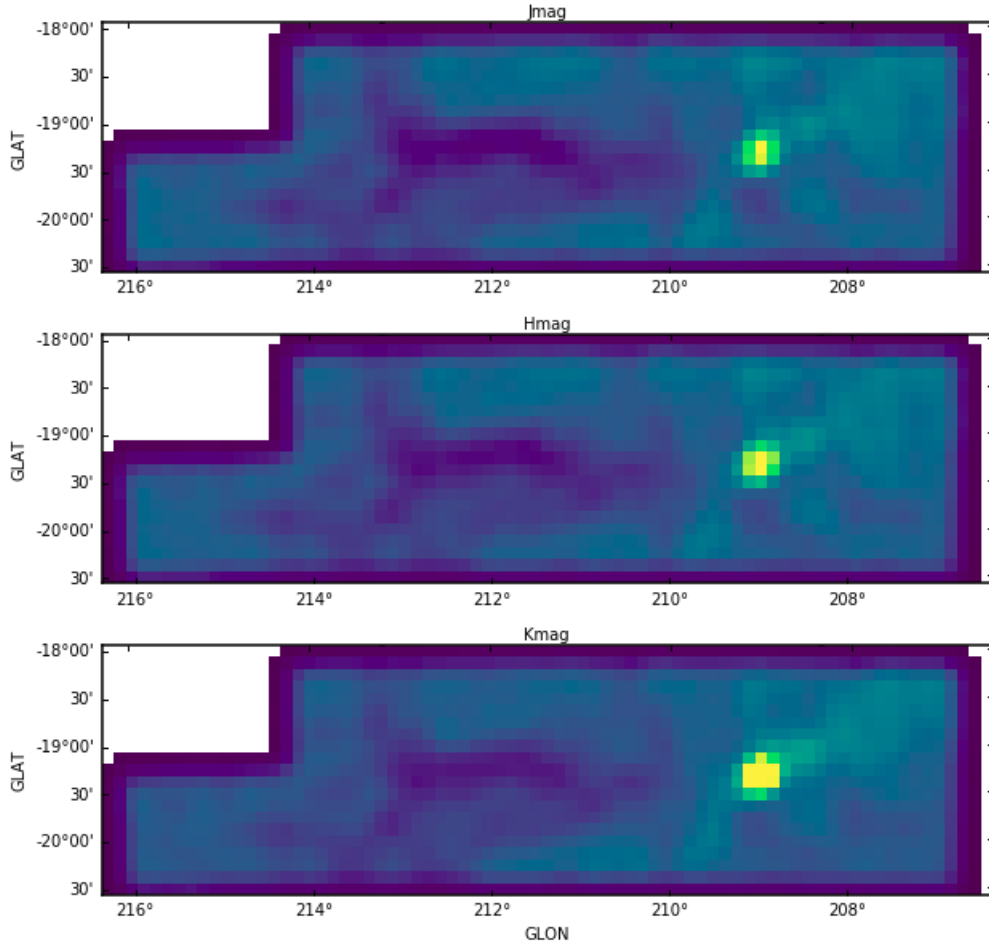


Figure 2.18: Plot generated by the PNICER showing the kernel density distribution map for the feature combinations, Jmag (top), Hmag (middle) and Kmag (bottom). This plot is generated as an example for Orion A region.

Before beginning the extinction map making process, it is always good to take a look at the data. PNICER does include some plotting methods, which helps visualize data. It first plots the density distribution for the feature combinations which is shown in fig. 2.16, following that it also shows the color-color diagram $[J-H]/[H-K]$ which is shown in fig. 2.17.

Next, it also displays a kernel density map of all input features as shown in fig. 2.18, leading to this, finally prepares the extinction map of the region. This map comes along with two other maps also, first the error in A_v and second the number distribution. The entire panel is shown in fig. 2.19. For more details on the part of unsupervised learning technique, please refer Meingast et al. (2017). The steps involved in generating the extinction map is given in detail at Smeingast (2017).

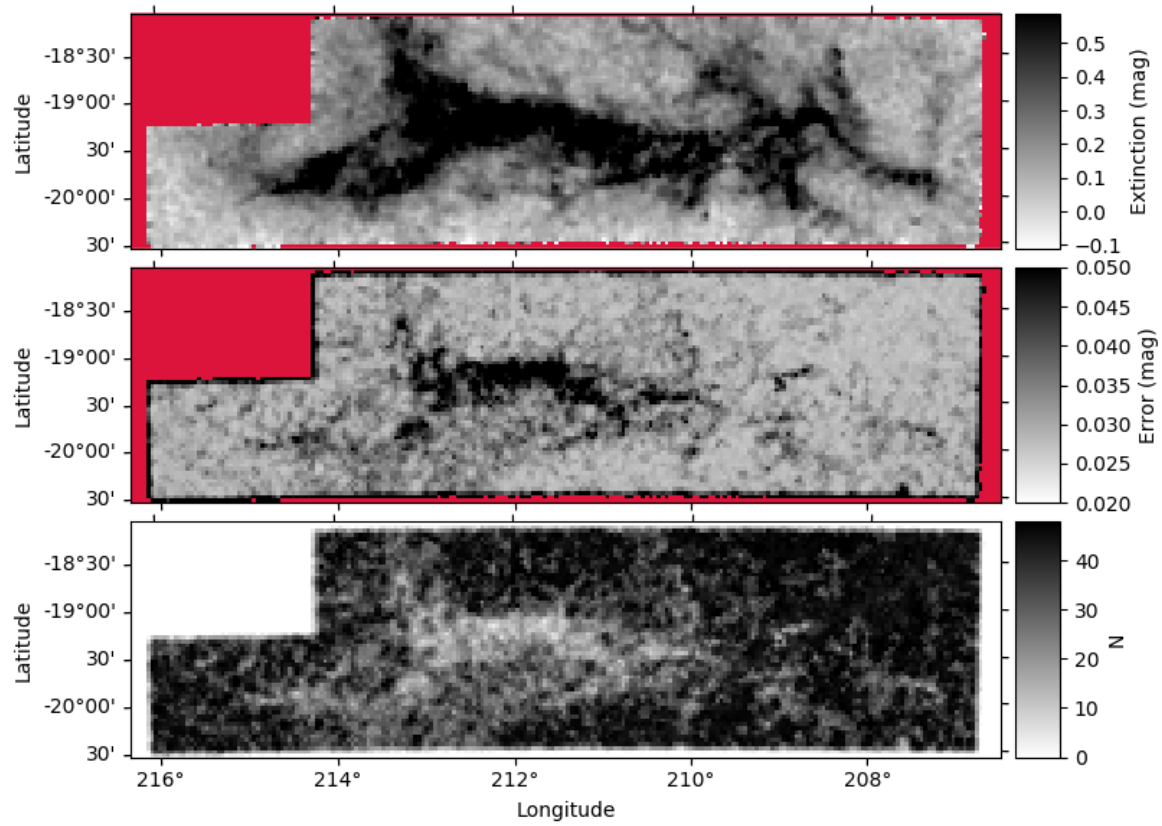


Figure 2.19: Plot generated by the PNICER showing the extinction map in V-band (top), the uncertainty map (middle) and a number density map (bottom) . This plot is generated as an example for Orion A region.

2.5.3 Using JHKs[CH1][CH2] photometry

This method is suggested by Gutermuth et al. (2009) (appendix A, phase 2) which uses five photometric band to estimate the extinction. In this method, H and K band are essential, J and [CH1][CH2] are used whenever they are available. The data used must have high quality photometry ($\sigma < 0.1$). These details are sufficient to disreminate the excess source with those which are showing NIR excess because of the line of sight dust only (Gutermuth et al. 2005). To estimate the line of sight extinction, which in this method is parameterized by color excess E_{H-K} from the line of sight reddening due to dust.

The process of estimating the extinction is two folds, in the first case, we use all the sources which has J band data available along with H and K_S photometric data. This also uses color excess ratio (E_{J-H} / E_{H-K}) with the baseline color of main sequence stars from Bessell & Brett (1988) classical T-Tauri stars (CTTS) locus from Meyer et al. (1997) (see section ??). This is accomplished by constraining the $[J-H]_o \leq 0.6$ which is a approximation for the intrinsic color of low mass stars. Using all these, the first set of equations are given by;

$$[J - H]_o = 0.58 \times [H - K]_o + 0.52; \quad [H - K]_o > 0.14 \quad (2.12)$$

$$[J - H]_o = 0.60; \quad [H - K]_o \leq 0.14 \quad (2.13)$$

from the standard equation of color transformation, we can write;

$$[H - K]_o = [H - K]_{meas} - ([J - H]_{meas} - [J - H]_o) \times \frac{E_{J-H}}{E_{H-K}} \quad (2.14)$$

Putting eq. 2.12 to eq. 2.14, we will get;

$$[H - K]_o = \frac{[J - H]_{meas} - \frac{E_{J-H}}{E_{H-K}} \times [H - K]_{meas} - 0.52}{0.58 - \frac{E_{J-H}}{E_{H-K}}} \quad (2.15)$$

and putting eq. 2.13 to eq. 2.14, we will get;

$$[H - K]_o = [H - K]_{meas} - ([J - H]_{meas} - 0.6) \times \frac{E_{J-H}}{E_{H-K}} \quad (2.16)$$

Using eq. 2.15 and eq. 2.16, one set of intrinsic color can be calculated but these calculation has to be restricted for only those sources which has J band data available.

For rest of the sources where J band is unavailable but [CH1] and [CH2] is available, we make use of color excess $\frac{E_{[CH1]-[CH2]}}{E_{H-K}}$, derived from Flaherty et al. (2007) along with the baseline colors YSO locus of [CH1]-[CH2] v/s [H]-[K] color-color space given in Bessell & Brett (1988); Gutermuth et al. (2005). This constrain is forced by applying condition $[H - K]_o \leq 0.2$, which is an approximation for intrinsic color of low mass stars. Using these, the second set of equations are as follow;

$$[H - K]_o = 1.33 \times [[CH1] - [CH2]]_o + 0.133; \quad [[CH1] - [CH2]]_o > 0.06 \quad (2.17)$$

$$[H - K]_o = 0.20; \quad [[CH1] - [CH2]]_o \leq 0.06 \quad (2.18)$$

from the standard equation of color transformation, we can write;

$$[H - K]_o = [H - K]_{meas} - ([[CH1] - [CH2]]_{meas} - [[CH1] - [CH2]]_o) \times \left(\frac{E_{H-K}}{E_{[CH1]-[CH2]}} \right) \quad (2.19)$$

Putting eq. 2.17 to eq. 2.19, we will get;

$$[H - K]_o = \frac{1.33 \times \left(\frac{E_{H-K}}{E_{[CH1]-[CH2]}} \times [H - K]_{meas} - [[CH1] - [CH2]]_{meas} \right) - 0.133}{\left(1.33 \times \frac{E_{H-K}}{E_{[CH1]-[CH2]}} \right) - 1} \quad (2.20)$$

Using these two steps, we would have $[H-K]_o$ for all the source (from eq. 2.15, eq. 2.16, eq. 2.18 and eq. 2.20). Now using the following steps, one can arrive at the visual extinction (A_v) value from the intrinsic color $[H-K]_o$;

we can define;

$$\frac{E_{H-K}}{E_{B-V}} = \frac{E_{H-V}}{E_{B-V}} - \frac{E_{K-V}}{E_{B-V}} \quad (2.21)$$

From Rieke & Lebofsky (1985); for the interstellar medium $\frac{E_{H-V}}{E_{B-V}} = -2.55$ and $\frac{E_{K-V}}{E_{B-V}} = -2.744$, such that;

$$\frac{E_{H-K}}{E_{B-V}} = \frac{E_{H-V}}{E_{B-V}} - \frac{E_{K-V}}{E_{B-V}} = 0.194 \quad (2.22)$$

And as we know for the interstellar medium, the color excess to visual extinction ratio is given by;

$$\frac{E_{B-V}}{A_v} = 3.1 \quad (2.23)$$

Using the above two equations;

$$A_v = \frac{3.1}{0.194} \times E_{H-K} = 15.979 \times ([H - K]_{meas} - [H - K]_o) \quad (2.24)$$

Where $[H - K]_{meas}$ is the measured color excess and $[H - K]_o$ is the intrinsic color calculated from eq. 2.15, eq. 2.16, eq. 2.18 and eq. 2.20). Hence the extinction in V-band can be calculated from equation 2.24.

2.6 YSO Identification

In this chapter, we have discussed the photometry methods (Aperture photometry and PSF photometry) in sec. 2.2.1 and sec. 2.2.2. Then using that data, we have dereddened the extincted sources in sec. 3.3. The reason behind the dereddening is wipe out the contribution of gas and dust present between the source and the observer. But why do we need to take out that contribution? The answer lies in the fact that the reddening is not just caused by interstellar medium, but it is also an excellent tracer of young sources. The young stellar objects (see sec. 1.6) happens to show a reddening due to interstellar reddening as well as circumstellar reddening. This circumstellar reddening happed because of the presence of circumstellar disc (or envelope) present. So if we take out the interstellar reddening from the total reddening (means if we dereddening), we can identify the sources which show extra extincted object (also called ‘excess’), and thus we can identify the young stellar objects. Hence to identify the YSO, first we have to deredden the sources by methods explained in sec. 3.3. This excess is identified in near infrared spectrum, as the UV/optical flux produced by young protostar is absorbed by the circumstellar disc, which re-radiates the energy in NIR spectrum. Based on this NIR excess, the sources can be classified in Class I/II/III sources (more detail 1.6.2).

The identification and classification of these YSO is explained as a multiphase process. (Gutermuth et al. 2005, 2009). The first phase eliminates the false NIR excess sources and first set of YSOs. This method uses the IRAC four bands. Second section deals with identification of another set of YSOs using JHKs[CH1][CH2] sources. The final phase adds and checks the YSOs with their MIPS 24 μm photometric data.

2.6.1 YSO identification:Phase I

Beginning of first phase starts with eliminating the false source like PAH background galaxies, AGNs etc. To eliminate the active star forming galaxies, it uses the fact that these sources shows very red [CH3] and [CH4] colors (Stern et al. 2005). Sources which obey following constrains are identified as active PAH galaxies;

$$[CH2] - [CH3] < \frac{1.05}{1.2} \times ([CH3] - [CH4] - 1) \quad (2.25)$$

$$[CH1] - [CH3] < \frac{1.5}{2} \times ([CH2] - [CH4] - 1) \quad (2.26)$$

$$[CH2] - [CH3] < 1.05 \quad (2.27)$$

$$[CH3] - [CH4] > 1.00 \quad (2.28)$$

$$[CH1] - [CH3] < 1.50 \quad (2.29)$$

$$[CH2] - [CH4] > 1.00 \quad (2.30)$$

$$[CH2] > 11.50 \quad (2.31)$$

A similer constraints can be drawn for the broad-line AGN, but these sources shows their MIR color largely consistent with the true NIR excess YSOs (Stern et al. 2005). Unlike the previous case where it uses color-color plot, this time it uses color-magnitude plot which is [CH2] v/s [CH2]-[CH4] plot. The sources which follows given constraints are identified as broad line AGNs can are discarded;

$$[CH2] - [CH4] > 0.5 \quad (2.32)$$

$$[CH2] > 13.5 + ([CH2] - [CH4] - 2.3)/0.4 \quad (2.33)$$

$$[CH2] > 14.0 + ([CH2] - [CH4] - 0.50) \quad (2.34)$$

$$[CH2] > 14.5 + ([CH2] - [CH4] - 1.2)/0.3 \quad (2.35)$$

$$[CH2] > 13.5 \quad (2.36)$$

To eliminate the unresolved knots of shock emission which is another source of contamination, it again uses the color-color diagram [CH1]-[CH2] v/s [CH3]-[CH4]. Following are the conditions for which unresolved knots of shock emission are identified;

$$[CH1] - [CH2] < \frac{1.20}{0.55} \times ([CH2] - [CH3] - 0.3) + 0.8 \quad (2.37)$$

$$[CH2] - [CH3] \leq 0.85 \quad (2.38)$$

$$[CH1] - [CH2] > 1.05 \quad (2.39)$$

There is another source which can pretend to be a NIR excess source, which is when a resolved PAH emission has contaminated the photometric apertures of faint field stars which shows spurious excess emission in [CH3] and [CH4]. These can be identified with following conditions;

$$\sigma_1 = \sigma[[CH2] - [CH3]] \quad (2.40)$$

$$\sigma_2 = \sigma[[CH1] - [CH2]] \quad (2.41)$$

$$[CH1] - [CH2] - \sigma_2 \leq 1.40 \times (([CH2] - [CH3]) + \sigma_1 - 0.7) + 0.15 \quad (2.42)$$

$$[CH1] - [CH2] - \sigma_2 \leq 1.65 \quad (2.43)$$

Now once all these contaminants are eliminated from the database, first set YSOs can be identified. With all those sources, which shows following are identified as Class I YSOs;

$$[CH2] - [CH3] > 0.70 \quad (2.44)$$

$$[CH1] - [CH2] > 0.70 \quad (2.45)$$

With those objects remaining, sources which shows following conditions are identified as Class II YSOs;

$$\sigma_3 = \sigma[[CH2] - [CH4]] \quad (2.46)$$

$$\sigma_4 = \sigma[[CH1] - [CH3]] \quad (2.47)$$

$$[CH2] - [CH4] - \sigma_3 > 0.50 \quad (2.48)$$

$$[CH1] - [CH3] - \sigma_4 > 0.35 \quad (2.49)$$

$$[CH1] - [CH3] + \sigma_4 \leq \frac{0.14}{0.04} \times (([CH2] - [CH4] - \sigma_3) + 0.5) \quad (2.50)$$

$$[CH1] - [CH2] - \sigma_4 > 0.15 \quad (2.51)$$

2.6.2 YSO identification: Phase II

Second phase of YSO identification involves five band identification scheme JHKs[CH1][CH2], high quality photometric data with read flag set as '222' in case of JHKs from 2MASS can be considered. After dereddening the sources by following the procedure explained in sec. 2.5.3, the sources can be identified as Class II sources if they follow these conditions;

$$\sigma_1 = \sigma[[CH1] - [CH2]]_{meas} \quad \sigma_2 = \sigma[[K] - [CH1]]_{meas} \quad (2.52)$$

$$[[CH1] - [CH2]]_o - \sigma_1 > 0.101 \quad (2.53)$$

$$[[K] - [CH1]]_o - \sigma_2 > 0 \quad (2.54)$$

$$[[K] - [CH1]]_o - \sigma_2 > -2.85714 \times ([[CH1] - [CH2]]_o - \sigma_1 - 0.101) + 0.5 \quad (2.55)$$

$$[CH1]_o < 16.30 \quad (2.56)$$

Sources which follows following condition along with the previous constraints;

$$[[K] - [CH1]]_o - \sigma_2 > -2.85714 \times ([[CH1] - [CH2]]_o - \sigma_1 - 0.401) + 1.70 \quad (2.57)$$

$$[CH1]_o < 16.80 \quad (2.58)$$

The constraint applied in eq. 2.56 and eq. 2.58, is actually decided based on the depth of MIR survey data. These two conditions basically eliminates faint extragalactic contaminants. Sources identified with this phase along with phase I are considered as YSO set.

2.6.3 YSO identification: Phase III

This phase rechecks the YSO set from phase I and phase II, and identifies deeply embedded YSOs using MIPS 24 μm which is not possible by using IRAC and 2MASS. This also search for heavily reddened Class II sources which is misidentified as Class I. Following conditions are used to identify Class II sources;

$$[CH3] - [24] > 2.5 \quad (2.59)$$

$$[CH2] - [24] > 2.5 \quad (2.60)$$

and as protostar Class I if they follow;

$$[CH2] - [24] > 4.5 \quad (2.61)$$

$$[CH4] - [24] > 4.0 \quad (2.62)$$

Hence by using all these three phase, we can make YSO catalog from the survey data.

2.7 Spectral Energy Distribution (SEDs) Modelling

We have seen the spectral energy distribution in chapter 1 sec. 1.6.2. Using that the YSO classification is also discussed. Now in this section we are going to discuss about modelling the YSOs and extracting various physical parameters out of this. Estimation of physical parameters like photospheric temperature (T_{eff}), Bolometric luminosity (L), mass (M), radius (R) etc. are extreamly important to study the star formation scenario in any given region. This section in divided into two subsection; first, it discusses one of the most popular photospheric model for protostellar system, its concept and working; secondly, it explains the tool used to model the SEDs.

2.7.1 Theoretical SED Model

In order to replicate the stellar conditions, many models have been proposed. Modelling the spectral energy distribution of the stellar photosphere is one of the most common method to study star formation. The stellar photosphere is the outer surface layers from which radiation escapes the star. These layers can be mathematically probed using model atmospheres. The synthetic spectra can be generated by formulating the radiative transfer equations on the model photosphere. These model spectra is then used to compair with the actual observed spectra (or some photometric data points) to extract various physical parameter of the star. In order to establish a model photosphere, assumptions has to be considered beforehand. Based on these assumptions, equations of photospheric model is formulated.

The basic idea behind the photospheric model is that it can simulate the variation of temperature and pressure at different scales of photosphere. The variation in these quantities depends on various parameters of the star, but it is predominantly varies according to the radiation flux passing the different levels of photosphere and the succesive absorption and emission by the same levels. These different depths of the star act differently amongs themselves. However, the flux passing through these different depths are, if considered,

constant (which is given by the Stefan-Boltzmann law; $F = \sigma T_{eff}^4$) then the only parameter to be taken care of is the absorption through these layers. This is governed by the term called *Opacity*. Now to be very elementary, the opacity is a function of the photospheric temperature (T_{eff}), pressure and the composition of the layer of photosphere. In other words, the composition is nothing but the metallicity of the star. Now surface gravity (g) can be treated as a proxy variable for pressure. So in order to model the photosphere as a function of its depths, we have got our parameter space which consists of [T_{eff} , metallicity, surface gravity (g)].

Simplest models use the assumption of 1-D plane-parallel photosphere, which implies that the parameter space (pressure, temperature) depends only on the depth of the atmosphere. However, this assumption fails for thick atmospheres and hence, spherically symmetric atmosphere is assumed in such case. Another common assumption used while modelling is local thermodynamic equilibrium (LTE). This assumption combines thermal, chemical and mechanical equilibrium and inflow of radiation can be taken to be a blackbody spectrum. The Maxwell-Boltzmann distribution can be applied to calculate the number of atoms or molecules occupying different excited energy states and the Saha equation can be used to determine the number of atoms in different ionization states. Many models also assume hydrostatic equilibrium, and that the total flux passing through the outer layers remains constant with depth.

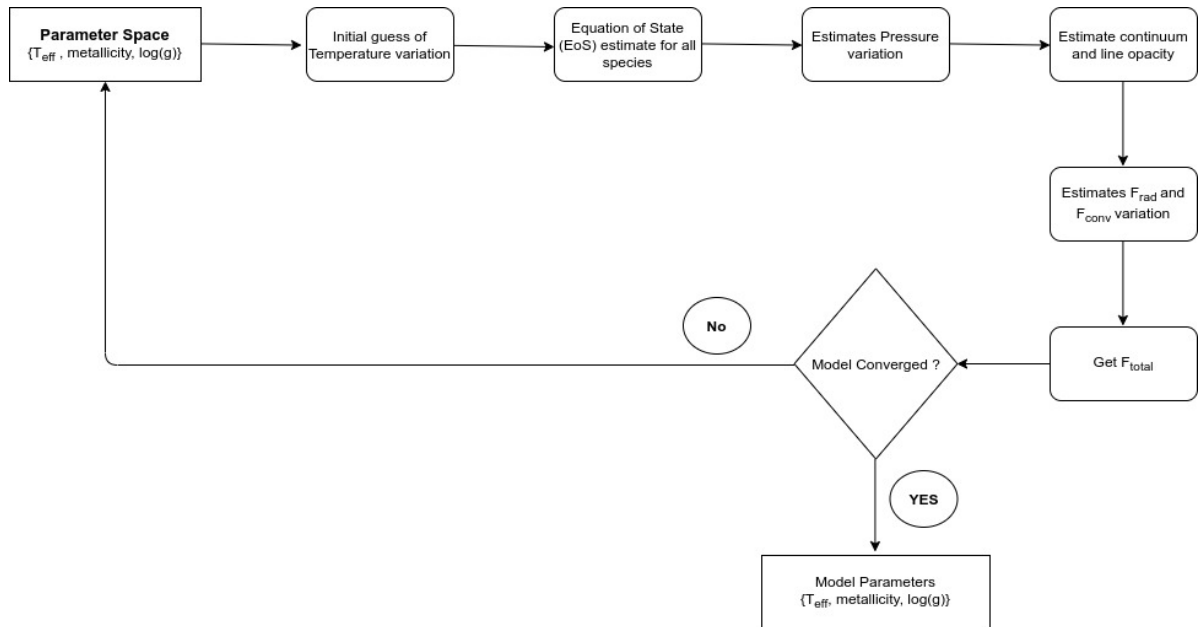


Figure 2.20: Flow chart showing the photosphere modelling process.

One of the tricky parameter here is the opacity, which is extreamly important to model the atmosphere. The amount of flux absorbed by the different layers of photosphere depends vividly on opacity, which intern is a function of composition of these different photospheric layers. It is computationally impossible to model the absorption feature of every element/molecule present in that layer. This problem is taken care by method called *opacity sampling*. This technique samples the wavelength space into smaller number of bins (closely about 1% of the space).

Table 2.12: Some commonly used theoretical modeles with their parameter grid space

Model	T_{eff} (K) (ΔT_{eff})	Metallicity (Δ Metallicity)	Log(g) (Δ Log(g))
Kurucz ATLAS9	3500 - 50000 (250)	-2.5 - +0.5 (0.5)	0.0 - +5.0 (0.5)
Phoenix NextGen	800 - 70000 (100)	-4.0 - +0.5 (0.5)	-0.5 - +5.5 (0.5)
BT-NextGen	2700 - 70000 (100)	-4.0 - +0.5 (0.5)	-0.5 - +5.5 (0.5)
BT-Dusty	1700 - 2700 (100)	-4.0 - +0.5 (0.5)	-0.5 - +5.5 (0.5)
BT-Cond	800 - 70000 (100)	-4.0 - +0.5 (0.5)	-0.5 - +6.0 (0.5)
BT-Settle	400 - 70000 (100)	-4.0 - +0.5 (0.5)	-0.5 - +6.0 (0.5)
BT-Settle CIFIST	1200 - 7000 (100)	0	2.5 - 5.5 (0.5)

There is another method to handle the opacity called *opacity distribution function*. These are the pretabulated statistical function of line opacity (opacity defined over pressure and temperature for given set of abundance), generated for different set of pressure and temperature grid, computes the opacity for entire grid and samples it according to the wavelength bin. Fig. 2.20 shows the iterative process of modelling the atmosphere. It initialize the process with the parameter space assumed over the different layers of atmosphere. After that the pressure is estimated with the preassumed equation of state (it can be different for different atmospheric model). This leads to estimating the different line opacities with pressure and temperature gradient for each layer. After that, formulating the equation of radiative transfer, convective and radiative flux is estimated. Using these, we can calculate the total flux crossing each layer. A converging value of flux leads to finalizing the parameter grid, otherwise, the deviation parameter space is calulated and feedback is applied to restart the process with an updated parameter space. Some of the commonly used models with their parameter grid is shown in table 2.12.

2.7.2 VOSA SED Analyzer

VO SED Analyzer (VOSA) is a online tool designed by Spanish Virtual Observatory (SVO) to perform task related to many astronomical analysis. This tool is developed to perform task in a user friendly environment in an automatic manner. VOSA is able to perform following tasks;

- VOSA can read photometric table build by user in given specific formate.
- Using this user is able to make query to several catalogs accessible through VO services. This makes wavelength coverage to increase such that the user can analyze the data.
- Using this user can make query to various theoretical models and user can estimate their own synthetic photometry.
- Using this user can perform a test statistically to examine which model can produce the observed data with least uncertainty. This allows user to make fitting optionally as well as optimize the interstellar extinction, such that, user can make likelihood of the model space as well as the reddening.
- To make the bolometric correction VOSA uses the best-fit model.
- Using modelling user can estimated bolometric luminosity for all sources.
- After modelling the SED, VOSA can generate a HR diagram using the estimated parameters using appropriate isochrones and evolutionary tracks.
- VOSA also provides an estimation of the mass and age of each source using the HR diagram.

2.7.2.1 IR excess detection and Model Fitting

This project aims to identify the young stellar object and estimate the physical properties like age, mass, luminosity etc. This can be achieved by fitting the spectral energy distribution with a theoretical model. VOSA provides large variety of theoretical model. VOSA helps to build a Spectral Energy Distribution (SED) for each object in the file combining user input data with data obtained from VO catalogues, taking into account extinction properties for deredening the observed fluxes and marking photometric points where IR or UV excess is detected. To do this task VOSA needs user photometric data in as specific format.

Table 2.13: Sample VOSA input file

Obj ID	RA	DEC	dis	Av	filter	flux/mag	error	pntopts	objopts
11203	45.44665	60.64207	2100+/-300	—	NOAO/NEWFIRM.JX	12.867	0.021	—	Av:0.5/25
11203	45.44665	60.64207	2100+/-300	—	NOAO/NEWFIRM.HX	12.451	0.034	—	Av:0.5/25
11203	45.44665	60.64207	2100+/-300	—	NOAO/NEWFIRM.KX	12.3	0.019	—	Av:0.5/25
11203	45.44665	60.64207	2100+/-300	—	Spitzer/IRAC.I1	12.133	0.012	—	Av:0.5/25
11203	45.44665	60.64207	2100+/-300	—	Spitzer/IRAC.I2	11.872	0.029	—	Av:0.5/25
11203	45.44665	60.64207	2100+/-300	—	Spitzer/IRAC.I3	12.126	0.022	—	Av:0.5/25
11203	45.44665	60.64207	2100+/-300	—	Spitzer/IRAC.I4	13.855	0.313	—	Av:0.5/25
11203	45.44665	60.64207	2100+/-300	—	PAN-STARRS/PS1.g	15.7704	0.0011	—	Av:0.5/25
11203	45.44665	60.64207	2100+/-300	—	PAN-STARRS/PS1.r	14.9093	0.0021	—	Av:0.5/25
11203	45.44665	60.64207	2100+/-300	—	PAN-STARRS/PS1.i	14.44	0.0037	—	Av:0.5/25
11203	45.44665	60.64207	2100+/-300	—	PAN-STARRS/PS1.z	14.1575	0.0035	—	Av:0.5/25
11203	45.44665	60.64207	2100+/-300	—	PAN-STARRS/PS1.y	13.9236	0.0012	—	Av:0.5/25

The sample vosa input file is shown in table 2.13. The wide variety of filters available at VOSA library make it convenient to do the entire process without taking care of filter transmission profile, convolution etc.

Most of the models used by VOSA for the analysis of the observed SEDs include only a photospheric contribution. But the observed SED for some objects can include the contribution not only from the stellar photosphere but also from other components as disks or dust shells. In these cases, some excess will appear. These excess sources can be identified by VOSA.

The algorithm used by VOSA to estimate the presence of infrared excess is an extension of the idea presented by Lada (2006). The main idea is calculating, point by point in the infrared, the slope of the regression of the log-log curve showing νF_ν vs ν . At a first approximation, when this slope becomes smaller than 2.56, infrared excess starts. The identification of excess is very prone to bad photometric data point. In order to avoid false IR excess detection, following steps are followed;

1. Process initiates with photometric point considered as $\lambda > 21500\text{\AA}$
2. If a point is labeled as ‘nofit’, then they are not considered for further steps.
3. The linear regression is done for every points from the first to is calculated.
4. Given that $y = \log(\nu F_\nu)$ which is a function of $x = \log(\nu)$ value calculated for this point with a line starting on initial point showing $slope = 2.56$, is called as y_L . The slope = 2.56 is called here as ‘critical slope’.
5. VOSA marks “excess suspicious” to a point if it qualifies both of the given conditions;

- Regression slope (b) with the uncertainty in the slope, is smaller than critical slope, that is;

$$b + \sigma(b) < 2.56 \quad (2.63)$$

- The observed value of y equal to minimu of 3σ above the value calculated from critical slope, that is;

$$(y_{obs} - y_l) > 3\sigma(y) \quad (2.64)$$

6. If a point is marked as ‘suspicious’, then it will not be considered for further process of linear regressions.
7. If two succesive points are identified as ‘suspicious’ then VOSA marks infrared excess to the first points of the beginning.
8. If a point is marked as ‘suspicious’, however if the next point is not marked, then VOSA keeps the marks as it is. The first point (the suspicious one) is not be considered for further steps in makeing linear regression, however VOSA keep on checking the further points.
9. If VOSA finds the last point as ‘suspicious’ such that it qualifies both excess conditons mentioned above so that the point is taken at the beginning of IR excess.
10. In addition to these, one final condition is taken by VOSA. The slope calculated with the above method for one of the last two points at least, then it has to be sigma matched with smaller than critical slope of 2.56 ¹.

2.7.2.2 SED Modelling

Once the IR-excess sources are identified, the photometric data point which belongs excess are no longer considered to fitting the theoretical model. Modelling process involves the compairision of the observed SED with the theoretical SEDs of a given model (multiple models can be selected by user, but it will take longer time with bigger grid). The best fitted grid point corosponds to the grid paramter $[T_{eff}, \log(g), \text{mettalicity}]$. The best fitting is

¹Process of estimating the IR-excess source does not classify them further into class I, II and III. This process will however, be able to make user identify excess sources and exclude excess data from modelling, please refer to vosa help-desk for step-wise procedure of IR excess identification.

identified by using least square minimization process. The fitting accuracy is checked by calculating the reduced χ^2_r value, which is given by;

$$\chi^2_r = \frac{1}{N - n_p} \times \sum_{i=1}^N \left(\frac{(Y_{i,o} - M_d Y_{i,m})^2}{\sigma_{i,o}^2} \right) \quad (2.65)$$

Where N is total number of photometric data points; n_p is number of fitted parameters; Y_o is observed flux; Y_m is theoretical flux; σ_o is error in observed flux; M_d is the multiplicative dilution factor.

Calculation of M_d is done by scaling the observed SED to the theoretical SED from the model chosen. This factor is also given by the ratio of radius to distance of source ($M_d = (R/D)^2$). The distance is given by the user in the input file as shown in table 2.13.

2.7.2.3 Synthetic Photometry and Bolometric Luminosity

Once the source is modelled with using a given theoretical model, the modelled source is now can be used to generate the synthetic photometry. Let the theoretical spectra is given by $F_i(\lambda)$ with the given unit $\text{erg/cm}^2/\text{s}/\text{\AA}$ and let the given filter is given by a dimensionless filter response curve given by $G_f(\lambda)$. Then the synthetic photometry corresponding to the F_i spectra as it is observed through the given filter G_f can be expressed by;

$$F_{i,f} = \int_{\lambda} F_i(\lambda) N_f(\lambda) d\lambda \quad (2.66)$$

where the $N_f(\lambda)$ is the normalized filter response given by;

$$N_f(\lambda) = \frac{G_f(\lambda)}{\int G_f(x) dx} \quad (2.67)$$

The synthetic photometry can be used to confirm whether the difference in physical parameters, as obtained from the model fitting, can result in the observed variations in the colors of the two groups.

The best fitting model is used to calculate the total observed flux for each source of the sample. The total theoretical flux for the source can be calculated as given by;

$$F_M = \int M_d \cdot F_M(\lambda) d\lambda \quad (2.68)$$

To estimate the total observed flux for the source, substitute the fluxes corresponding to the observing filters by the observed ones such that as much as flux possible comes from

the observations.

$$F_{tot} = \int M_d \cdot F_M(\lambda) d\lambda + F_{obs} - F_{mod} \quad (2.69)$$

Theoretical density flux corresponding to the observed one $F_{o,f}$ can be calculated using the normalized filter response N_f given by;

$$F_{M,f} = \int M_d \cdot F_M(\lambda) N_f(\lambda) d\lambda \quad (2.70)$$

To calculate the total observed flux, it is important to estimate the amount of overlapping among different filter observations. To do that, it approximates the coverage for each filter with its effective width after that it can identify spectral regions such that we define a *overlapping factor* as;

$$over_r = \frac{\sum W_i}{(\lambda_{max,r} - \lambda_{min,r})} \quad (2.71)$$

This can be used to estimate the degree of oversampling in every region and hence, the total observed and model flux can be approximate by;

$$F_{obs} = \sum_f \frac{F_{o,f} \cdot W_{eff,f}}{over_r} \quad (2.72)$$

and;

$$F_{mod} = \sum_f \frac{F_{M,f} \cdot W_{eff,f}}{over_r} \quad (2.73)$$

So total flux is given by;

$$F_{tot} = F_M + \sum_f \frac{[F_{o,f} - F_{M,f}] \cdot W_{eff,f}}{over_r} \quad (2.74)$$

Where $F_{M,f}$ and $F_{o,f}$ are the model and observed flux densities corresponding to the filter f. Now the bolometric luminosity can be given by;

$$L(L_\odot) = 4\pi D^2 F_{obs} \quad (2.75)$$

2.7.2.4 Estimation of stellar radius and mass

The multiplicative dilution factor (M_d) calculated from the fitting can be used to estimate the stellar radius given by;

$$R_1 = \sqrt{D^2 M_d}; \quad \delta R_1 = R_1 \frac{\delta D}{D} \quad (2.76)$$

There is another way of calculating the stellar radius using the T_{eff} and L_{bol} given by;

$$R_2 = \sqrt{\frac{L_{bol}}{4\pi\sigma_{SB}T_{eff}^4}}; \quad \delta R_2 = \sqrt{\frac{1}{4}\left(\frac{\Delta L_{bol}}{L_{bol}}\right)^2 + 4\left(\frac{\Delta T_{eff}}{T_{eff}}\right)^2} \quad (2.77)$$

These values of stellar radius can be used to estimate mass, similar to estimation of stellar radius, mass will also have two expressions given by;

$$M = \frac{10^{Log(g)} R^2}{G_{NW}} \quad (2.78)$$

putting expression of R_1 and R_2 in above equation is given by;

$$M_1 = \frac{10^{Log(g)} R_1^2}{G_{NW}}; \quad \delta M_1 = M_1 \sqrt{\ln(10)^2 (\Delta Log(g))^2 + 4\left(\frac{\Delta R_1}{R_1}\right)^2} \quad (2.79)$$

and;

$$M_2 = \frac{10^{Log(g)} R_2^2}{G_{NW}}; \quad \delta M_2 = M_2 \sqrt{\ln(10)^2 (\Delta Log(g))^2 + 4\left(\frac{\Delta R_2}{R_2}\right)^2} \quad (2.80)$$

2.7.2.5 Estimation of age and mass from H-R diagram

Till now we have explained the estimation of T_{eff} and L_{bol} which can be used to plot the H-R diagram. Using various types of available theoretical isochrones and evolutionary track (e.g. BT-Settle, Siess, BACH15 etc.), we can estimate the age (and mass) of the source. Once the HR diagram is plotted, then following are the steps involved in estimating the age and mass ² from the plot;

²The similar algorithm used for mass calculation but with Evolutionary tracks instead of isochrones. There are several small conditions to be checked for falling calling the D1 and D2 distances as a final value that are not mentioned here to keep the explanation brief, please refer to vosa help-desk on such conditions.

1. Identifying the points $(T_{eff}, \log L)$ falling within the isochrones (and Evolutionary tracks). For those who do fall, the following steps has been taken;
2. Using $(T_{eff,min}, T_{eff,max})$ and $(\log L_{min}, \log L_{max})$, making the small grid of 9 points (e.g. $(T_{eff}, \log L)$, $(T_{eff,min}, \log L)$, $(T_{eff,max}, \log L)$, $(T_{eff}, \log L_{min})$...) as shown in fig. 2.21. For each source following are the steps carried out using these 9 point grid;

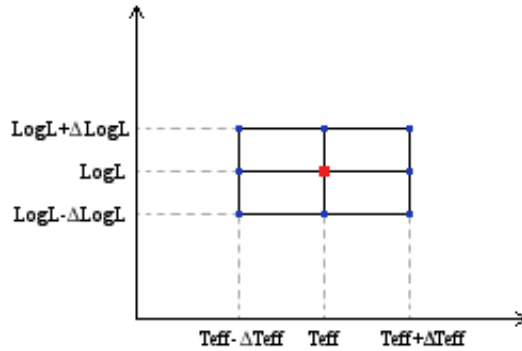


Figure 2.21: Uncertainty grid showing the nine points to calculate the age and mass with their own uncertainty.

3. The interpolation between isochrones involves finding the two closer isochrones to the $(T_{eff}, \log L)$ point (one to each side of the point). The two closest isochrone points would be required for the next step. Let the two closest isochrones have age T_1 and T_2 as shown in fig. 2.22 (In case of mass estimation, the two closest evolutionary tracks have mass M_1 and M_2).
4. Calculating the projection of $(T_{eff}, \log L)$ to the line defined by the closest point of isochrone (and evolutionary track for mass estimation) and either the next point in the curve or the prior one. This distance is used for the next step. Call this distance for each isochrone as D_1 and D_2 .
5. To calculate the age of the source, take the average of T_1 and T_2 weighted by D_1 and D_2 .

$$Age = \frac{(T_1 \cdot D_2 + T_2 \cdot D_1)}{D_1 + D_2} \quad (2.81)$$

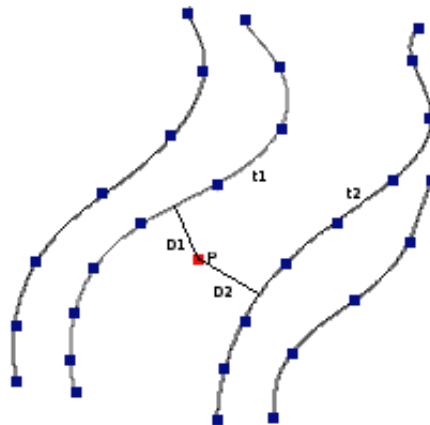


Figure 2.22: Interpolation is used to estimate the minimum distance from point P to get D1 and D2 from either side of the point to the respective isochrone.

6. Doing step (3-5) for each source having 9 grid points explained in step 2. Hence for each source, we will get one age value corresponding to (T_{eff}, LogL) and 8 age values for the rest of the grid. These 8 age values standard deviation will give the sigma value for the age.

Chapter 3

Results

3.1 Selection of Sources for Analysis

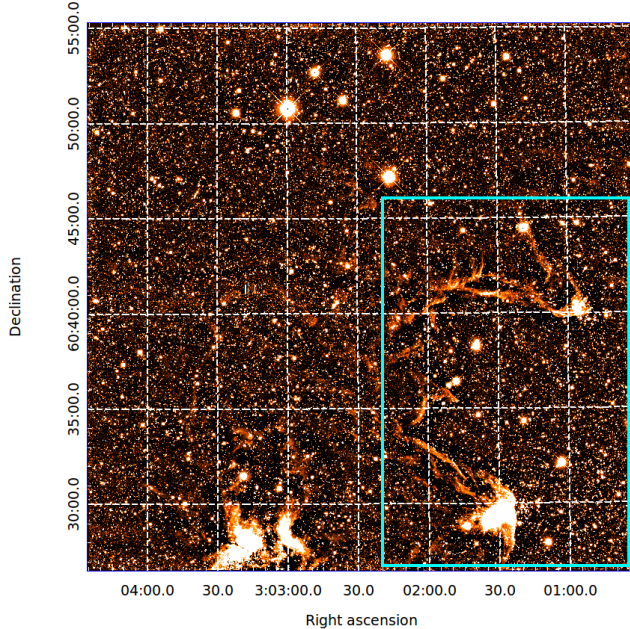


Figure 3.1: NEWFIRM K-band image showing the area of image from where sources are considered for results and analysis.

Results have been studied from the perspective of Bright rimmed clouds (BRCS), BRC 13 and BRC 14. Since both the BRC are spatially located close to each other, hence to study the YSO population, we have kept both regions as one single FOV which is shown in Fig. 3.1. From here onwards, this project utilizes only those sources which are bounded by the box shown in Fig. 3.1. The area of this box is 262.15 arcsec^2 . The size and the

dimensions of this box has been chosen such that it satisfies three conditions, first, it should cover maximum number of available MIR sources, second, it must excludes sources at the edge of NEWFIRM image (see Fig. 2.9) where the S/N ratio is very poor, and last condition, box should cover all number of YSOs identified by previous work.

3.2 Magnitude Distributions and Color-Color-Diagrams

As explained in chapter ??, section ??, the initial data reduction is done and this section deals with the photometric results. As mentioned in section 3.1, the results will be presented only for those sources which falls within the green box shown in fig. 3.1. The magnitude distribution is shown in fig. 3.2 for NIR data and fig. 3.3 for MIR data. Since we this project does not involve any photometry on optical data, hence we have used PS1 PanSTARR data from its archive. The magnitude distribution for this is shown in fig. 3.4.

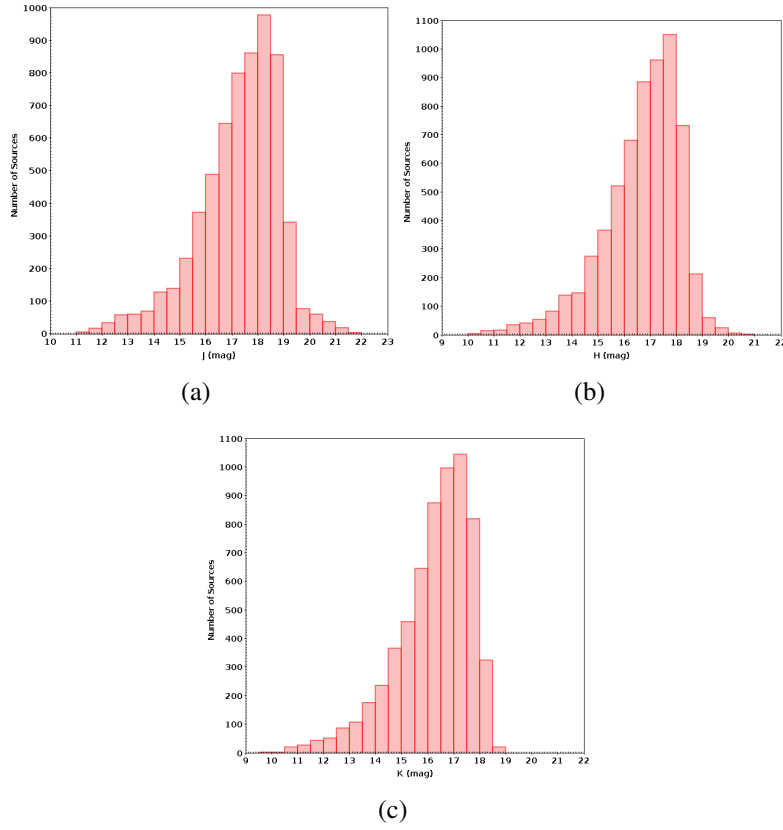


Figure 3.2: Magnitude distribution for the photometric data in case of Near-Infrared. (a) For J band, (b) for H band and (c) for K band. The vertical axis shows the number of sources and horizontal axis shows the magnitude. The distribution is plotted for all those sources which are falling in the box shown in fig. 3.1.

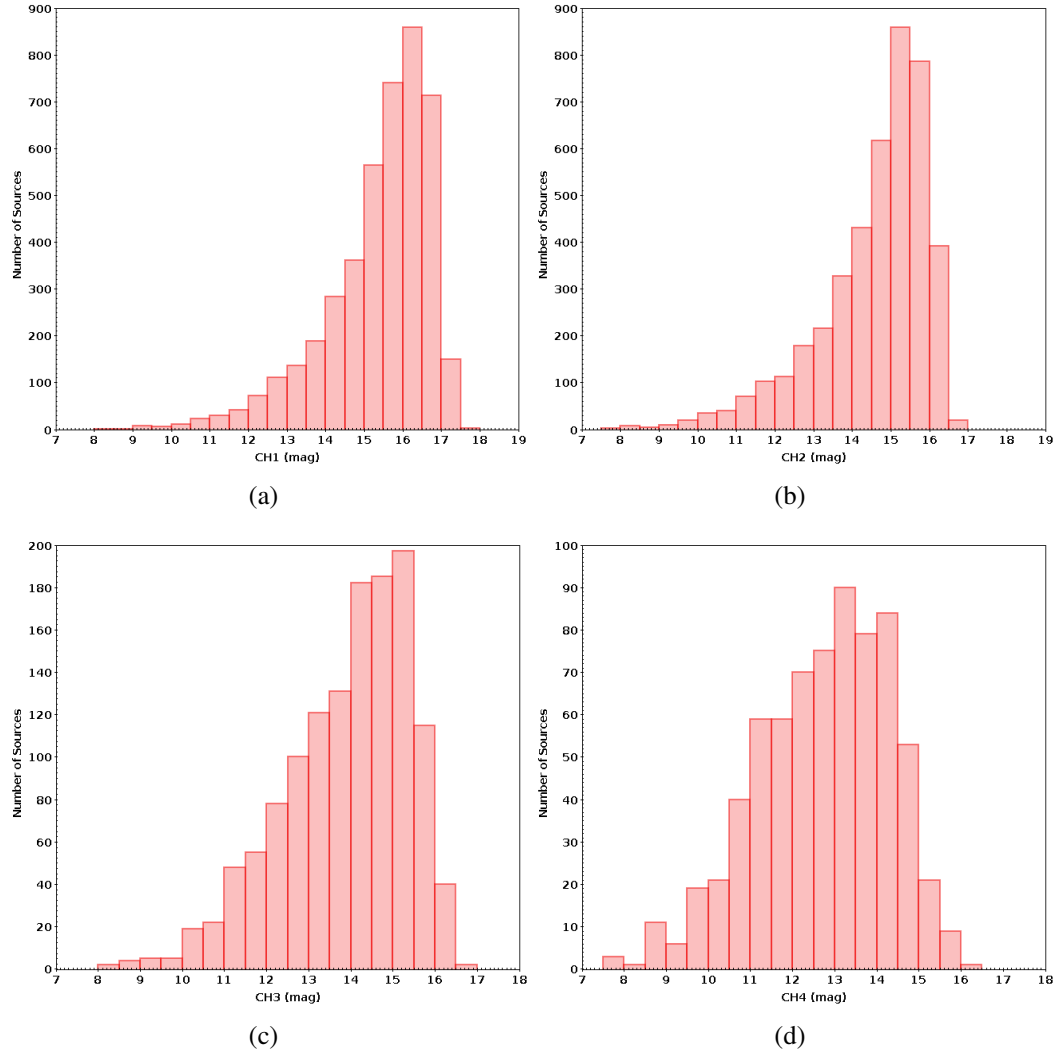


Figure 3.3: Magnitude distribution for the photometric data in case of Mid-Infrared. (a) For CH1 ($3.6 \mu\text{m}$) band, (b) for CH2 ($4.5 \mu\text{m}$) band, (c) for CH3 ($5.8 \mu\text{m}$) band and (d) for CH4 ($8.0 \mu\text{m}$). The vertical axis shows the number of sources and horizontal axis shows the magnitude. The distribution is plotted for all those sources which are falling in the box shown in fig. 3.1.

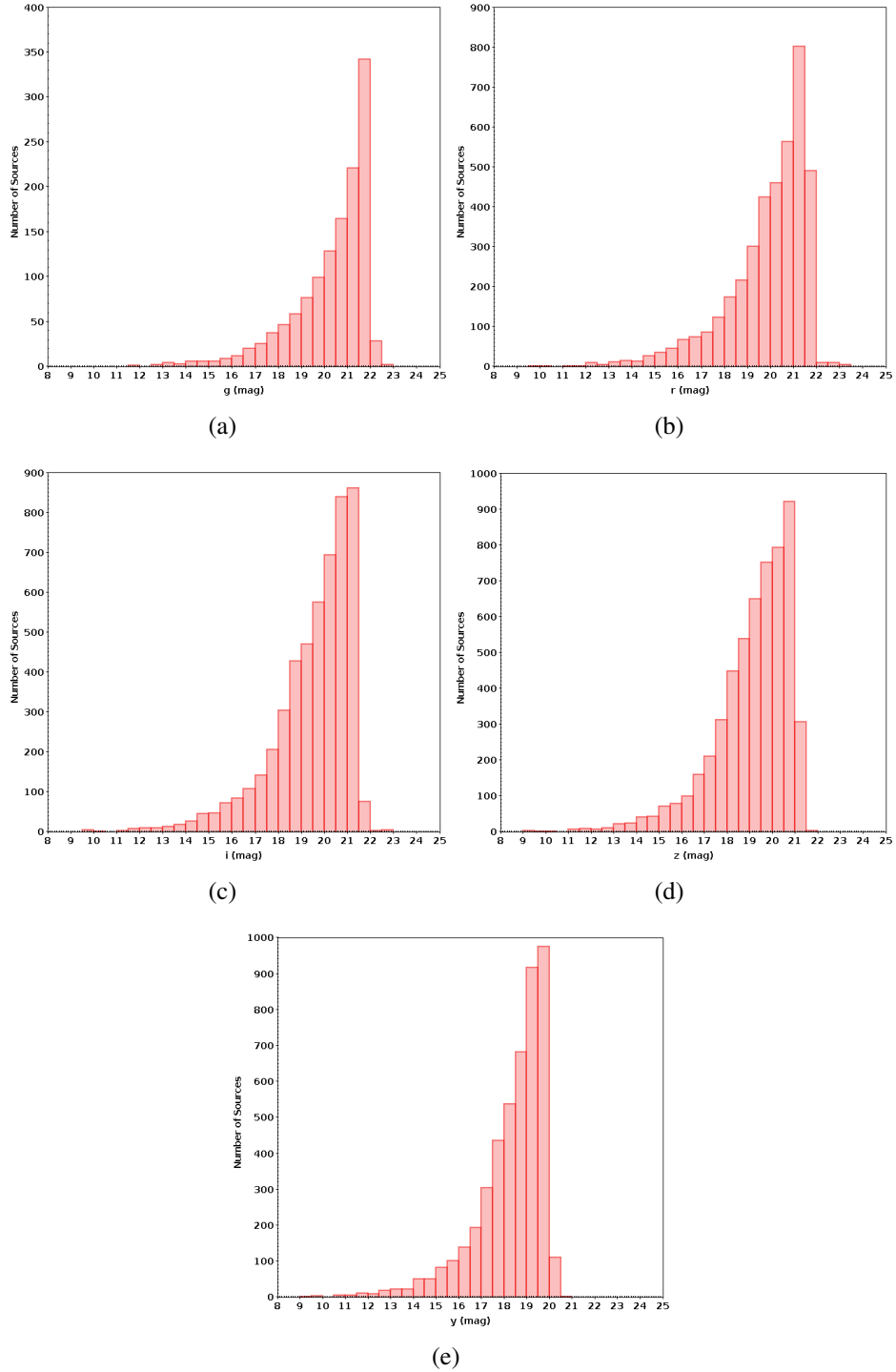


Figure 3.4: Magnitude distribution for the photometric data in case of PanSTARR optical data. (a) For g ($0.49 \mu\text{m}$) band, (b) for r ($0.62 \mu\text{m}$) band, (c) for i ($0.75 \mu\text{m}$) band, (d) for z ($0.87 \mu\text{m}$) band and (e) for y ($0.96 \mu\text{m}$) band. The vertical axis shows the number of sources and horizontal axis shows the magnitude. The distribution is plotted for all those sources which are falling in the box shown in fig. 3.1.

The 90% completeness limit for these distributions is shown in table 3.1. Several combinations of color-color diagrams can be plotted from these data sets. Similarly, various color-magnitude diagrams are also possible. Color-Magnitude diagrams are a very good tool to check the correctness of data and to check the different trends. Some of these color-color diagrams and color-magnitude diagrams are plotted in fig. 3.5 and fig. 3.6

Table 3.1: Completeness limit (90%) for the distributions shown in fig. 3.2, fig. 3.3, fig. 3.4.

S.No.	Filter	λ (μm)	90 % Completeness limit (mag)
1.	g	0.49	21.90
2.	r	0.62	21.65
3.	i	0.75	21.20
4.	z	0.87	20.85
5.	y	0.96	19.80
6.	J	1.00	18.95
7.	H	1.20	18.30
8.	K	2.20	17.82
9.	CH1	3.60	16.80
10.	CH2	4.50	15.85
11.	CH3	5.80	15.20
12.	CH4	8.00	13.71

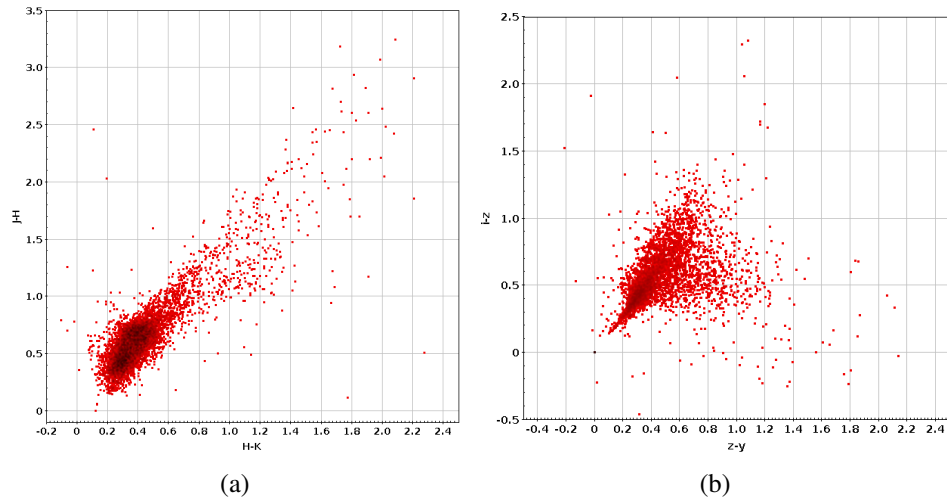


Figure 3.5: Color-Color Plots; (a) (J-H) vs (H-K) Near Infrared color-color plot; (b) (i-z) vs (z-y) Optical color-color plot.

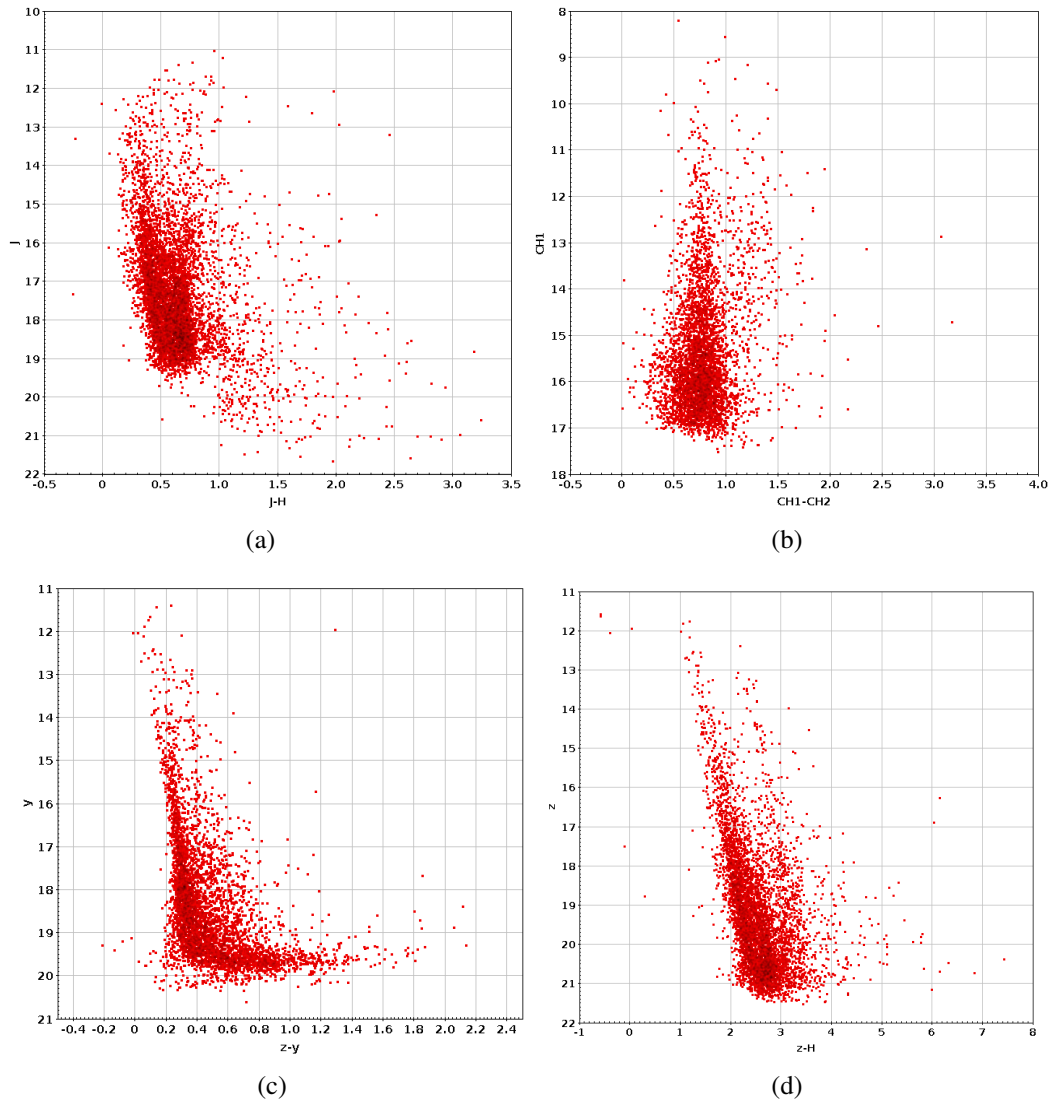


Figure 3.6: Color-Magnitude Plots; (a) J vs (J-H) Color-Magnitude plot; (b) [3.6] vs ([3.6]-[4.5]) Color-Magnitude plot; (c) y vs (z-y) Color-Magnitude plot; (d) z vs (z-H) Color-Magnitude plot;

By looking at the color-magnitude plots, it is very easy to verify several things; like if the data ranges in correct interval, or if the data is showing some wrong sequencing, or if the data is bad or the source is a spurious source. By looking at the CMDs with longer wavelengths like z vs $(z-H)$ shown in fig. 3.6(d); it is prominent to discover two sets of population. One with the $(z-H)$ color ranges between (0-3) and the one with $(z-H)$ color shows >3 . These are the most possible young sources. It will be discussed in detail in sec. ???. These plots can be used to estimate the age and the mass of sources with a suitable isochrone and evolutionary track model after making their distance and extinction corrections.

Whereas the color-color plots like very popular to examine and identify young stellar object YSOs and distinguish them from the evolved sources as explained in section ???. One of the classic example of such approach is by plotting $(J-H)$ vs $(H-K)$ near-infrared plot as shown in fig. 3.5(a). We will use this diagram to identify the field source from the young sources in section ??

3.3 Extinction Estimation

As given in section 2.5, there are various method to probe the extinction. Estimation of extinction is widely done to distinguish and then identify the young stellar objects. The reason why we need to estimate the extinction in this project is because by eliminating the interstellar reddening, we can identify the color excess or reddening shown by the young sources. These young sources happens to show two types of reddening; first because of the presence of dust and gas in interstellar medium between source and observer and second because of the circumstellar disc/envelope present around young sources. Before entering to the zero-age main sequence, the young star accretes the surrounding envelope of gas and dust, which are the main reason behind the circumstellar reddening (see sec. 1.6.1 for more details).

In this section, we have discussed few methods of extinction that we have attempted in this project and we have also discussed that why we have not chosen a particular one to go on with further analysis.

3.3.1 Using Column Density Map

As we have discussed the method of estimating the extinction by making a column density map and then with given values of $N(H_2)$, we can calculate the visible band extinction A_v

(see details in sec. 2.5.1), so we are fortunate enough to get the column density map already prepared and published by Deharveng et al. (2012). They have used Herschel-SPIRE data to make the map which is accounted to show emission from the cold dust which is optically thin. In addition to several assumptions, they have assumed the gas to dust ratio as 100. Estimation of temperature from fitting the modified blackbody allowed the estimation of column density. Also the consideration of opacities at different wavelength is another major assumption taken from Preibisch et al. (1993). The column density map given in Deharveng et al. (2012) is shown in fig. 3.7.

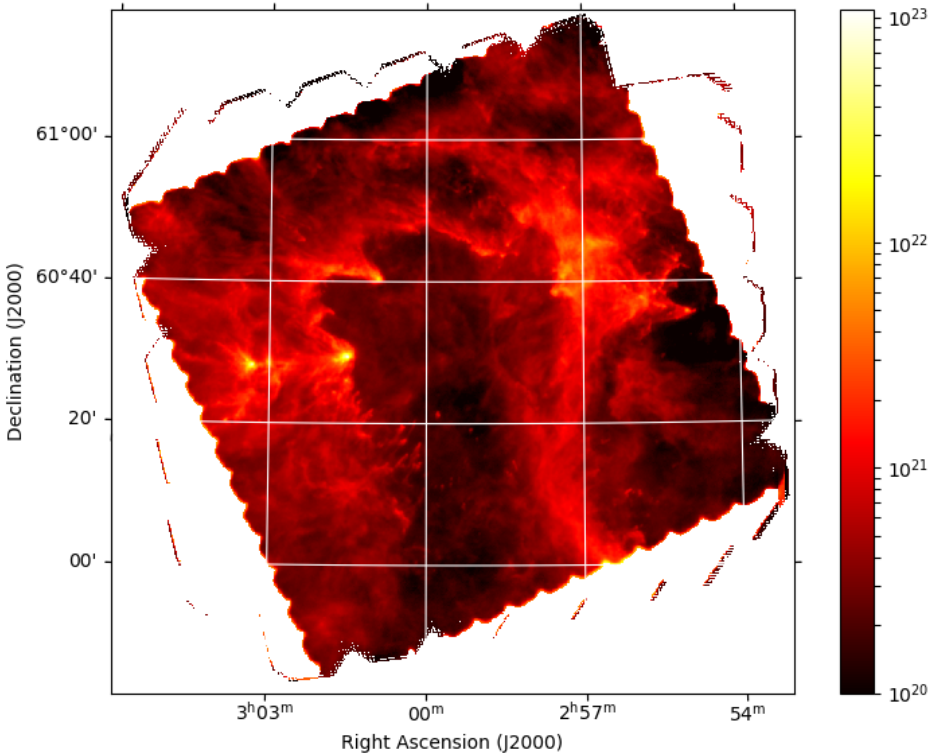


Figure 3.7: Column density map given in Deharveng et al. (2012) showing W5E HII region. Colorbar shows the $N(H_2)$ value in cm^{-2} . Values of column density is estimated using method discussed in section 2.5.1.

Using this map for extinction estimation gives maximum value of visible extinction $A_v = 96$ mag ($\approx N(H_2) = 9.0 \times 10^{22} \text{ cm}^{-2}$) along the BRC 14 region. Similarly they have found maximum value of visible extinction $A_v = 18.20$ mag ($\approx N(H_2) = 9.6 \times 10^{21} \text{ cm}^{-2}$) along the BRC 13 region. The distribution of V-band extinction for all the sources falling within the box shown in fig. 3.1, is shown in fig. 3.8. With another point to remember, that the W5E region is ~ 2.0 Kpc from observer, so the average foreground distribution

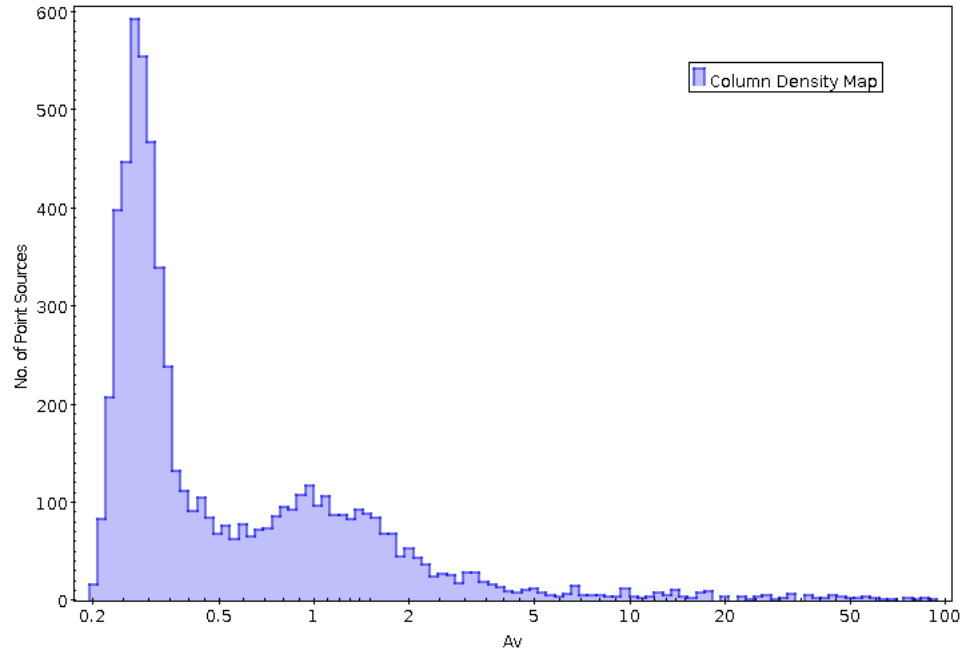


Figure 3.8: Extinction distribution obtained for sources within the box shown in fig. 3.1. Extinction is calculated from column density map given in Deharveng et al. (2012).

that one should expect (For interstellar medium ~ 1.0 mag/Kpc) should be atleast >1.0 mag, however the distribution shown in fig. 3.8 peaks around ~ 0.35 mag. To investigate the extinction values in more detail, we have tried other methods to come up with some more realistic extinction distribution. This study is not considering this extinction values for further analysis.

3.3.2 Using JHKs[3.6][4.5] photometry

In order to estimate more realistic values of extinction, we have attempted the method extinction estimation using five photometric bands i.e. JHKs[3.6][4.5]. This method uses some emperical color cutoffs criteria to get the $[H-K]_o$ i.e. intrinsic color for each of the sources. They have two ways of doing that out, in first case, this quantity is calculated for all sources having J band data available. In second case, $[H-K]_o$ is estimated for all those sources which do not have J band data available but they do have [3.6] and [4.5] IRAC data available. In addition to this, all sources must have H and Ks band data accesible. The complete set of equations involves along with the detailed process is given in section 2.5.3.

Instead of making a extinction map, this methods gives the extinction values for every source. In case of this study, we have also carried out the same procedure as mentioned

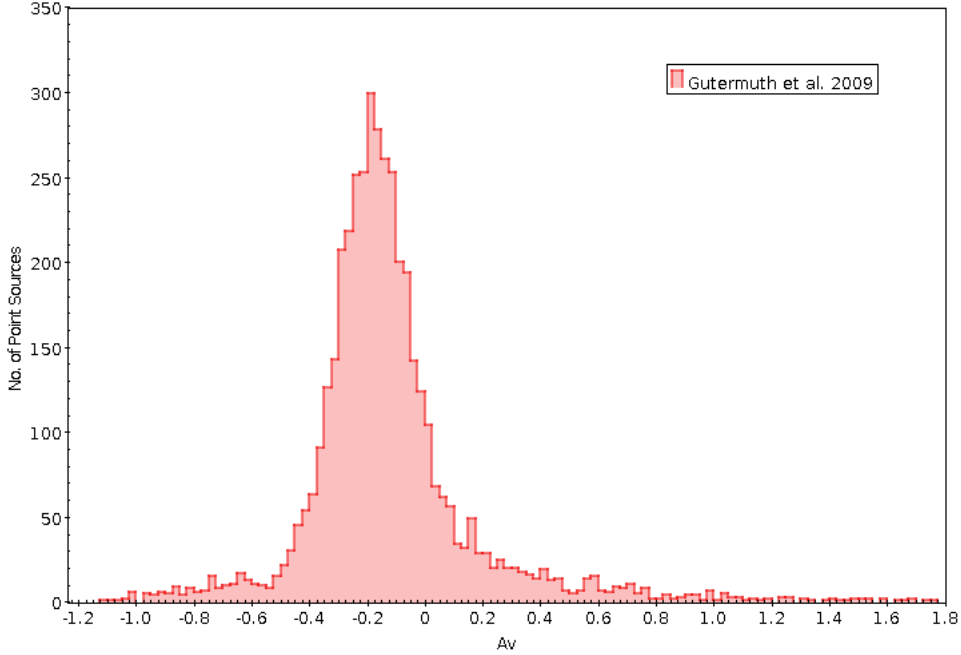


Figure 3.9: Extinction distribution obtained for sources within the box shown in fig. 3.1. Extinction is calculated JHKs[3.6][4.5] photometric data (Gutermuth et al. 2009).

above. The extinction distribution in A_v is shown in fig. 3.9. This plot peaks at ~ 0.18 , the minimum value it gives is around ~ -1.15 , maximum value obtained is ~ 1.80 . Over 65% of the sources shows negative value of extinction. As it is obvious that the negative extinction values are unphysical, hence this study does not use this method for any further analysis.

3.3.3 Using Field Stars

Our extinction map is calculated by dereddening the H - Ks of background stars to the nominal average intrinsic H - Ks of field stars, i.e., $A_K = 1.82 \times [(H-K)_{meas} - (H-K)_{int}]$, where $(H-K)_{int} = 0.2$ is considered the average intrinsic color of field stars. The extinction map is shown in fig. 3.11. The FOV of the map is 315 arcmin^2 and resolution is 1 arcmin. Following are the steps taken to create the map;

1. Isolate the field stars from excess sources using $(J-H)$ vs $(H-K)$ plot which is shown in fig. 3.10.
2. For these field sources extinctions is calculated as $A_K = 1.82 \times [(H-K)_m - (H-K)_{int}]$ Where, $(H-K)_{int} = 0.2$ for field sources.
3. To make the map, each source is convolved with Gaussian Kernel.

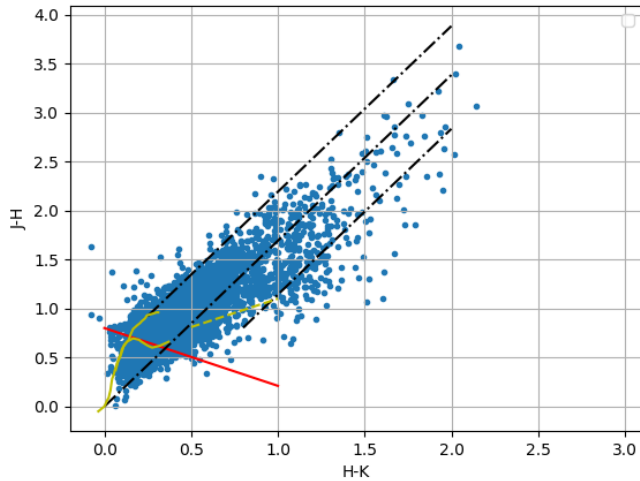


Figure 3.10: Color-color diagram (J-H)/(H-K) for W5E HII from area shown in Fig. 3.1. The Continuous curves shows the intrinsic locus of Main sequence (below) and Giants(above) (Bessell & Brett 1988). The dashed line represents the locus of intrinsic color of classical T-Tauri (Meyer et al. 1997). The dashed-dotted lines are reddening vectors from (Cohen et al. 1981). All the sources lies leftward to the middle reddening vectors are used as field stars to calculate extinction based on intrinsic color of field stars. The extinction map built using that is shown in fig. 3.11.

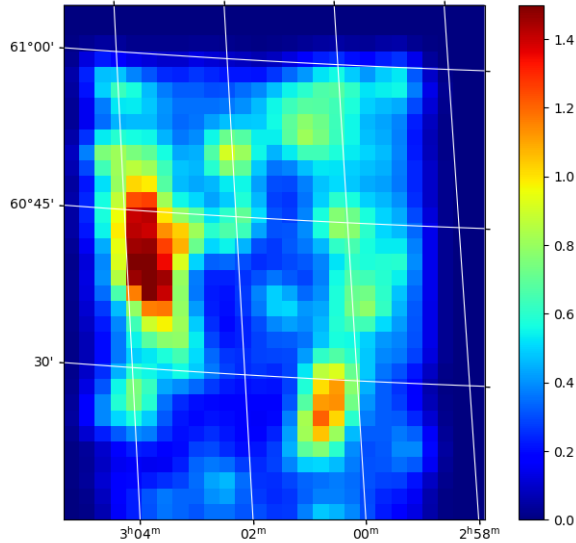


Figure 3.11: Extinction map of W5E HII region made by using the background field stars. The colorbar shows extinction in K-band i.e. A_K . The map has 315 arcmin^2 field of view and resolution if 1 arcmin.

The map is shown in fig. 3.11, it has FOV of 315 arcmin² and has resolution of 1 arcmin. The maximum and minimum values of extinction estimated from this map are 0.02 mag and 1.5 mag in K band respectively. The gaussian used here has a thickness approximatly equal to its resolution. The resolution of this map is qualified to be called as poor resolution as the number of field sources close to the two BRCs are very low. In order to increase the resolution, it is required to use narrow gaussian kernel, which infact turns to give either blanck pixels or zero pixel values near the head of BRCs. Since the BRCs are the main target site for this project and the under-abundense of these field stars close to the BRCs yield the underestimated value of extinction, hence this is obligatiry to move on to the next method of extinction estimation.

3.3.4 Using PNICER

PNICER is a machine-learning based algorithm which uses JHKs data and their measured color with a given extinction law to get the extinction value A_v . It requires two different regions, namely science field and control field. The science field is the target region and the control field is a region with nearby un-extinct regions (or regions with minimum extinction). This is used to compare the two region's extinction and then using the machine learning algorithm, it makes a map which gives AK values (Meingast et al. 2017).

The routine applies machine learning techniques to photometric measurements of extincted sources, in combination with reddening-free control field data, to determine the extinction along the line of sight. In particular, PNICER fits Gaussian Mixture Models along the extinction vector in arbitrary numbers of dimensions to derive probability densities describing the extinction for each source. Section 2.5.2 explaines the entire procedure in detail.

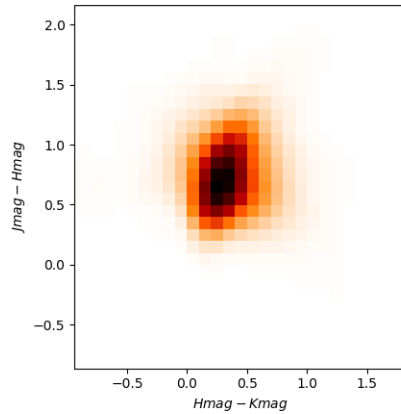


Figure 3.12: Color-Color plot produced by PNICER (J-H) vs (H-K). The data is taken from 2MASS point source catalog in JHK band with read flag as '222'.

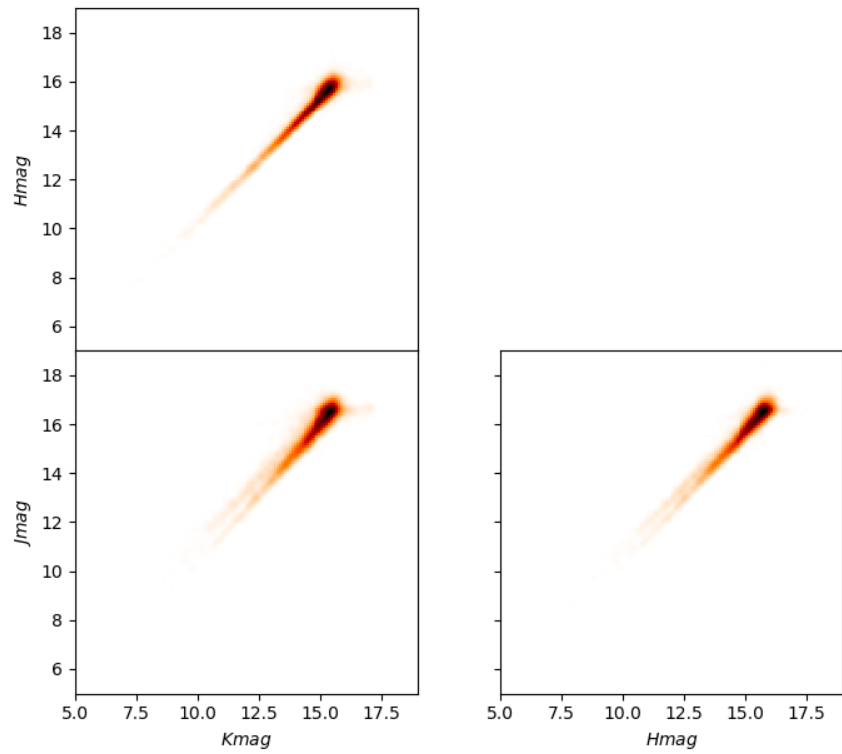


Figure 3.13: Plot generated by the PNICER showing the density distribution for the feature combinations. This plot is generated for W5E HII region in order to make the extinction map of the same region for all three filter combination.

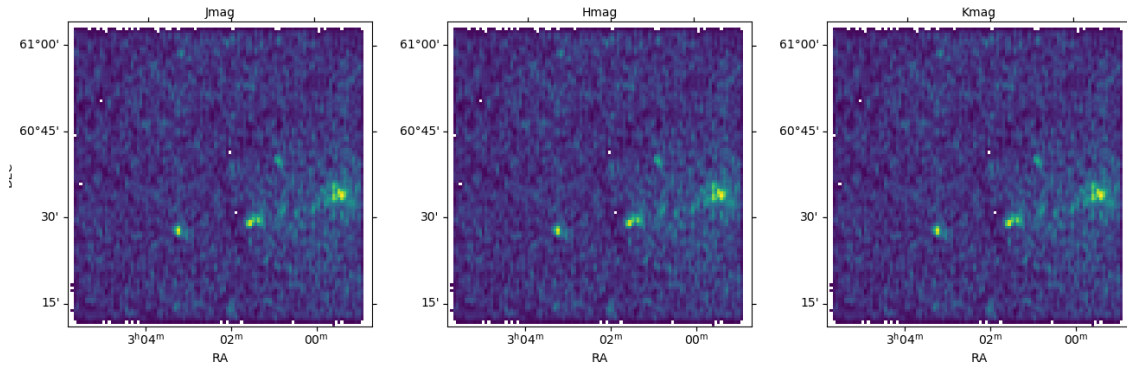


Figure 3.14: Plot generated by the PNICER showing the kernel density distribution map for the feature combinations, Jmag (left), Hmag (middle) and Kmag (right). This plot is generated for W5E HII region.

The results PNICER draws before making the extinction map are the density distribution for all combination of magnitudes as shown in fig. 3.13 and its own color-color (J-H) vs (H-K) plot as shown in fig. 3.12. This two plots uses the 2MASS point source catalog data instead of NEWFIRM data (NEWFIRM is more deeper survey than 2MASS, hence fig. 3.12 and fig. 3.10). The other plot it generates is the kernel density distribution map for the feature combinations for all three bands.

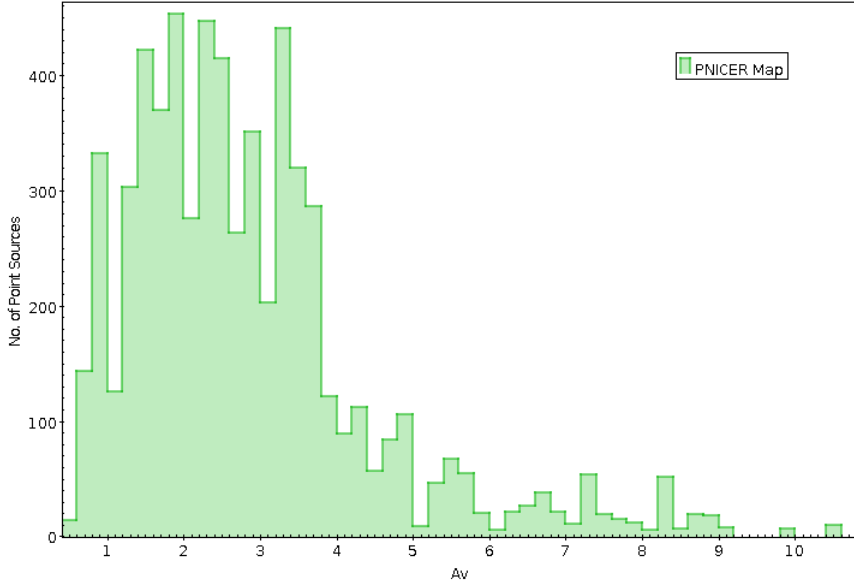


Figure 3.15: Histogram distribution of extinction values in V-band (A_v) for all those sources falling in green box in fig. 3.1. The extinction values are taken from PNICER map shown in fig. 3.16.

The extinction map is shown in fig. 3.16. The map shown has field of view of 0.5 deg^2 with the resolution of 0.5 arcsec. The colorbar shown is giving the extinction value in V-band, i.e. A_v . The minimum value estimated here is about 0.3 mag and the maximum value estimated is about 10.60 mag in V-band. This distribution peaks around 2.5 mag, which is reliable for a source at a distance of 1.8-2.3 Kpc. The distribution is shown in fig. 3.15. This project makes use of this extinction map for further analysis.

3.3.4.1 Extinction Uncertainty Map

In order to improve the extinction values reliability, we have carried out the task of making the uncertainty map from the PNICER map. The uncertainty values is used as the standard deviation of the extinction value. Following are the steps involved in making the uncertainty map;

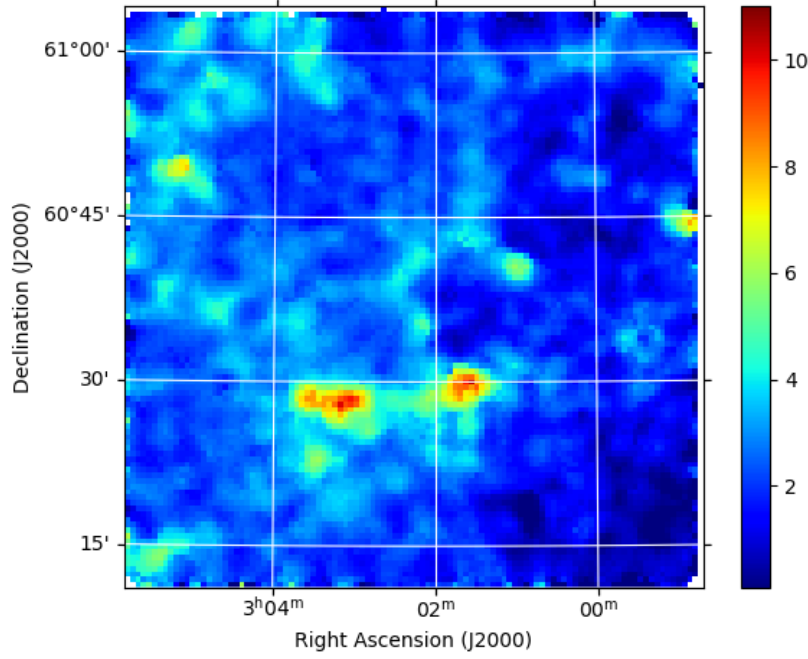


Figure 3.16: Extinction map generated by PNICER for W5E HII region. The colorbar shows the extinction values in V-band (A_v). The map shown has field of view of 0.5 deg^2 with the resolution of 0.5 arcsec.

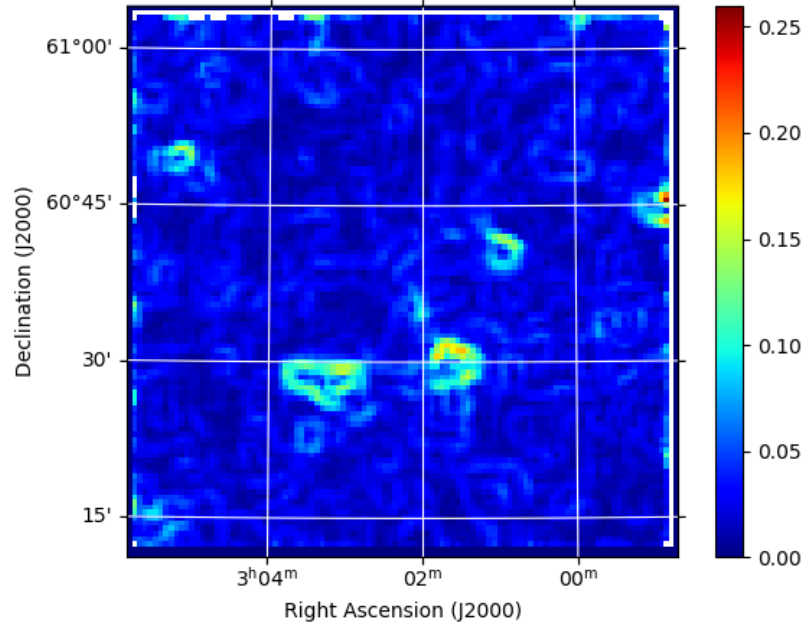


Figure 3.17: Extinction uncertainty map generated by PNICER for W5E HII region. The colorbar shows the extinction uncertainty values in V-band (σA_v) which is calculated from PNICER map. The map shown has field of view of 0.5 deg^2 with the resolution of 0.5 arcsec.

1. From the map generated by PNICER map, for each pixel, the 3×3 grid is selected. These nine values are used to make the uncertainty map. For every (i,j) pixel, there would be (i-1,j), (i+1, j), (i-1, j-1), (i+1, j-1)....etc. pixel values.
2. Calculate the standard deviation of these nine values, let it be $\sigma_{i,j}$. For all values of (i,j), calculate the value of $\sigma_{i,j}$, except for the outer edge of the PNICER map. Hence for $(i \times j)$ pixels, it will give the standard deviation $(i \times j - 2(i+j))$ values.
3. Using all the values of standard deviation calculated from step 2, make a map with convoluting each pixel value such that the uncertainty map should have the same resolution as the PNICER map.

Extinction uncertainty map made by the above procedure is shown in fig. 3.17, the map shown has field of view of 0.5 deg^2 with the resolution of 0.5 arcsec which is same as the PNICER map. The minimum value of uncertainty is 0.03 mag and maximum value is 0.265 mag. The colorbar shows the uncertainty in fig. 3.17. These uncertainty values along with the extinction values is used for rest of the analysis.

3.4 YSO identification

Infrared (IR) data are a very useful tool for detecting YSOs and studying their nature in clusters/SFRs. YSOs exhibit strong IR excess due to the presence of circumstellar discs and envelopes, hence they can be separated out using the NIR and MIR observations.

We used IRAC detections in all [3.6], [4.5], [5.8] and [8.0] bands with an uncertainty less than 0.2 mag to identify Class I and Class II sources associated with the region following the schemes described in detail by Gutermuth et al. (2005, 2009) (see appendix A, phase 1). Various non-stellar contaminations, which include emission from features dominated by polycyclic aromatic hydrocarbons (PAHs), likely star-forming galaxies and weak-line active galactic nuclei, are eliminated using these schemes.

These criteria are given in section 2.6. Fig. 3.18 shows the color-color diagram [Ks] - [3.6] vs [3.6]-[4.5] showing the class II (green) and class I (blue) sources with field/class III sources (red). The numbers of YSOs identified based on this are; 195 class II and 14 class I sources for the BRC 13 and BRC 14 region combined. The black line shown in fig. 3.18 distinguishes class I and class II sources. These lines are drawn considering the average value of sigma for all source, for more detail refer to section 2.6.2.

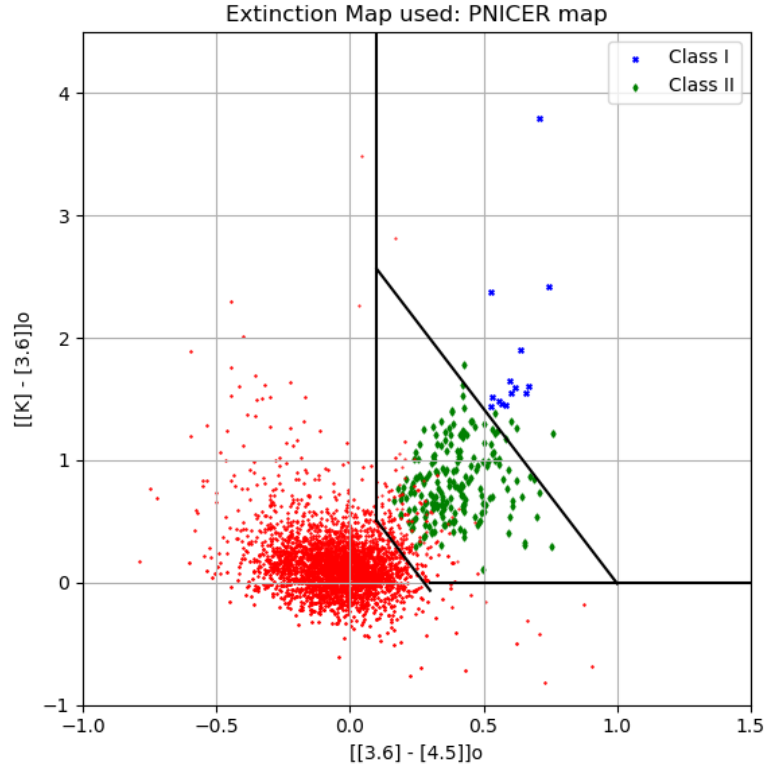


Figure 3.18: color-color diagram $[K_s] - [3.6]$ vs $[3.6] - [4.5]$ showing the class II (green) and class I (blue) sources with field/class III sources (red). The color cutoff are given in detail in section 2.6. The identification scheme is taken from Gutermuth et al. (2005, 2009).

The constraint applied in eq. 2.56 and eq. 2.58, is actually decided based on the depth of MIR survey data. These two conditions basically eliminates faint extragalactic contaminants. To take the value for this condition, we have used the photometric magnitude distribution as shown in fig. 3.3. The 90% completeness factor for $[3.6]$ is 16.80 mag (see table 3.1). For eliminating the faint extragalactic sources, the criteria for protostars class I source uses 90% completeness limit i.e. 16.80 mag and in case of class II source, it is relaxed by 0.5 mag and taken as 16.30 mag.

3.5 SED Modelling and HR diagram

All the source identified as young stellar object in section 3.4, are modelled using the online spectral energy analyzer VOSA. The model choosen for it is BT-Settl CIFIST. The parameter grid for this model is given in table 2.12. We have utilized the entire grid space

offered by the model. For extinction, we have used the values from PNICER map fig. 3.16 (sec. 3.3.4) and its standard deviation from the the map shown in fig. 3.17 (sec. 3.3.4.1). The distance taken for all the sources are 2100 ± 300 pc. A user made input file is uploaded to VOSA for the analysis. A sample VOSA input file is shown in table 2.13.

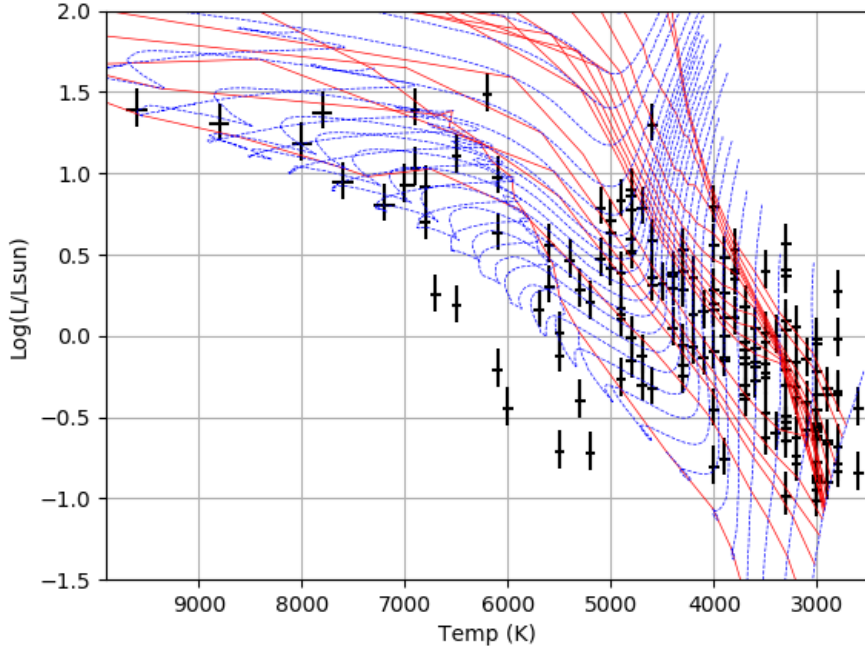


Figure 3.19: The HR diagram plot for the source (in black) identified in section 3.4. The horizontal axis is temperature in K and vertical axis given bolometric luminosity (L/L_{\odot}) in logscale. The red lines are the isochrones of 0.007 Myr (right most) till 10 Myr (left most). The blue dotted curves are the evolutionary tracks of mass $0.1 M_{\odot}$ (very bottom) to $30 M_{\odot}$ (very top). The isochrones and evolutionary tracks are taken from Siess et al. (2000).

The result of the SED modelling gives the temperature (T_{eff}) and luminosity (L/L_{\odot}) for all the sources. The HR diagram can be plotted using these results as shown in fig. 3.19. The plot shows the luminosity and temperature for all the sources along with their uncertainty as error bar. To estimate more physical parameters like age and mass, we have opted the procedure given in section 2.7.2.5. As explained there, to estimate the age, we need the age isochrones and to estimate the mass, we need the evolutionary tracks. For this purpose, we have used the age isochrones and evolutionary tracks from Siess et al. (2000). The age isochrones ranges from 0.07 Myr to 10 Myr and evolutionary track ranges from $0.1 M_{\odot}$ to $30 M_{\odot}$. With this estimation, the mass distribution obtained is shown in fig. 3.20. The minimum mass and maximum mass obtained are $0.13 M_{\odot}$ and $6.88 M_{\odot}$ respectively.

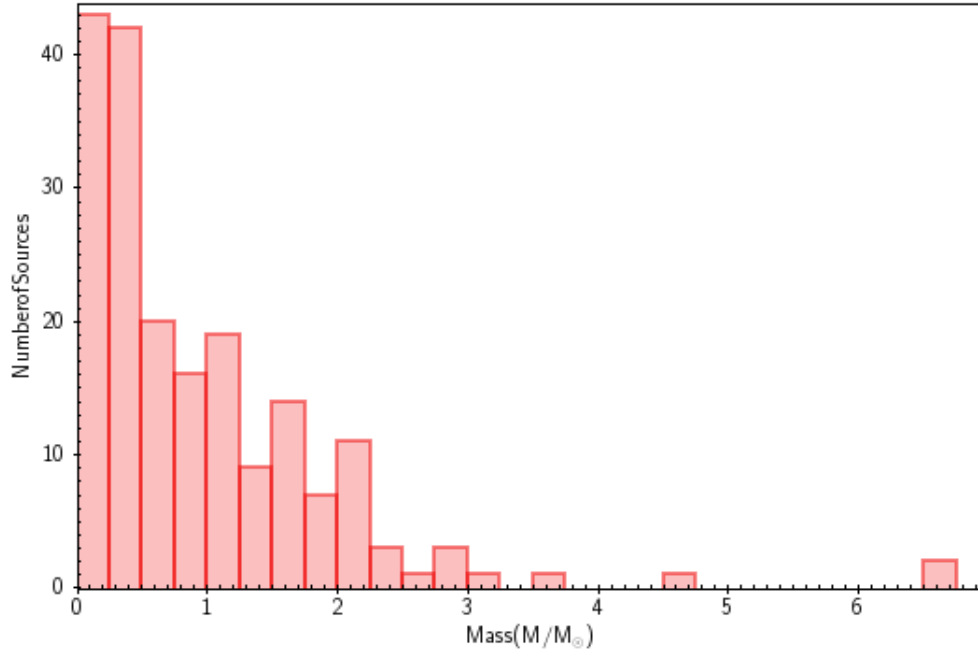


Figure 3.20: Mass distribution for all the sources identified in section 3.4 and modelled by VOSA.

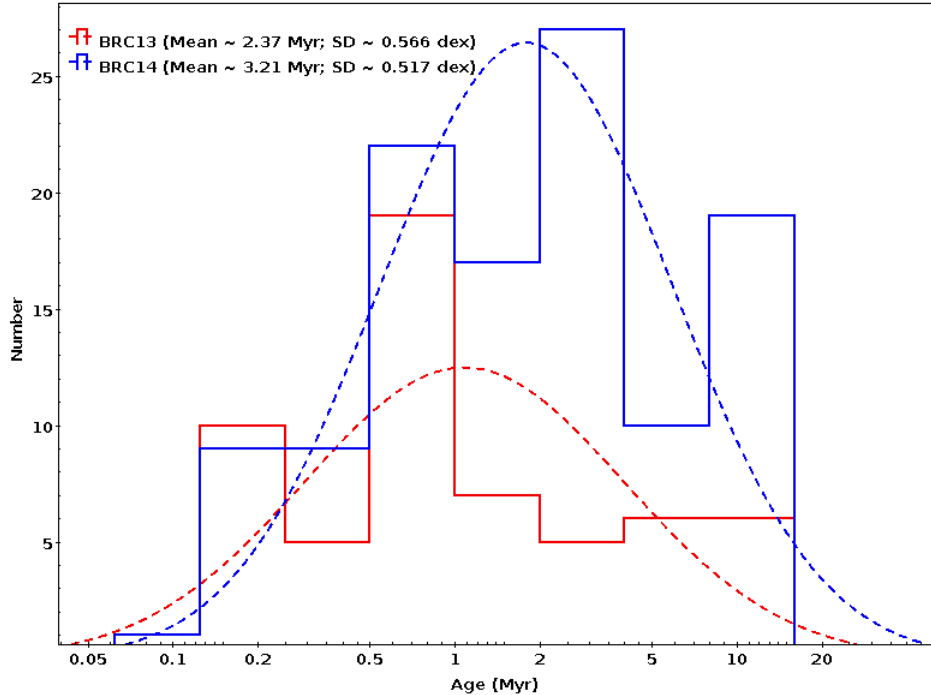


Figure 3.21: Age distribution for all the sources identified in section 3.4 and modelled by VOSA. Distribution shown for BRC 13 (in red) and BRC 14 (in blue), histograms are fitted with gaussian (dotted curves) to calculate the mean age for the two BRCs.

The age distribution thus obtained is shown in fig. 3.21. Here the distribution is plotted for both the BRCs separately (BRC13 in red and BRC14 in blue). The distribution has horizontal axis as age in Myr which is in logscale. The distribution is fitted with the gaussian to estimate the mean age for both the BRCs. The mean age thus obtained for BRC 13 is 2.37 ± 1.76 Myr. The mean age for BRC 14 is calculated as 3.21 ± 1.67 Myr.

Chapter 4

Conclusions and Future Work

Following are the main that we will take in order to proceed further in this project in coming phase;

- Till now this project has covered two BRCs in W5E H II region. In order to do a statistical analysis considering the star formation rates and efficiency, this project has to look for more BRCs in W5 H II complex.
- Along with these two BRCs, W3, W4 and W5 cloud complexes are sites where more BRCs are found. As future work, this project will try to cover as many BRCs as possible and then we will attempt to make a statistical analysis on star formation rates and efficiency.
- In case on BRC 13 and BRC 14, the project is able to cover till making HR diagram of the site, however there are few population of premain sequence sources which lie outside the pre-main sequence isochrones, this can be because to poor photometric data point or poor statistics.
- As future work, the fitting statistics will be improved by looking the individual sources which are lying outside the isochrones, there photometry data and spatial location in NIR, MIR images.
- Another way to improve the fitting accuracy is by narrowing the initial conditions like reddening, metalicity and distance constraint.
- Reddening can be estimated by making reddening/extinction maps along the line of site of region. We will make these maps based on the reddening obtained from the JHK CC diagram, after tracing individual data point to the tip of the main sequence locus.

- After getting the extinction of individual sources, we will proceed to make map out of that by convolving that with gaussian or square cell approach.
- As the accurate age and mass estimation will complete, the project will look for the calculate of initial mass function (IMF) and age distribution.
- To obtain the star formation rate (SFR) and efficiency (SFE), cloud parameters will be required hence we will compute the cloud mass, column density etc.
- Since the calculations for SFR and SFE for BRC 13 and 14 is still ongoing, nevertheless after calculating the SFR and SFE, we will proceed to other BRCs.
- The data reduction of some more BRCs are still going on in parallel with the analysis of part of BRC 13 and 14, however we are not including those data reduction in this thesis, since we do not have got any physical parameters (age, mass etc.) out of those BRCs.

Bibliography

- Adams, F. C., Lada, C. J., & Shu, F. H. 1987, *The Astrophysical Journal*, 312, 788
- Allard, F., Homeier, D., Freytag, B., & Sharp, C. 2012, *European Astronomical Society Publications Series*, 57, 3
- Aspin, C., Sandell, G., & Russell, A. 1994, *Astronomy and Astrophysics Supplement Series*, 106, 165
- Axford, W. I. 1964, *The Astrophysical Journal*, 140, 112
- Bally, J., Devine, D., & Reipurth, B. 1996, *The Astrophysical Journal Letters*, 473, L49
- Bally, J., Reipurth, B., Lada, C. J., & Billawala, Y. 1999, *The Astronomical Journal*, 117, 410
- Bally, J., Walawender, J., Johnstone, D., et al. 2008, *Reipurth* (San Francisco, CA: ASP), 459
- Baraffe, I., Homeier, D., Allard, F., & Chabrier, G. 2015, *Astronomy & Astrophysics*, 577, A42
- Bertoldi, F. 1989, *The Astrophysical Journal*, 346, 735
- Bertoldi, F. & McKee, C. F. 1990, *The Astrophysical Journal*, 354, 529
- Bessell, M. & Brett, J. 1988, *Publications of the Astronomical Society of the Pacific*, 100, 1134
- Bisbas, T. G., Wünsch, R., Whitworth, A. P., Hubber, D. A., & Walch, S. 2011, *The Astrophysical Journal*, 736, 142
- Blitz, L., Levy, E., & Lunine, J. 1993, *UofAP*, Tuscon

- Bok, B. J. & Reilly, E. F. 1947, *The Astrophysical Journal*, 105, 255
- Carroll, B. W. & Ostlie, D. A. 2017, *An introduction to modern astrophysics* (Cambridge University Press)
- Castor, J., McCray, R., & Weaver, R. 1975a, *The Astrophysical Journal*, 200, L107
- Castor, J. I., Abbott, D. C., & Klein, R. I. 1975b, *The Astrophysical Journal*, 195, 157
- Chauhan, N., Pandey, A., Ogura, K., et al. 2011, *Monthly Notices of the Royal Astronomical Society*, 415, 1202
- Chauhan, N., Pandey, A., Ogura, K., et al. 2009, *Monthly Notices of the Royal Astronomical Society*, 396, 964
- Cohen, J. G., Frogel, J. A., Persson, S., & Elias, J. H. 1981, *Astrophysical Journal*, 249, 481
- Dale, J., Ercolano, B., & Bonnell, I. 2012, *Monthly Notices of the Royal Astronomical Society*, 424, 377
- Dale, J., Ercolano, B., & Bonnell, I. 2013, *Monthly Notices of the Royal Astronomical Society*, 430, 234
- Dale, J. E., Bonnell, I., & Whitworth, A. 2007, *Monthly Notices of the Royal Astronomical Society*, 375, 1291
- Davis, L. E. et al. 1994, *IRAF Programming Group*, NOAO, Tucson
- Deharveng, L., Schuller, F., Anderson, L., et al. 2010, *Astronomy & Astrophysics*, 523, A6
- Deharveng, L., Zavagno, A., Anderson, L., et al. 2012, *Astronomy & Astrophysics*, 546, A74
- Dyson, J. E. & Williams, D. A. 1997, *The physics of the interstellar medium* (CRC Press)
- Elmegreen, B. G. & Lada, C. J. 1977, *The Astrophysical Journal*, 214, 725
- Evans II, N. J., Dunham, M. M., Jørgensen, J. K., et al. 2009, *The Astrophysical Journal Supplement Series*, 181, 321
- Fall, S. M., Krumholz, M. R., & Matzner, C. D. 2010, *The Astrophysical Journal Letters*, 710, L142

- Fischera, J. & Martin, P. G. 2012, *Astronomy & Astrophysics*, 547, A86
- Flaherty, K. M., Pipher, J., Megeath, S., et al. 2007, *The Astrophysical Journal*, 663, 1069
- Franco, J., Tenorio-Tagle, G., & Bodenheimer, P. 1990, *The Astrophysical Journal*, 349, 126
- Fukuda, N., Hanawa, T., & Sugitani, K. 2002, *The Astrophysical Journal Letters*, 568, L127
- Greene, T. P. & Lada, C. J. 1996, *The Astronomical Journal*, 112, 2184
- Gritschneider, M., Naab, T., Walch, S., Burkert, A., & Heitsch, F. 2009, *The Astrophysical Journal Letters*, 694, L26
- Gutermuth, R., Megeath, S., Myers, P., et al. 2009, *The Astrophysical Journal Supplement Series*, 184, 18
- Gutermuth, R. A., Megeath, S. T., Pipher, J. L., et al. 2005, *The Astrophysical Journal*, 632, 397
- Henney, W. J., Arthur, S. J., De Colle, F., & Mellema, G. 2009, *Monthly Notices of the Royal Astronomical Society*, 398, 157
- Hildebrand, R. H. 1983
- Hosokawa, T. & Omukai, K. 2009, *The Astrophysical Journal*, 691, 823
- Howell, S. B. 1989, *Publications of the Astronomical Society of the Pacific*, 101, 616
- Indebetouw, R. 2015, *IAU General Assembly*, 22
- Kahn, F. 1958, *Reviews of Modern Physics*, 30, 1058
- Kahn, F. 1969, *Physica*, 41, 172
- Kahn, F. et al. 1954, *Bulletin of the Astronomical Institutes of the Netherlands*, 12, 187
- Karr, J. & Martin, P. 2003, *The Astrophysical Journal*, 595, 900
- Kessel-Deynet, O. & Burkert, A. 2003, *Monthly Notices of the Royal Astronomical Society*, 338, 545

- Knee, L. & Sandell, G. 2000, *Astronomy and Astrophysics*, 361, 671
- Koenig, X., Leisawitz, D., Benford, D., et al. 2011, *The Astrophysical Journal*, 744, 130
- Koenig, X. P., Allen, L. E., Gutermuth, R. A., et al. 2008, *The Astrophysical Journal*, 688, 1142
- Krumholz, M. R., Bate, M. R., Arce, H. G., et al. 2014, *Protostars and Planets VI*, 243
- Krumholz, M. R. & Matzner, C. D. 2009, *The Astrophysical Journal*, 703, 1352
- Krumholz, M. R., Matzner, C. D., & McKee, C. F. 2006, *The Astrophysical Journal*, 653, 361
- Kudritzki, R., Pauldrach, A., Puls, J., & Abbott, D. 1989, *Astronomy and Astrophysics*, 219, 205
- Kudritzki, R., Puls, J., Lennon, D., et al. 1999, arXiv preprint astro-ph/9910449
- Lada, C. J. 2006, *The Astrophysical Journal Letters*, 640, L63
- Lada, C. J. & Lada, E. A. 2003, *Annual Review of Astronomy and Astrophysics*, 41, 57
- Lefloch, B. & Lazareff, B. 1994, *Astronomy and Astrophysics*, 289, 559
- Lefloch, B. & Lazareff, B. 1995, *Astronomy and Astrophysics*, 301, 522
- Lopez, L. A., Krumholz, M. R., Bolatto, A. D., PROCHASkA, J. X., & Ramirez-Ruiz, E. 2011, *The Astrophysical Journal*, 731, 91
- Lopez, L. A., Krumholz, M. R., Bolatto, A. D., et al. 2014, *The Astrophysical Journal*, 795, 121
- Martin, P. G., Roy, A., Bontemps, S., et al. 2012, *The Astrophysical Journal*, 751, 28
- McKee, C. F. 1989, *The Astrophysical Journal*, 345, 782
- Meingast, S., Lombardi, M., & Alves, J. 2017, *Astronomy & Astrophysics*, 601, A137
- Meyer, M. R., Calvet, N., & Hillenbrand, L. A. 1997, *The Astronomical Journal*, 114, 288
- Miao, J., White, G. J., Nelson, R., Thompson, M., & Morgan, L. 2006, *Monthly Notices of the Royal Astronomical Society*, 369, 143

- Miao, J., White, G. J., Thompson, M., & Nelson, R. P. 2009, The Astrophysical Journal, 692, 382
- Newman, R. & Axford, W. 1968, The Astrophysical Journal, 153, 595
- Norman, C. & Silk, J. 1980, The Astrophysical Journal, 238, 158
- Ogura, K. 2010, in Astronomical Society of India Conference Series, Vol. 1
- Ogura, K., Chauhan, N., Pandey, A. K., et al. 2007, Publications of the Astronomical Society of Japan, 59, 199
- Ojha, D. K., Tamura, M., Nakajima, Y., et al. 2004a, The Astrophysical Journal, 608, 797
- Ojha, D. K., Tamura, M., Nakajima, Y., et al. 2004b, The Astrophysical Journal, 616, 1042
- Oort, J. H., Spitzer, L. J., et al. 1955, Astrophysical Journal, 121
- Osterbrock, D. 1974, Institute for Advanced Studies, and National Science Foundation. San Francisco, WH Freeman and Co, 263, 224
- Osterbrock, D. E. & Ferland, G. J. 2006, Astrophysics Of Gas Nebulae and Active Galactic Nuclei (University science books)
- Pandey, A., Sharma, S., Ogura, K., et al. 2008, Monthly Notices of the Royal Astronomical Society, 383, 1241
- Panwar, N., Chen, W., Pandey, A., et al. 2014, Monthly Notices of the Royal Astronomical Society, 443, 1614
- Pauldrach, A., Puls, J., & Kudritzki, R. 1986, Astronomy and Astrophysics, 164, 86
- Pavlakis, K., Williams, R., Dyson, J., Falle, S., & Hartquist, T. 2001, Astronomy & Astrophysics, 369, 263
- Pellegrini, E. W., Baldwin, J. A., & Ferland, G. J. 2011, The Astrophysical Journal, 738, 34
- Pottasch, S. et al. 1956, Bulletin of the Astronomical Institutes of the Netherlands, 13, 77
- Pottasch, S. et al. 1958, Bulletin of the Astronomical Institutes of the Netherlands, 14, 29

Pottasch, S. R. 1958, in Symposium-International Astronomical Union, Vol. 8, Cambridge University Press, 1053–1058

Preibisch, T., Ossenkopf, V., Yorke, H., & Henning, T. 1993, Astronomy and Astrophysics, 279, 577

Prialnik, D. 2000, An Introduction to the Theory of Stellar Structure and Evolution

Rieke, G. & Lebofsky, M. 1985, The Astrophysical Journal, 288, 618

Robitaille, T. P., Whitney, B. A., Indebetouw, R., & Wood, K. 2007, The Astrophysical Journal Supplement Series, 169, 328

Roy, A., Martin, P. G., Polychroni, D., et al. 2013, The Astrophysical Journal, 763, 55

Samal, M., Zavagno, A., Deharveng, L., et al. 2014, Astronomy & Astrophysics, 566, A122

Sandell, G. & Knee, L. 2001, in Science with the Atacama Large Millimeter Array, Vol. 235, 154

Sandford, M., Whitaker, R., & Klein, R. 1982, The Astrophysical Journal, 260, 183

Scoville, N., Polletta, M., Ewald, S., et al. 2001, The Astronomical Journal, 122, 3017

Sharma, S., Pandey, A., Borissova, J., et al. 2016, The Astronomical Journal, 151, 126

Siess, L., Dufour, E., & Forestini, M. 2000, arXiv preprint astro-ph/0003477

Smeingast. 2017, smeingast/PNICER

Spitzer Jr, L. 1954, The Astrophysical Journal, 120, 1

Spitzer Jr, L. 2008, Physical processes in the interstellar medium (John Wiley & Sons)

Stahler, S. W. & Palla, F. 2008, The formation of stars (John Wiley & Sons)

Stern, D., Eisenhardt, P., Gorjian, V., et al. 2005, The Astrophysical Journal, 631, 163

Sugitani, K. 1989, in The Physics and Chemistry of Interstellar Molecular Clouds: mm and Sub-mm Observations in Astrophysics (Springer), 112–113

Sugitani, K., Fukui, Y., & Ogura, K. 1991, the Astrophysical Journal Supplement Series, 77, 59

- Sugitani, K. & Ogura, K. 1994, The Astrophysical Journal Supplement Series, 92, 163
- Sugitani, K., Tamura, M., & Ogura, K. 1995, The Astrophysical Journal Letters, 455, L39
- Tej, A., Ojha, D., Ghosh, S., et al. 2006, Astronomy & Astrophysics, 452, 203
- Tenorio-Tagle, G., Bodenheimer, P., Rozyczka, M., & Franco, J. 1986, Astronomy and Astrophysics, 170, 107
- Vink, J. S., de Koter, A., & Lamers, H. J. 2000, arXiv preprint astro-ph/0008183
- Walawender, J., Bally, J., & Reipurth, B. 2005, The Astronomical Journal, 129, 2308
- Warin, S., Benayoun, J., & Viala, Y. 1996, Astronomy and Astrophysics, 308, 535
- Wasserburg, G., Black, D., & Matthews, M. 1985, University of Arizona Press, Tucson, 703
- Wells, L. A. 1994, IRAF Photometry Documentation
- Whitworth, A. P., Bhattacharjee, A. S., Chapman, S. J., Disney, M. J., & Turner, J. A. 1994, Monthly Notices of the Royal Astronomical Society, 268, 291
- Wilking, B. A. 1989, Publications of the Astronomical Society of the Pacific, 101, 229
- Yadav, R. K., Pandey, A., Sharma, S., et al. 2016, Monthly Notices of the Royal Astronomical Society, 461, 2502
- Zavagno, A., Deharveng, L., Comeron, F., et al. 2006, Astronomy & Astrophysics, 446, 171
- Zeidler, P., Preibisch, T., Ratzka, T., Roccatagliata, V., & Petr-Gotzens, M. 2015, VizieR Online Data Catalog, 358